Drag Measurement in Unsteady Compressible Flow

Marc Efune

A dissertation submitted to the Faculty of Engineering and the Built Environment, University of the Witwatersrand, Johannesburg, in fulfilment of the requirements for the degree of Master of Science in Engineering.

Johannesburg, March 2003

Declaration

I declare that this dissertation is my own, unaided work, except where otherwise acknowledged. It is being submitted for the degree of Master of Science in Engineering at the University of the Witwatersrand, Johannesburg. It has not been submitted before for any degree or examination at any other university.

Signed this _____ day of __________ 20

____

Marc Efune.

To my father and late mother.

Acknowledgements

I would like to express my sincerest appreciation to Professor Skews for his advice, support and most of all patience. I would also like to thank Professor Skews for securing funding for the project.

A special thanks goes to Dr. Murray Bredin for opening up this field of research at the university. Without his work, this thesis would never have been possible. I would also like to thank Dr. Murray Bredin for his help and input whenever it was required.

I am very grateful to the School of Mechanical, Industrial and Aeronautical Engineering for allowing me the opportunity to further my studies.

Thanks to Mr Cooper and the laboratory staff for their support and assistance.

I would like to thank Antun Andreis, Nandkishore Menon, Jithin Mohan and Ivor Clifford and all the other post-graduate students for their constant help and encouragement.

Abstract

Drag over a wide range of shapes is well established for steady flow conditions. Drag in unsteady flow, however, is for the most part not well understood. The research presented herein examines the drag over cones in unsteady compressible flow. This was achieved by constraining cones, with half-vertex angles ranging from 15° to 30°, in a shock tube and passing shock waves over them. The resulting drag was measured directly using a stress wave drag balance (SWDB). Tests were run at shock Mach numbers between 1.12 and 1.31 with corresponding post-shock Reynolds numbers between 2×10^5 and 6×10^5. The drag on the four cone geometries as well as one sphere geometry was modelled numerically. Density contours of the flow fields, obtained from the numerical simulations were used to visualise the shock/model interactions and deduce the causes of any variations in drag. It was thus proved that post-shock fluctuations are due to shock wave reflections off the shock tube walls and the model support. The maximum unsteady drag values measured experimentally ranged from 53.5 N for the 15° cone at a Mach number of 1.14 to 148.6 N for the 30° cone at a Mach number of 1.29. The drag obtained numerically agreed well with experimental results, showing a maximum deviation in peak drag of 9.6%. The drag forces on the conical models peaked as the shock wave reached the base of the cone whereas the drag on the sphere peaked just before the shock reached the equator of the sphere. The negative drag and large post-shock drag fluctuations on a sphere measured by Bredin (2002) were present in the numerical results and thus confirm that these features were not due to balance error. The large post-shock drag fluctuations were also present on the cones. The unsteady drag was shown to increase as both the shock wave Mach number and the cone angle were increased. The ratio of the maximum unsteady drag to the compressible steady state drag varied from

4.4:1 to 9.8:1, while the ratio of the maximum unsteady drag to the incompressible steady state drag varied from 8.3:1 to 22.2:1. The steady state drag values were shown to be of the same order of magnitude as the post shock unsteady drag. Further numerical work is recommended to confirm that drag fluctuations are in fact due to shock reflections and to better establish the relationship between the unsteady drag and the cone angle.

Contents

List of Figures

List of Tables

List of Symbols

a	Speed of sound
c	Speed of sound
C_D	Drag coefficient
$C_{D\text{-}C}$	Compressible steady state drag coefficient
$C_{D\text{-}I}$	Incompressible steady state drag coefficient
d	Maximum diameter
M	Mach number
P	Pressure
R	Universal gas constant
Re	Reynolds number
T	Temperature
t	Time
V	Velocity
v	Velocity
x	Calibration constant
ε	Half-vertex angle
γ	Ratio of specific heats
μ	Viscosity
ρ	Density

1 Introduction

Most aerodynamic flows, when analysed, are treated as steady. This is largely due to the fact that the steady state drag coefficient for most particles is well established. The effect on the drag coefficient of unsteady flow, however, is for the most part not well understood. The assumption of steady flow is incorrect in many situations and thus a better understanding of the effect of unsteady flow is of great significance.

Situations where particles experience unsteady flow include aerosol and pollutant dispersal and fuel injection into internal combustion engines. Many aerodynamic systems such as aircraft and wind energy conversion systems are subjected to unsteady flow due to turbulence and atmospheric variability. Another important field of study into unsteady flow involves objects subjected to blast waves. In order to accurately predict the behaviour of these particles and systems, under such conditions, one needs to determine the unsteady drag they will experience.

Cones have particular importance in this field of research as nose cones are employed so widely on aircraft, rockets and so on. The added advantage of a cone is that the separation point is fixed and thus one would expect the drag to remain fairly constant under steady flow conditions.

During the course of the project attempts were made to obtain reliable unsteady drag coefficients from both experimental data and computational fluid dynamics (CFD) simulations. These attempts were deemed important since steady state drag data is almost exclusively quoted in the form of a non-dimensional drag coefficient. The drag coefficient, C_D, for a body of revolution in steady flow is calculated as follows (Morrison, 1962):

$$C_D = \frac{Drag}{\frac{\rho}{2} V^2 \pi \frac{d^2}{4}} \tag{1.1}$$

where: ρ = free stream density

V = free stream velocity

d = maximum diameter

Under steady flow conditions the free stream density and velocity are unambiguous and thus a reliable drag coefficient can be obtained. In unsteady flow, however, the choice of reference point for measuring the density and velocity is arbitrary thus rendering the drag coefficient untrustworthy. It was therefore decided for this project to work with the actual drag force alone.

2 Objectives

The objectives of the project were to:

- Measure the drag on various cones in unsteady compressible flow.
- Determine the effect of vertex angle and Mach number on the measured drag.
- Compare the drag measured experimentally with steady state values as well as that predicted by CFD simulations.
- Verify the suitability of using a stress wave drag balance for measuring drag in unsteady compressible flow.
- Compare the drag on a cone with the drag on a sphere and thereby confirm whether variations in drag measured on a sphere by Bredin (2002) using the same equipment, are in fact drag variations and not due to balance error. This should be possible since, as stated previously, with the separation point of a cone being fixed, one expects the drag to remain fairly constant under steady flow conditions.

3 Background and Motivation

3.1 Applicable Gas Dynamics

3.1.1 Normal Shock Theory

As stated previously, the purpose of this research was to measure drag in unsteady flow. The unsteady flow generated was in the form of accelerating fluid flow, specifically shock waves. The following section outlines the basic gas dynamics theory that will be used when analysing the physical processes and when setting up numerical simulations. The theory was extracted from John (1969).

The Mach number, M, is the ratio of the generated particle speed (or wave) in a gas to the speed of sound in that gas. For a compressible gas, the speed of sound in the gas will remain constant if the temperature remains constant.

The speed of sound, c, is calculated as follows:

$$c = \sqrt{\gamma R T} \tag{3.1}$$

where:

where:	γ	=	ratio of specific heats (1.4 for air)
	R	=	universal gas constant (0.2871 kJ/kg K)
	T	=	temperature of the gas

In subsonic flow ($M < 1$) the generated speed of the gas particles is less than the speed of sound and the gas ahead of the waves is able to adjust steadily to the oncoming waves. When the flow is supersonic ($M > 1$) the gas must adjust rapidly and a shock wave forms.

Variations in pressure, temperature and density occur across the shock wave. The passage of a shock wave results in an effectively instantaneous increase in pressure, density and temperature since the wave thickness is so small. The properties across a stationary shock wave can be determined using the following equations:

$$M_2^2 = \frac{M_1^2 + 5}{7M_1^2 - 1} \tag{3.2}$$

$$\frac{T_2}{T_1} = \frac{\left(1 + 0.2M_1^2\right)\left(7M_1^2 - 1\right)}{7.2M_1^2} \tag{3.3}$$

$$\frac{P_2}{P_1} = \frac{7}{6}\left(M_1^2 - 1\right) \tag{3.4}$$

$$\frac{V_2}{V_1} = \frac{\rho_1}{\rho_2} = \frac{1 + 0.2M_1^2}{1.2M_1^2} \tag{3.5}$$

where:

where:	M_1	=	incident Mach number
	M_2	=	Mach number downstream of shock
	T_2/T_1	=	static temperature ratio across the shock
	P_2/P_1	=	static pressure ratio across the shock
	V_2/V_1	=	velocity ratio

3.1.2 Compressible Duct Flows

The preceding equations allow one to calculate flow properties across a plane normal shock wave. They are thus adequate for tasks such as initialising the flow in a numerical simulation. A different technique is required to predict the compressible duct flow found in a shock tube however. The technique employed is known as the method of characteristics. A basic introduction of this method has been summarised from Thompson (1972) and Han and Yin (1993).

The method of characteristics utilizes the *x-t* or *wave* diagram for representing unsteady flows. The construction of *x-t* diagrams is based on the principle that any flow perturbation will travel at the speed of sound in the flow. If one fixes the axes of observation relative to the wall of the duct, the perturbation will appear to travel at the speed of sound plus the duct flow speed.

A convenient introduction to the analysis of compressible duct flow is given by the *piston problem*. Figure 3.1 shows a piston moving through a duct. The piston and the gas ahead of it are initially stationary until at time $t = 0$ the piston motion, $U(t)$, is initiated.

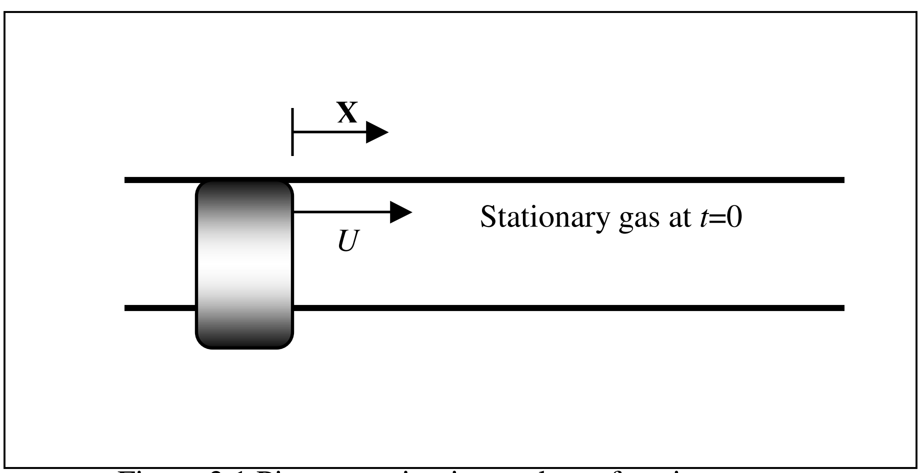

Figure 3.1 Piston moving into a duct of stationary gas

The acceleration of the piston into the duct causes a weak pressure wave to propagate into the duct. As the piston accelerates further, additional pressure waves are transmitted into the duct. Each pressure wave is represented as a characteristic in Figure 3.2. A characteristic represents a line along which all flow properties are constant. The initial pressure waves generated by the piston are compression waves. Each wave accelerates and pressurises the gas slightly thereby raising the temperature. The sound speed behind each wave is thus increased. Subsequent waves, travelling at the higher speed of sound, thus catch up to the preceding waves. This occurrence results in the forming of a shock wave and is the point on a wave diagram where two or more characteristics intersect.

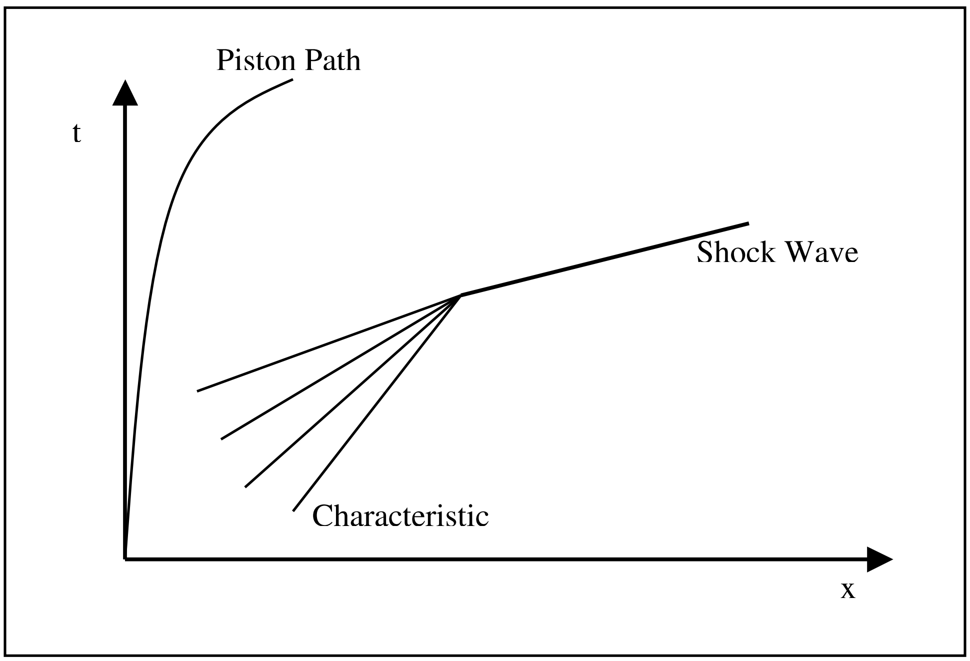

Figure 3.2 Formation of a shock wave where characteristics intersect

3.1.3 Reflection of Shockwaves

There are two possible types of shock wave reflections from a boundary or symmetry plane, namely *Regular Reflection* and *Mach Reflection*. In the upper schematic of Figure 3.3, regular reflection is shown where the initial shock, *i*, and reflected shock, *r*, intersect on the boundary. The strength of the reflected shock, *r*, is that required to return the flow behind *r* to the original free-stream direction.

The lower schematic illustrates Mach reflection. In this case, the intersection of *i* and *r* does not occur on the boundary and a shock called a Mach stem, *m*, occurs between the boundary and the intersection of all three shocks at the triple point, *T*. A slip surface, *s*, emanates downstream behind the triple point.

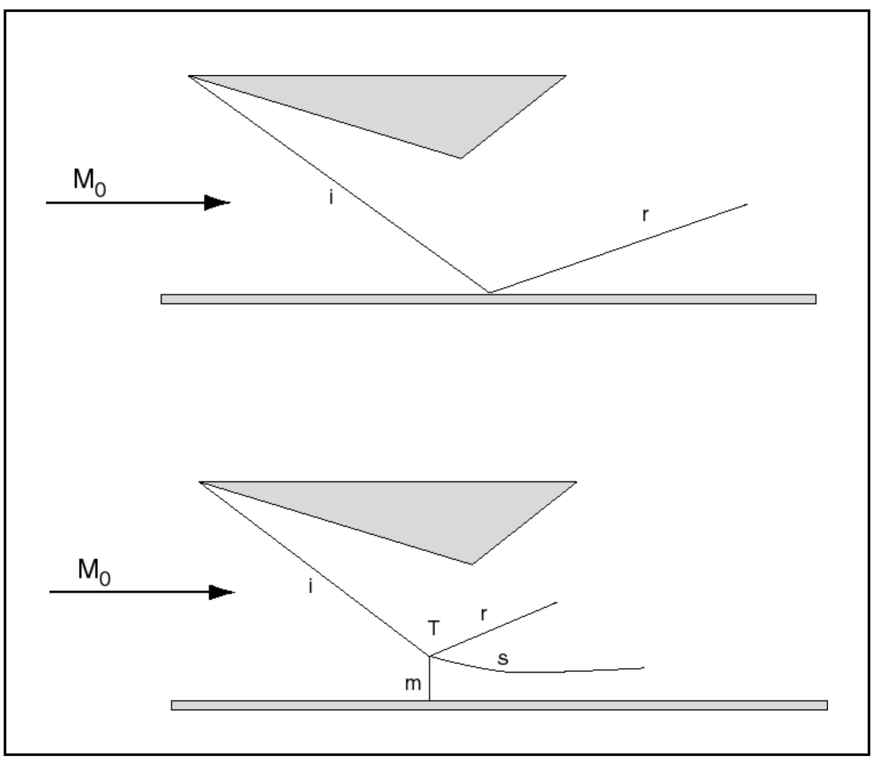

Figure 3.3 Regular and Mach Reflection

3.2 Drag Data in Steady Flow

Drag data, usually in the form of a drag coefficient, is well defined for many model configurations such as spheres, cones and cylinders in steady flow. As mentioned in the introduction, attempts to obtain an unsteady drag coefficient have been deemed untrustworthy. Steady state drag coefficients are well established though and are thus valuable in providing, rather than a quantitative, a qualitative comparison with drag forces measured in unsteady flow. The principal focus of this thesis is the investigation of unsteady drag on cones and thus this section will deal primarily with steady flow drag on cones. However, one of the objectives of this work also deals with gauging the accuracy of drag variations recorded using a sphere, as investigated by Bredin (2002). It was thus deemed necessary to include a short description of steady flow drag on spheres as well.

Drag on conical bodies corresponds closely (disregarding some skin-friction) to the compression waves originating from the apex. It is thus important to categorise the types of flows obtained before delving into the drag produced. Certain steady supersonic flows such as flow over conical bodies depend only on the spherical angle, ε, measured from an axis of symmetry. The resulting pattern of flow is known as *Conical Flow* since all properties are constant on the surface of a cone where ε is constant (Thompson (1972)). This is not always the case, though. At any given free-stream Mach number there is a maximum cone angle (half-vertex angle) for which a conical solution exists. This conical solution occurs when the shock is attached to the apex of the cone. When the maximum cone angle is exceeded, the shock is detached from the cone and the front is round rather than conical. Figure 3.4 from Hoerner (1965) shows this maximum angle for cones as well as wedges, while Figure 3.5 from Thompson (1972) shows an example of an attached shock on the left and a detached shock on the right.

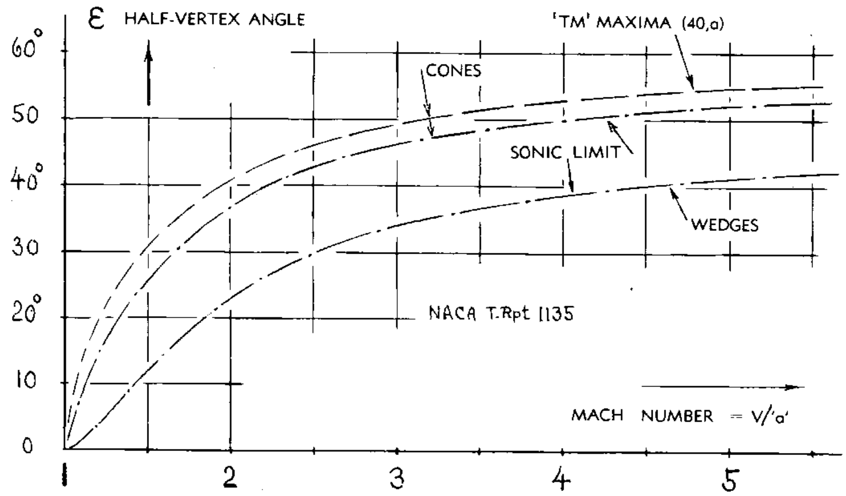

Figure 3.4 Maximum half-vertex angle permitting an attached shock

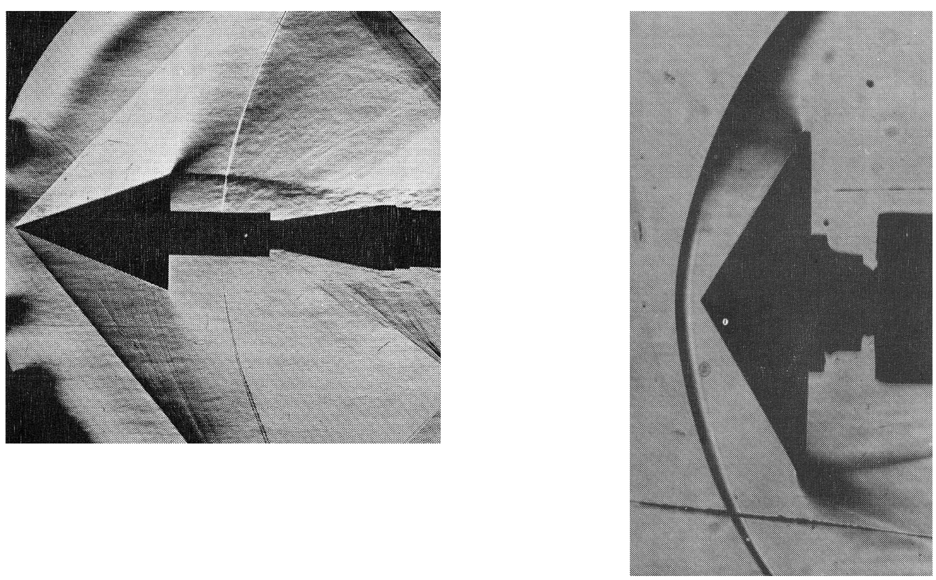

Figure 3.5 Examples of an attached and detached shock

The two key factors affecting the magnitude of the drag coefficient of a cone are the shape, usually inferred by the half-vertex angle, ε, or the fineness ratio (length divided by maximum diameter) and the speed or nature of the flow inferred by the Mach number or Reynolds number. The experimental work to be undertaken will involve cones with half-vertex angles ranging from 15° to 30° corresponding to fineness ratios between 1.85 and

0.86. In terms of the range of flows, shock waves with Mach numbers between 1.1 and 1.3 are envisaged. Post shock Reynolds numbers between 2×10^5 and 7×10^5 corresponding to post shock Mach numbers between approximately 0.15 and 0.41 are expected. Numerical simulations will reproduce flows with shock Mach numbers up to 1.5. The appropriate range of these key parameters should be kept in mind when viewing the following figures.

Figure 3.6, from Hoerner (1965), shows the drag coefficients of wedges, cones and similar shapes as a function of their half-vertex angle for Reynolds numbers between 10^4 and 10^6 in uncompressed fluid flow. Figures 3.7 and 3.8, from Morrison (1962), show the total drag coefficient on various bodies of revolution as a function of fineness ratio and Mach number respectively.

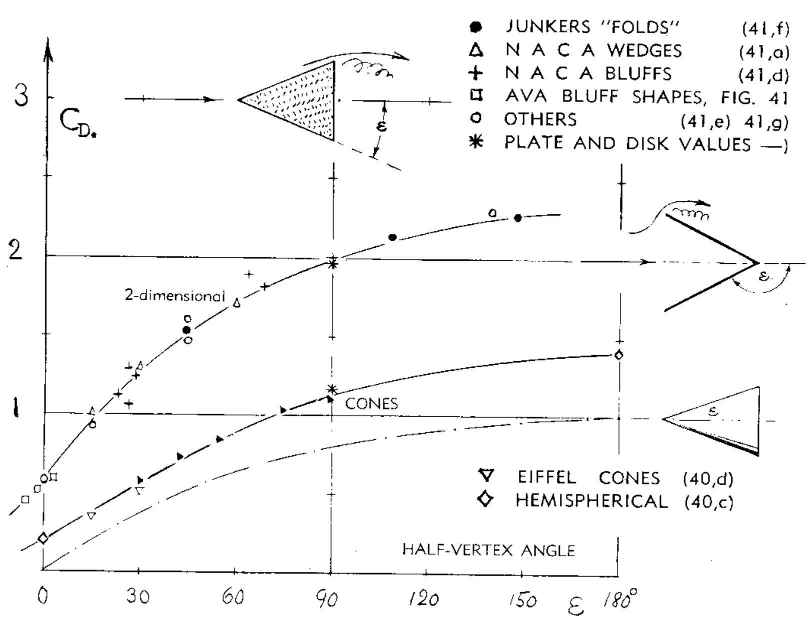

Figure 3.6 Drag coefficients of cones and other shapes as a function of half-vertex angle

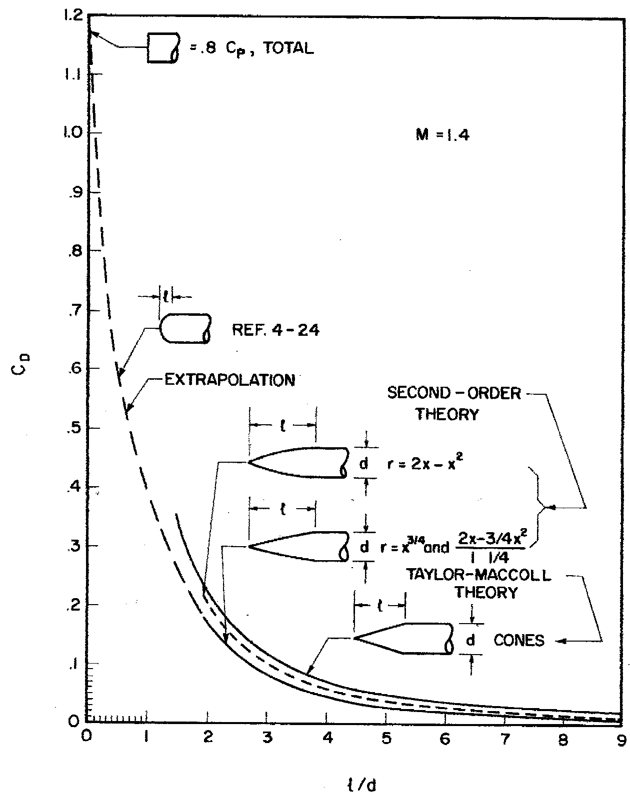

Figure 3.7 Drag coefficients on bodies of revolution at M = 1.4

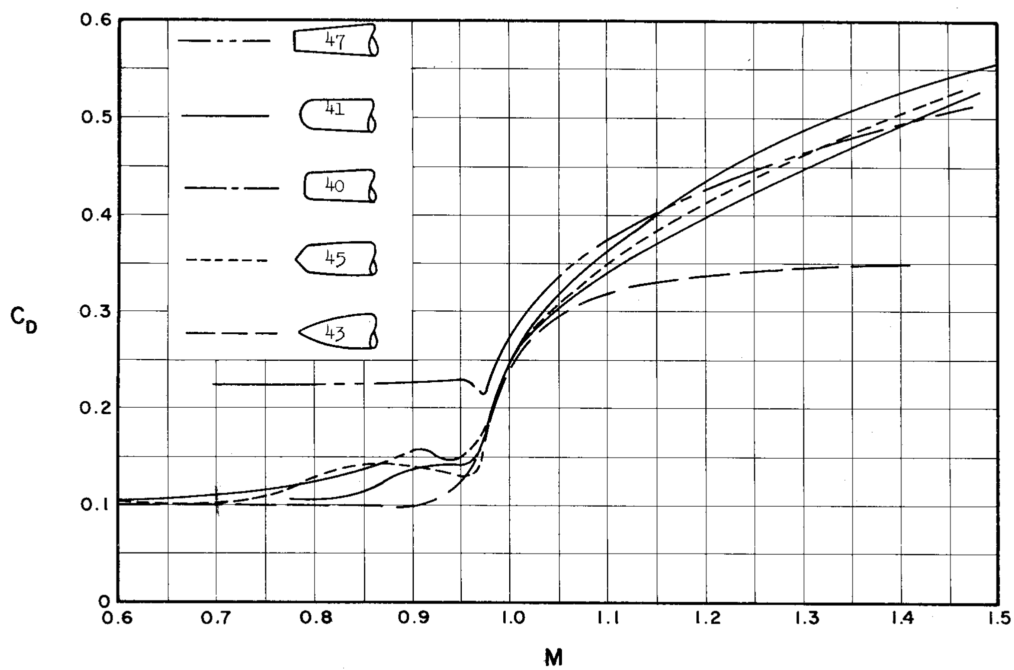

Figure 3.8 Drag coefficients for five configurations with fineness ratios of about 2

Conical flow, described previously, is theoretically treated as a half-infinite pattern of flow thereby accounting for pressure and drag on cones of finite length in truly supersonic axial flow. At subsonic and transonic speeds, however, the pressure on the surface of a cone starts from an infinitely small stagnation point diminishing to values below ambient pressure at the cone's rim. Theoretical methods describing and correlating these transonic pressure changes and the corresponding changes in drag coefficient employ certain linearised terms and are thus only realistic for very small cone angles (Hoerner (1965).

As stated previously, the post shock Mach numbers are expected to peak at approximately 0.41. Interestingly, no compressible steady state drag coefficient data could be found in the literature for cones at these speeds. An example of such data is illustrated below in Figure 3.9, from Hoerner (1965), which shows theoretical (40,a) and experimental (41,d; 41,a) drag coefficients of various conical heads at transonic and supersonic Mach numbers, with the minimum Mach number being 0.6. It was thus decided to use CFD simulations to obtain the steady state compressible drag coefficients as will be discussed later.

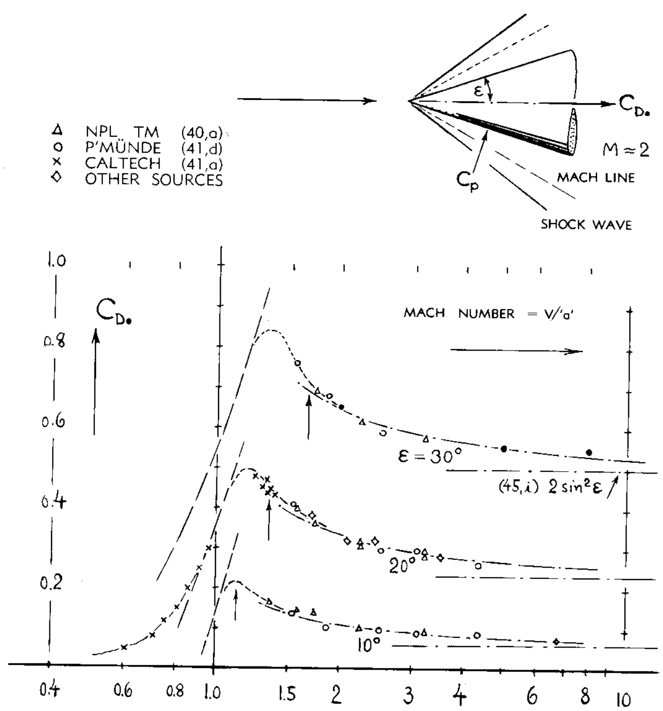

Figure 3.9 Drag coefficients of various conical heads as a function of Mach number

The afore-mentioned relationships between the steady state drag on a cone and the flow speed and cone angle consistently reveal an increase in drag as both parameters (in the appropriate range) are increased.

The coefficient of a drag on a sphere in steady flow is well defined as a function of Reynolds number up to Reynolds numbers of 10^7. Figure 3.9, from Clift et al. (1978) illustrates this relationship. As stated previously, the Reynolds numbers relevant to the current project range from 2×10^5 to 7×10^5. No theoretical calculations have been able to predict drag in this range, thus the drag values have been obtained empirically.

Figure 3.10 shows C_D to be fairly constant at 0.5 for $2 \times 10^5 < Re < 3 \times 10^5$. As Re reaches 3×10^5, marked changes in the flow pattern occur. This phase is known as *critical transition*. During this phase, the flow separates from the sphere resulting in a wide turbulent wake behind the sphere. The separation point then begins to move towards the rear of the sphere, while fluctuations in the position of the separation point and in pressure and skin friction also start to increase. Further increase of Reynolds number results in the wake becoming very narrow and thus at $Re = 4 \times 10^5$ the drag coefficient drops to 0.07. The definition of a Reynolds number at which critical transition is said to occur is arbitrary since it depends on the surface roughness of the sphere and the free-stream turbulence of the flow. It is taken as the Reynolds number at which $C_D = 0.3$, corresponding to $Re = 3.65 \times 10^5$ for a free-stream flow with no turbulence. At Reynolds numbers greater than 4×10^5 the drag coefficient increases slightly tending towards a constant value of approximately 0.19 (Clift et al. (1978)).

Clift et al. (1978) also presents C_D as a function of Mach number with Reynolds number as a parameter. Figure 3.11 shows an increase in drag as the Mach number increases from 1 to approximately 1.5 for $Re = 10^5$.

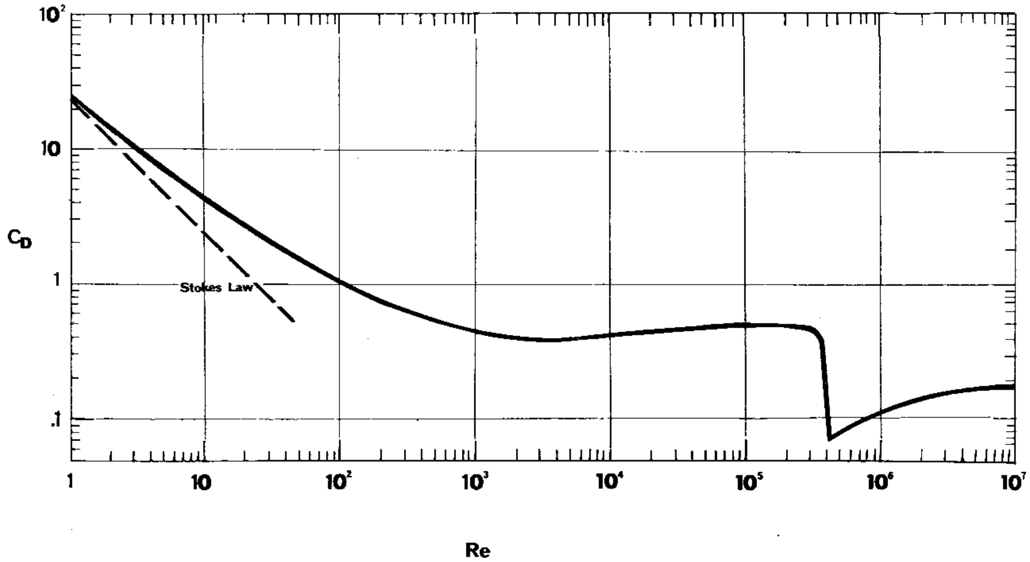

Figure 3.10 Drag coefficient of a sphere as a function of Reynolds number

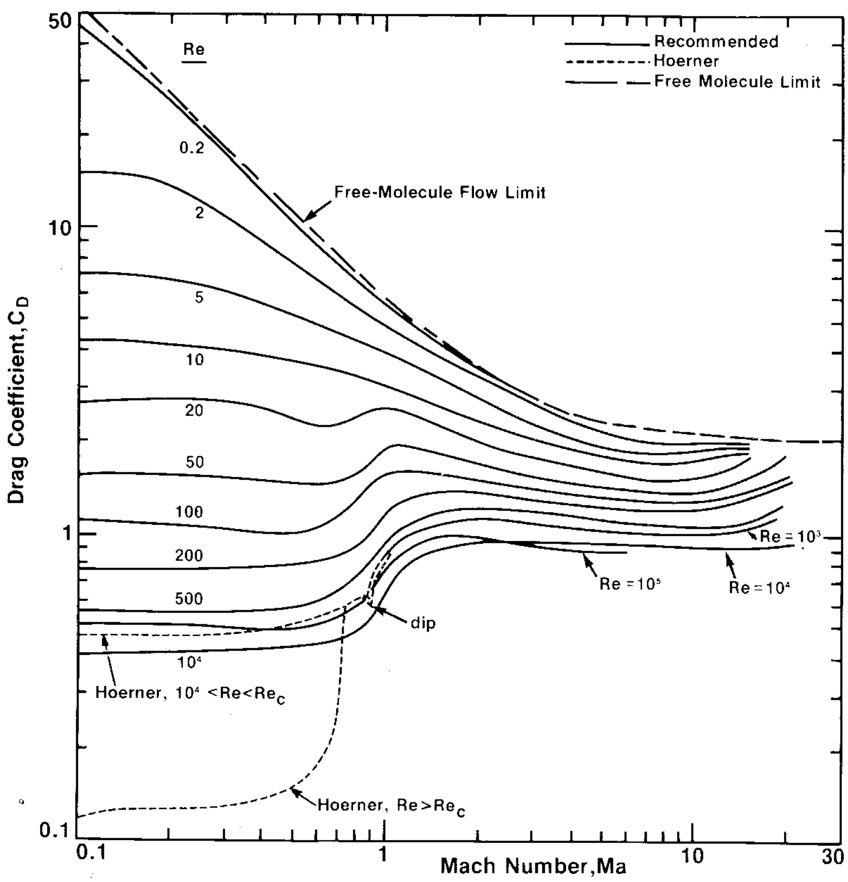

Figure 3.11 Drag coefficient of a sphere as a function of Mach number and Reynolds number

3.3 Drag Data in Unsteady Flow

The drag on bodies such as cones and spheres in steady flow as outlined above has been well established. A full understanding of drag in unsteady flow however, is still in its infancy. The first work on unsteady drag was performed by Stokes (1851) who derived a theoretical prediction for the force on a sphere oscillating in a fluid using the assumption of creeping flow. His derivation showed the unsteady drag to be equal to the steady state drag plus an 'added mass force'. The added mass force is the additional force required to accelerate the fluid around the body.

Boussinesq (1885) and Basset (1888) carried out further theoretical work producing the following relationship: Unsteady drag = Steady state drag + Added mass force + History integral force where the new term accounts for the unsteady viscous diffusion of vorticity around the sphere. The history integral force is also known as the Basset history force.

Most of the subsequent research involved experimental attempts to correlate the unsteady drag with Reynolds number. The resulting empirical equations are specific to the range of Reynolds numbers from which they were derived. There have been two chief methods of investigating drag in unsteady flow. The first method involves measuring the drag force on a model directly from the model support. The second method uses optical techniques to infer, from the trajectory, the drag on an unrestrained model accelerating relative to the flow.

Tyler and Salt (1977) measured the trajectories of unrestrained spheres accelerated by shock waves for Reynolds numbers between 1×10^4 and 5×10^4. A sphere was released from the top wall of the shock tube (using an electromagnet) such that the sphere was in the centre of the shock tube as the shock arrived. Periodic discontinuities in the trajectories corresponding to discontinuities in drag were observed. The initial C_D is 10 to 12% higher than the steady state value rising to between 20 and 30% higher as the particle decelerates. The C_D then drops sharply and this process recurs with a period of ±2 ms. It is presumed that the drag response is due to the formation and shedding of vortices from the sphere. As a vortex forms behind the sphere the pressure difference across the sphere would increase causing an increase in drag. If the vortex were then shed the pressure difference would decrease resulting in a sharp drop in drag.

Igra and Takayama (1993) tracked the trajectory of a sphere in a shock tube for the range $6 \times 10^3 < Re < 1 \times 10^5$. The sphere was initially placed on the shock tube floor leading one to believe that the flow field around the sphere must have been affected. The measured drag coefficients were 50% higher than steady state values for $Re > 1 \times 10^4$ and 100% higher for $Re < 1 \times 10^4$.

Britan et al. (1995) placed spheres of various sizes on a thin wire support in a shock tube. They found the ratio of cross-sectional areas of the shock tube and sphere had a minor effect on the sphere's acceleration. Shadowgraph photography was used to track the sphere position and to visualise the shock interaction with the sphere. The results show the reflected wave has a bow shape. The region between the reflected wave and the sphere is at a much higher pressure than the downstream portion of the sphere (at atmospheric pressure). This difference in pressure results in an increase in drag in the direction of the flow. Since the reflected wave propagates out spherically the reflected pressure on the sphere decays with time. One would thus expect the maximum drag to occur just before the incident shock reaches the equator.

Shadowgraphs taken at a later time show the original reflected shock wave having been reflected off the shock tube walls. This reflected wave travels back towards the centre of the shock tube spherically. The portion of the wave travelling upstream (since it is travelling against the direction of the flow) reaches the front of the sphere after the portion of the wave travelling downstream reaches the rear of the sphere. Thus, a greater portion of the rear half of the sphere will be covered by this reflected wave. The high pressure region behind the wave may thus cause the net drag on the sphere to be acting upstream. This would be indicated by negative drag readings. Britan et al. (1995) however, were not able to measure the sphere displacement and hence the drag during the shock wave reflection and diffraction.

Rodriguez et al. (1995) investigated the unrestrained motion of spheres in a vertical shock tube. The spheres were initially allowed to fall freely until subjected to an upward-moving shock wave. The recorded drag coefficient was 25% higher than steady state values for $5 \times 10^3 < Re < 1.2 \times 10^5$.

Recent improvements in techniques for measuring unsteady drag in flow accelerated by shock waves have led to some noteworthy results, mostly regarding unsteady drag on a sphere due to shock wave loading. Bredin (2002) using the apparatus employed for the current work measured the drag on a sphere constrained in a shock tube. The drag was measured directly using a stress wave drag balance and deconvolution data processing, the use of which will be discussed in the following section.

Tests were run with shock wave input and steady post shock flow in which three stages were identified. During the first stage the shock reflection and diffraction were predominant. The drag rose to a maximum at approximately the same time that the shock wave took to reach the equator of the sphere. The drag then decreased faster than the time needed for the shock to reach the rear of the sphere. Negative drag was observed at this point. The second stage was characterised by the reflection of the shock waves off the walls of the shock tube. During this stage the drag exhibited very high frequency oscillations. The final stage corresponding to steady flow showed the drag still to be unsteady. Figure 3.12 illustrates the drag measured on the sphere, highlighting the effect of shock strength on the drag.

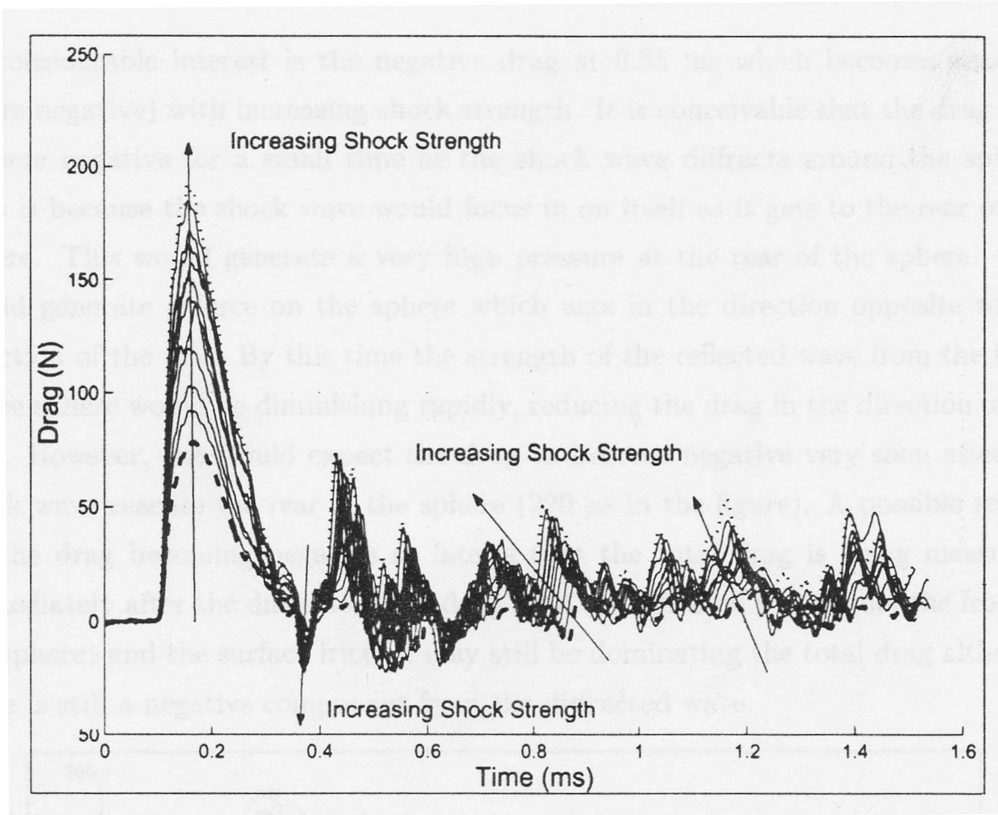

Figure 3.12 Drag measured on a sphere (Bredin (2002))

Tanno et al. (2003) performed an experimental and numerical study of the unsteady drag force acting on a sphere suspended in a vertical shock tube and loaded with a planar shock wave of $M_S = 1.22$ in air. The drag force was measured by an accelerometer installed inside the sphere. Using deconvolution data processing, a drag history comparable to numerical simulations was produced. High speed video recordings and double exposure holographic interferometric observations were also conducted to interpret the interaction of the shock wave over the sphere. Transition of the reflected shock wave from regular to Mach reflection was shown to occur. It was found that the maximum drag force appeared before the shock arrived at the equator of the sphere and before the transition from regular to Mach reflection. Negative drag was observed when the Mach stem of the transmitted shock wave reflected and focused at the rear stagnation point of the sphere.

Sun et al. (2004) investigated the dynamic drag coefficient of a sphere by shock wave loading numerically and experimentally. Their results correspond well to those described above. They were also able to show numerically the transition from regular to Mach reflection, as illustrated in Figure 3.13. By comparing the times at which transition and the maximum drag occur, it was concluded that the transition of the shock reflection pattern has no significant influence on the overall drag loading, but is a transient phenomenon in shock/sphere interaction.

Of the previous work reviewed, only one example was found regarding the measurement of unsteady drag on shock-loaded bodies other than spheres. Tamai et al. (2004) suspended models with various configurations in a vertical shock tube and subjected the models to planar shock waves of $M_S = 1.22$. Accelerometers installed within the models were used to measure acceleration and thus the drag. Model shapes were cones with smooth and coarse surface finish, a double cone, a sphere, a 2:3 ellipsoid and a cylinder. Drag forces were found to reach a maximum when the incident shock wave reaches just before the equator and then decrease to a minimum value. Depending on body shape, the minimum value is negative and maintained for a few hundred microseconds.

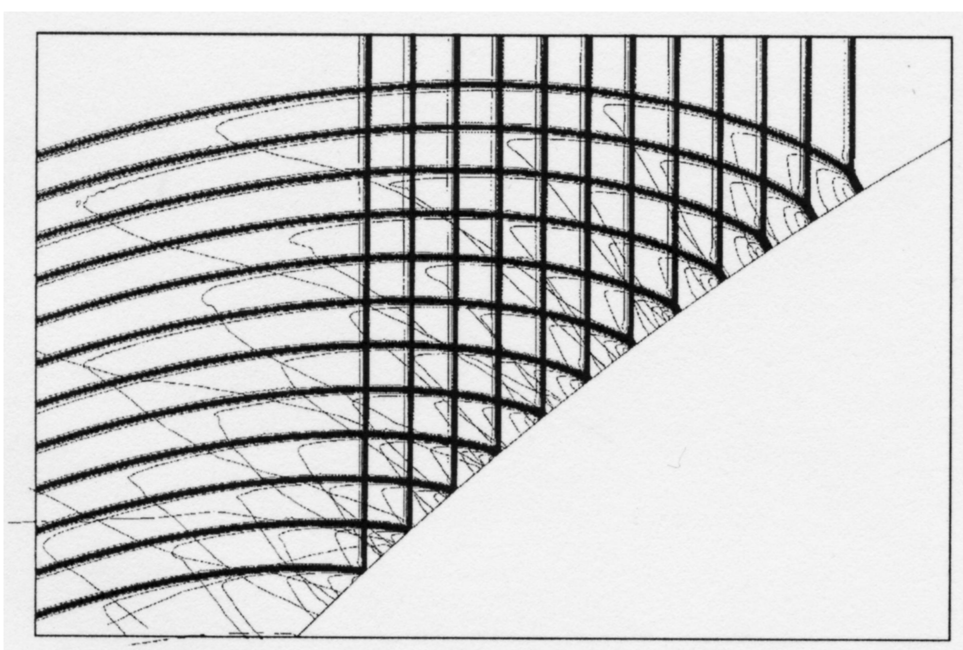

Figure 3.13 Transition from regular to Mach reflection over a sphere

3.4 Stress Wave Drag Balance

The use of force balances to measure aerodynamic forces in steady flow, such as flows produced in wind tunnels, is well established. In transient flows such as those generated in shock tubes however, the use of a conventional force balance presents problems. Conventional force balances require the test model to be in a state of force equilibrium with its support mechanism. Damping mechanisms and/or filters are used to reduce the effects of vibrations caused by the initiation of the flow. The time taken for a shock wave to pass over a model is usually much shorter than the average time taken for vibrations to be damped however. These types of balances typically achieve response times greater than 200 ms, or at best 10 ms by using an accelerometer to compensate for acceleration of the model (Sanderson and Simmons (1991)). In order to reduce the response time of force balances for use in unsteady flow, Sanderson and Simmons developed the Stress Wave Drag Balance (SWDB) technique.

The suitability of a SWDB to measure drag under shock loading conditions has been the subject of much research in recent times. An example of such research is Bredin (2002) using the same apparatus as the current work. This balance was shown to have a response time of 20 μs, enough to follow the drag force as a shock wave reflects off and then diffracts around a sphere. The balance testing time was 1.5 ms and the error was shown to be less than 15%.

Smith and Mee (1996) used a SWDB for the measurement of aerodynamic drag in a hypervelocity expansion tube in which the test flow period was approximately 50 μs. The validity of the technique was demonstrated by comparing the forces measured on a range of sharp cones and two re-entry type heat shield geometries with those expected theoretically. Agreement to within 10% for the cones and 11% for the heat shields was achieved.

A SWDB is a slender rod at the end of which is attached an aerodynamic model. Any drag force applied to the model causes stress waves to propagate within the model. These stress waves are transmitted and reflected within the model and the rod. The history of the stress wave activity is measured by strain gauges at one or more locations on the model or the SWDB.

The aerodynamic model and its support structure behave as a linear dynamic system for forces which lead to linear strains. Such systems can be represented by the convolution integral:

$$y(t) = \int_0^t g(t-\tau)u(\tau)d\tau \tag{3.6}$$

For a SWDB, *u(t)* is the applied load, *y(t)* is the measured strain and *g(t)* is the impulse response function. If the system characteristics (in the form of the impulse response function) are known, then the history of the applied load can be determined from the history of the measured strain (Mee (2003)). This process is called deconvolution.

One method for experimentally determining the impulse response of the system is to measure the output signal generated by a step change in the input. Mee (2003) outlined the following process for determining the impulse response from a step input. The impulse response can be determined by differentiating the step response with respect to time and scaling the result appropriately. This can be shown by taking the Laplace transform of Equation 3.6 to obtain:

$$Y(s) = G(s)U(s) \tag{3.7}$$

where *Y(s)*, *G(s)* and *U(s)* are the Laplace transforms of *y(t)*, *g(t)* and *u(t)* respectively. If a step input of magnitude *a* is applied, the Laplace transform of this input is *a/s* and Equation 3.7 becomes:

$$Y(s) = \frac{aG(s)}{s} \tag{3.8}$$

Inverting Equation 3.8 gives:

$$y(t) = a\int_0^t g(\tau)d\tau \tag{3.9}$$

or:

$$g(t) = \frac{1}{a}\frac{dy(t)}{d(t)} \tag{3.10}$$

Therefore, the impulse response can be determined from the response of the system to a step of magnitude *a*. Mee (2003) verifies a number of experimental methods of obtaining a step response and thus the calibration of an SWDB. The method employed for the current work involves attaching a fine wire to the tip of the model, applying a load to it, and then cutting the wire. Further details of this process are provided in Section 4.

Once the impulse response, ($g(t)$), has been determined, the applied load, ($u(t)$) can be found from Equation 3.6 using the following method from Bredin (2002). The measured strain, ($y(t)$), is recorded in a discrete manner, so Equation 3.6 is discretised as follows, where $i = 1,2,3,\ldots$ The sampling interval is Δt and $t = i\Delta t$:

$$y_i = \sum_{j=0}^{i} g_{i-j}.u_j \tag{3.11}$$

Since the initial force is zero, Equation 3.11 can be expanded as follows:

$$y_1 = g_1.u_1 \tag{3.12}$$

$$y_2 = g_1.u_2 + g_2.u_1 \tag{3.13}$$

$$y_3 = g_1.u_3 + g_2.u_2 + g_3.u_1 \tag{3.14}$$

By rearranging and solving the above equations sequentially, *u* can be found for each step.

4 Experimental Apparatus and Procedure

4.1 The Shock Tube

The experimental apparatus employed for the purpose of this work was designed and built by M. S. Bredin for the degree of Doctor of Philosophy. The shock tube was located in the Mechanical Engineering Laboratories at the University of the Witwatersrand. A general outline of the apparatus is given below; if greater detail is required see Bredin (2002).

The shock tube consists of four basic components: the driver section, the variable opening time valve, the driven section and the test section. A schematic of the shock tube can be seen in Figure 4.1.

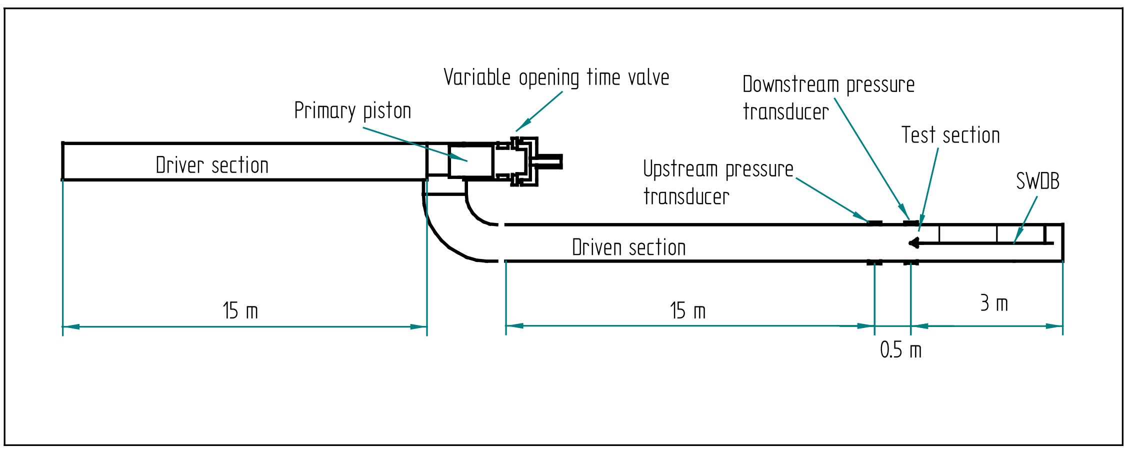

Figure 4.1 Schematic of the shock tube

4.1.1 The Driver Section

The driver section was pressurised using a Mannesmann-Demag SE75EKS compressor. The compressor can provide a maximum pressure of 700 kPa. The desired pressure was achieved by opening a hand-operated ball valve. A maximum driver pressure of 450 kPa was achieved. The driver section is 15 m long and has an internal diameter of 140 mm.

The driver section is separated from the driven section by the primary piston. When running a test, the primary piston is held in position by pressurising a cavity ahead of the piston (cavity 1) to approximately 100 kPa more than the driver pressure. An o-ring, with a major diameter of 190 mm and a thickness of 3 mm, was used to seal the primary piston. This o-ring needed to be replaced on occasion since it tended to disengage from its groove and get destroyed by the moving piston. It was found that gluing the o-ring into place extended the life of the o-ring.

In order to run a test, cavity 1 ahead of the primary piston is vented as described below. The piston then moves forward rapidly allowing the compressed air of the driver section to flow into the driven section and then the test section. A range of Mach numbers were attainable by using the variable opening time valve, which will be outlined in the following section.

4.1.2 The Variable Opening Time Valve

The variable opening time valve makes use of a secondary piston located forward of cavity 1. A further cavity ahead of the secondary piston, cavity 2, is pressurised during a test such that cavity 1 is sealed. After the driver section and cavity 1 have been pressurised, cavity 2 is vented causing the secondary piston to move back into cavity 2. Cavity 1 then vents through holes cut into the secondary piston. Figure 4.2, from Bredin (2002), shows a schematic of the valve as it starts to open.

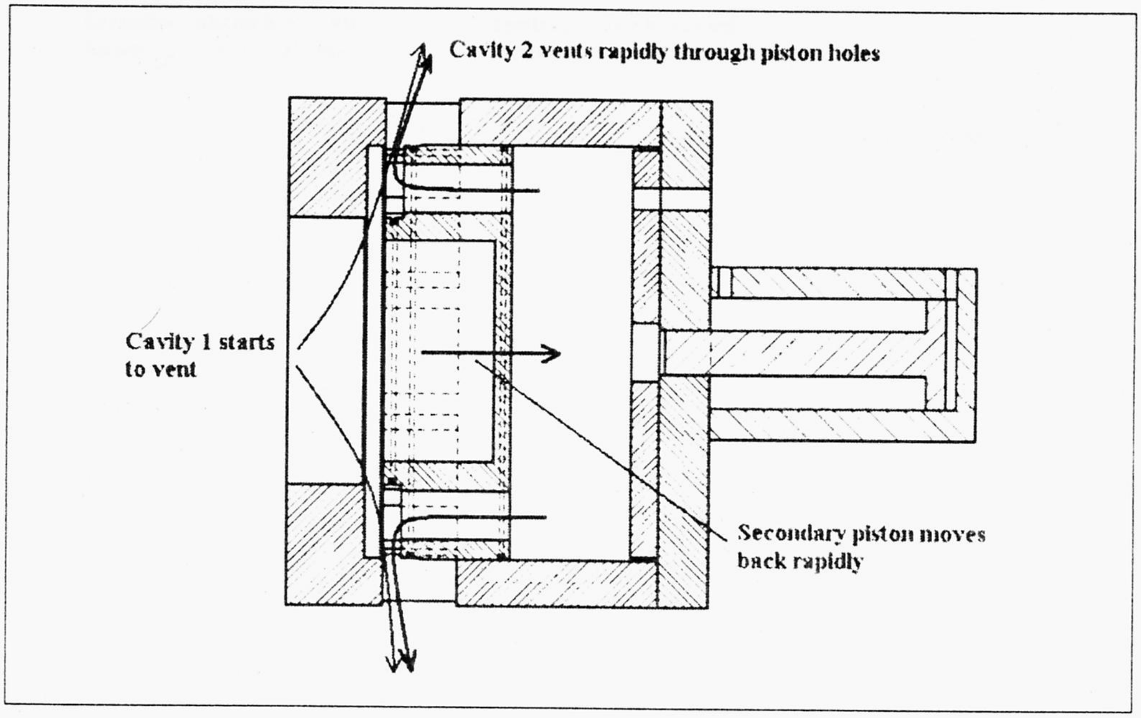

Figure 4.2 Opening of the variable opening time valve

The venting of cavity 1 finally causes the primary piston to move forward thus allowing the compressed air of the driver section to flow into the driven section.

The variation in opening time is achieved by adjusting a steel ring that surrounds the holes cut into the secondary piston. As a greater area of the holes is exposed, cavity 1 vents more rapidly and consequently the primary piston moves forward more rapidly. This means the air enters the driven section quicker and greater Mach numbers are attained at the test section.

Shock waves with Mach numbers varying from 1.12 to 1.31 were achieved by adjusting the driver pressure and the steel ring.

It is important to note that a tertiary piston is used before each test to push the secondary piston back into its starting position thus closing the valve.

4.2 Stress Wave Drag Balance

The stress wave drag balance consists of a 3 m length of 8 mm diameter brass rod instrumented with semi-conductor strain gauges. An aerodynamic shield surrounds the balance to eliminate skin friction between the balance and the airflow in the shock tube. The shield comprises a brass pipe with a large enough diameter to house the balance and the wires from the strain gauges. Foam strips glued onto the balance prevent it from touching the inner wall of the shield. The strain gauges are covered with insulation tape for the same reason. A bush made from PTFE is located at the front of the shield to prevent air from passing between the shield and the balance.

The semi-conductor strain gauge is a Kyowa KSP-1-350-E4 with a gauge factor of 150 and a gauge length of 1 mm. In order to improve the signal to noise ratio it is necessary increase the bridge voltage by connecting the strain gauges to a Wheatstone Bridge. However, increasing the bridge voltage increases the current proportionally. This necessitated the increasing of the nominal resistance of the gauges since they can only withstand limited current. 350 Ω gauges have thus been used rather than the conventional 120 Ω gauges.

4.3 Calibration Models

Four calibration models were designed with cone vertex angles ranging from 60° to 30°. The cones were labelled from 1 to 4, Cone 1 having the largest vertex angle and Cone 4 the smallest. All the cones had a base diameter of 50 mm. The cones were manufactured from aluminium. The calibration models were designed to correspond as closely as possible with each test model. Four separate calibration models were required since the transmission and reflection of stress waves within the models would be different for each model due to the different dimensions.

The choice of materials was critical to the performance of the calibration models. The calibration needed to yield a step response time as short as possible, while damping out any vibrations caused by the calibration procedure. PVC and aluminium models were manufactured and the calibration procedure, outlined in Section 4.5, was performed for each model. The PVC models, due to the naturally higher internal damping, damped out vibrations well, however the response time was too long. Aluminium was thus chosen since a satisfactory response time of approximately 0.2 ms was achieved.

The vibrations were not adequately damped with the aluminium models though, so it was decided to introduce extra materials into the calibration models to provide the necessary damping. To this end, silicone sealant was injected into the calibration models and PVC 'damper screws' were manufactured and screwed into the base of the models to rest against the silicone sealant once it had hardened. This configuration provided the required damping together with a fast response time. The dimensions of the four calibration cones as well as the damper screw are shown below:

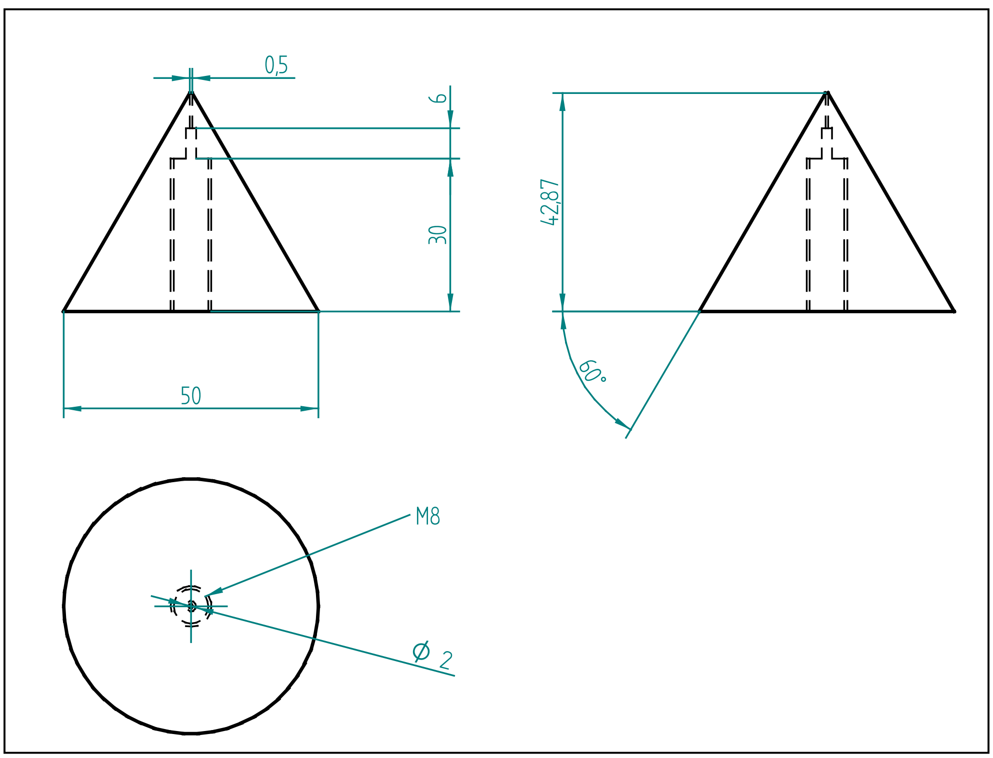

Figure 4.3 Calibration Cone 1

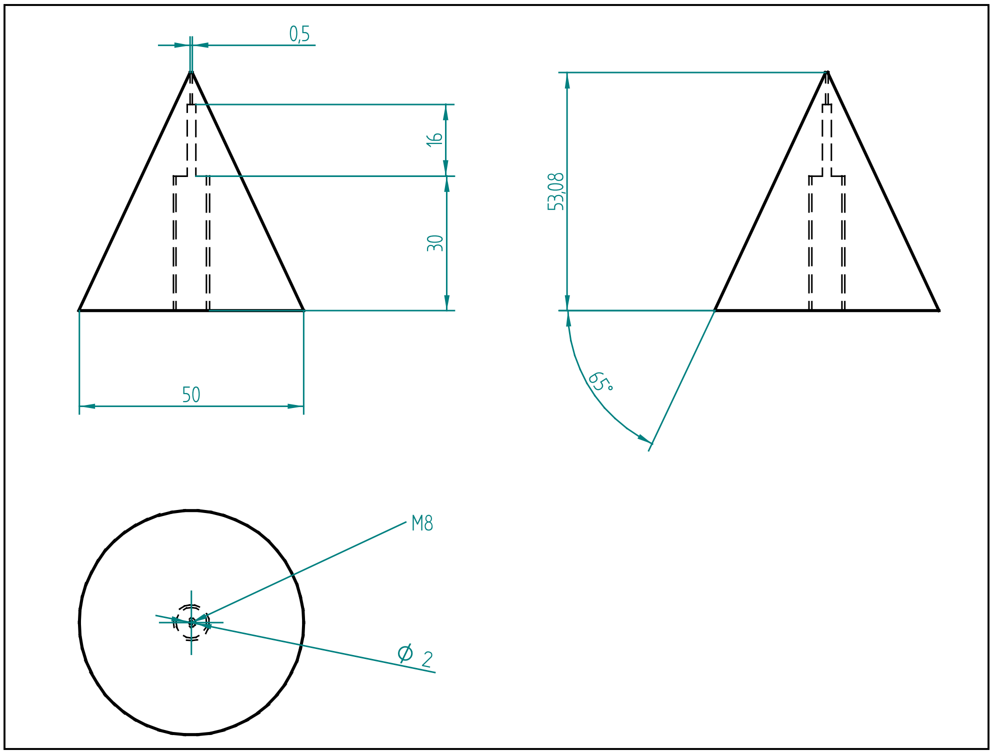

Figure 4.4 Calibration Cone 2

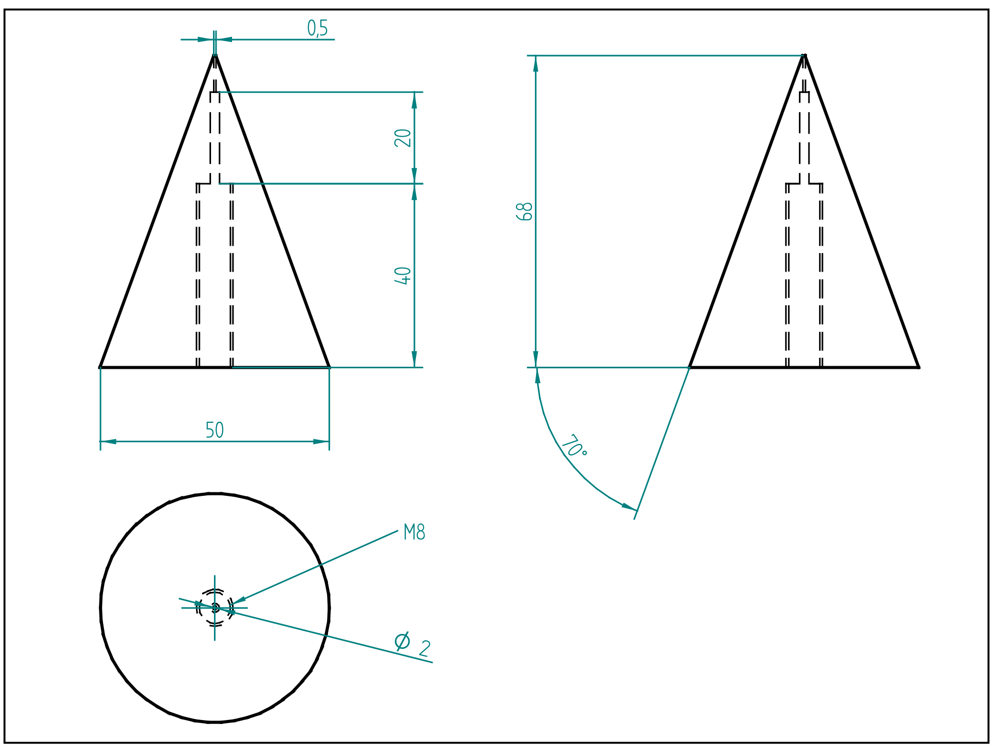

Figure 4.5 Calibration Cone 3

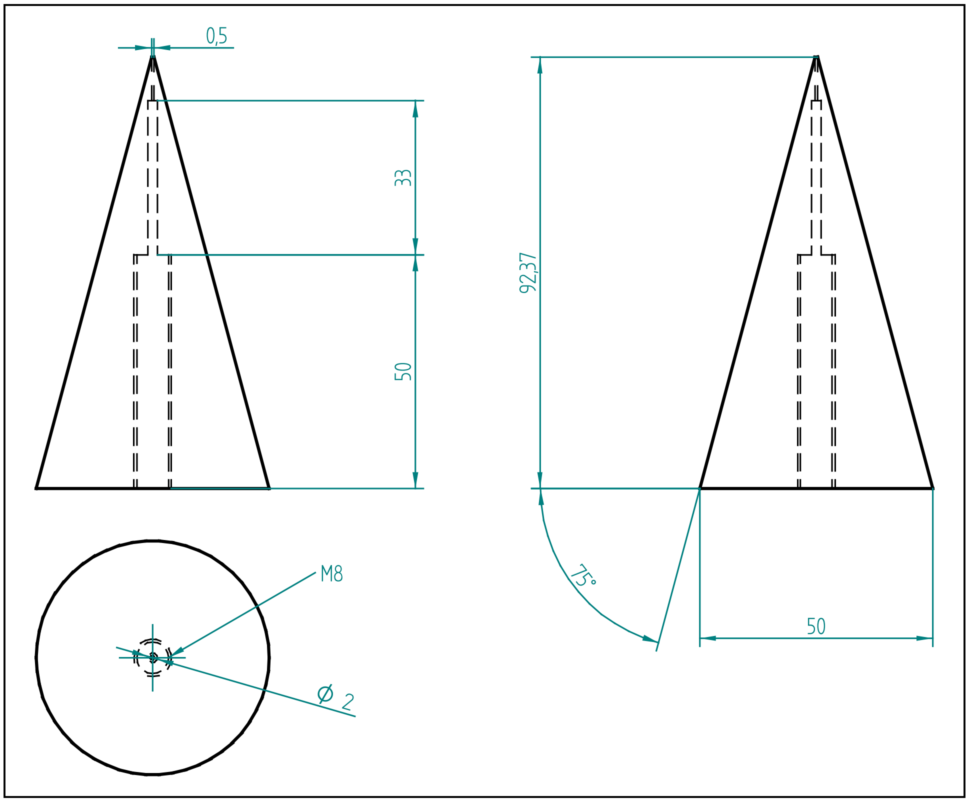

Figure 4.6 Calibration Cone 4

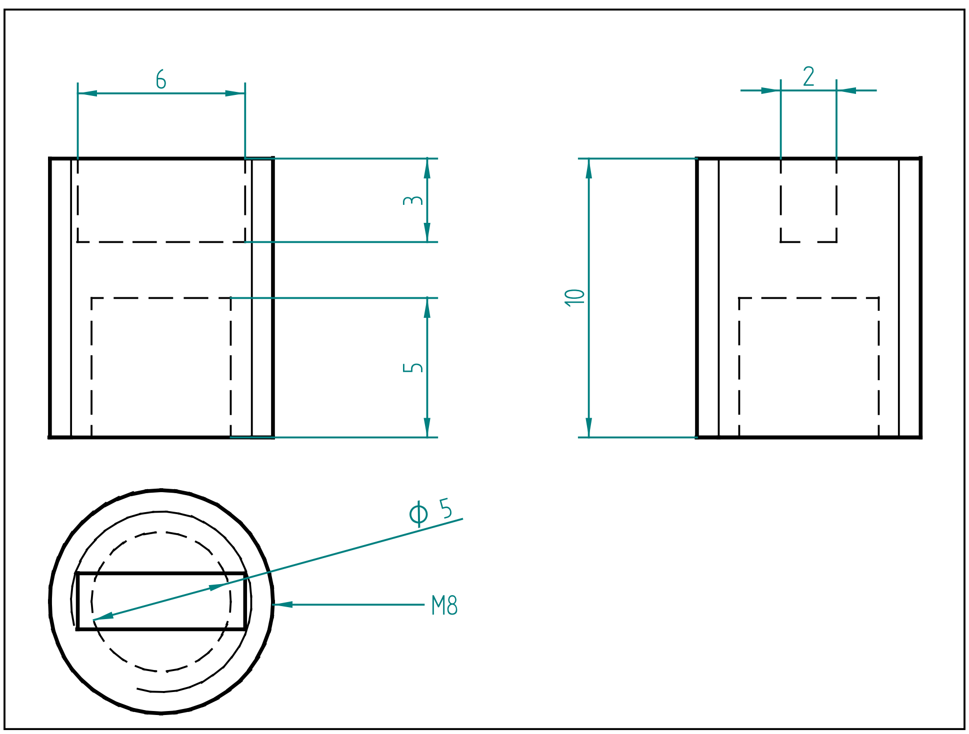

Figure 4.7 Damper Screw

4.4 Test Models

Four test models were designed with cone vertex angles ranging from 60° to 30°. As with the calibration models, Cone 1 has the largest vertex angle and Cone 4 the smallest. Since any change in the configuration of the models changes the response to an applied force, the test models were designed to resemble the calibration models as closely as possible. The 0.5 mm hole drilled into the apex of the calibration cones was omitted from the test models since it was thought that they might affect they flow over the cones. The dimensions of the four test cones are shown below:

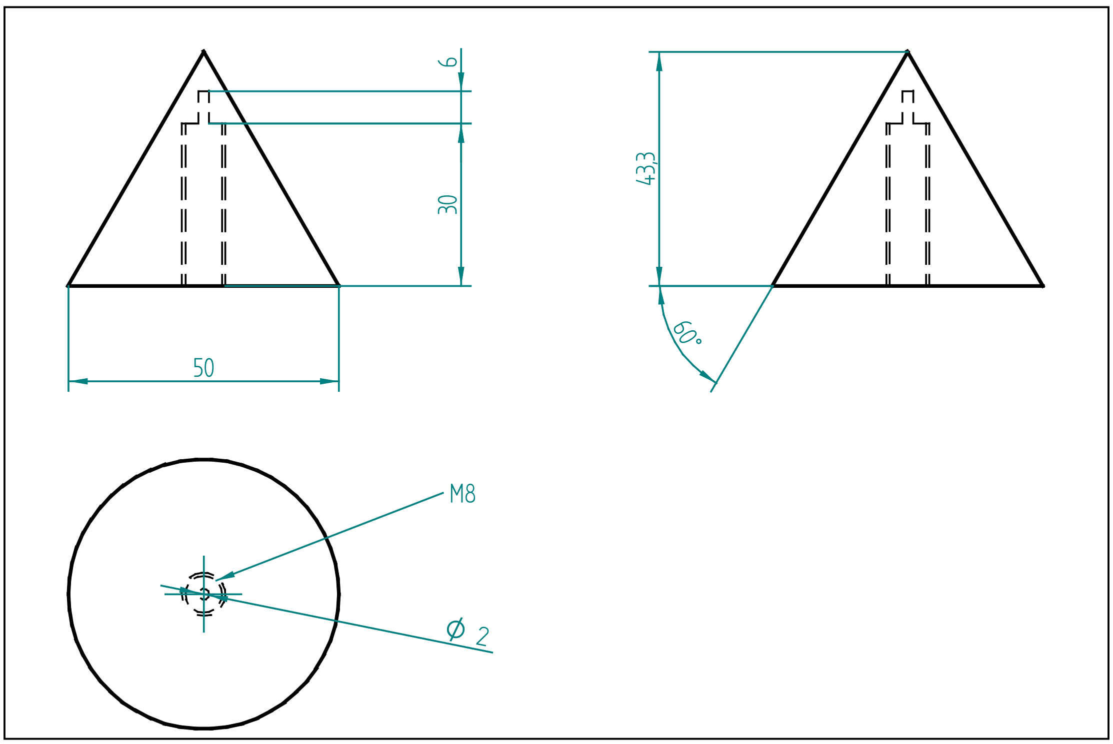

Figure 4.8 Cone 1

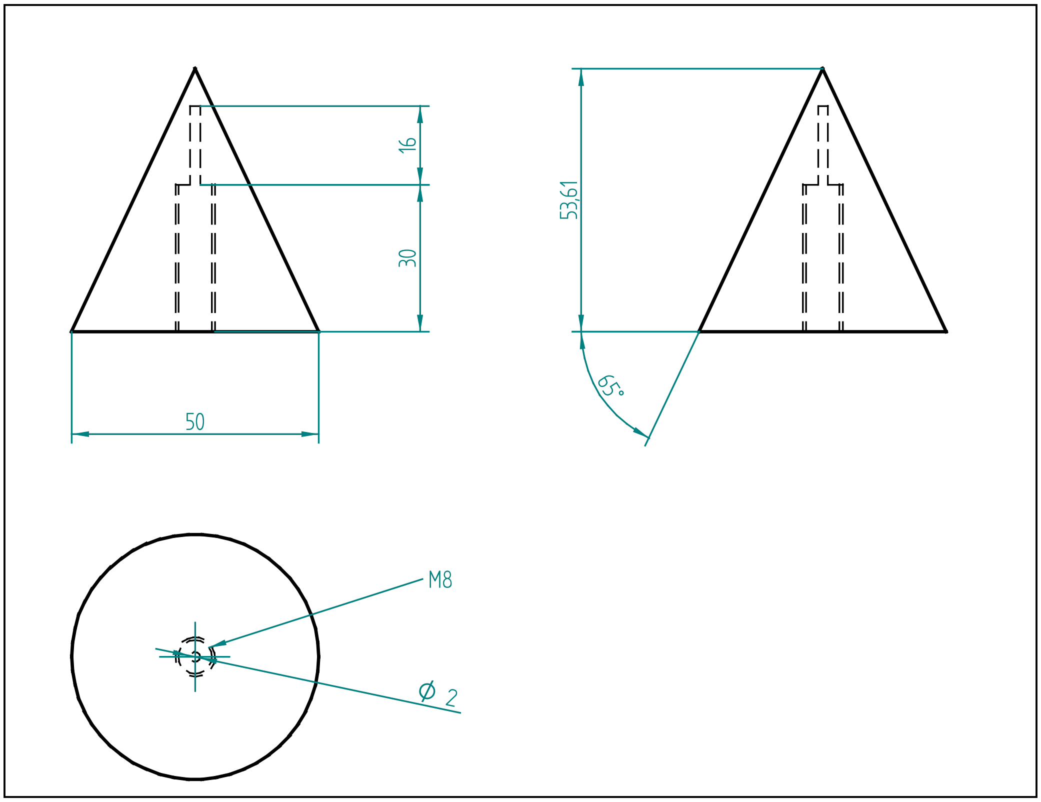

Figure 4.9 Cone 2

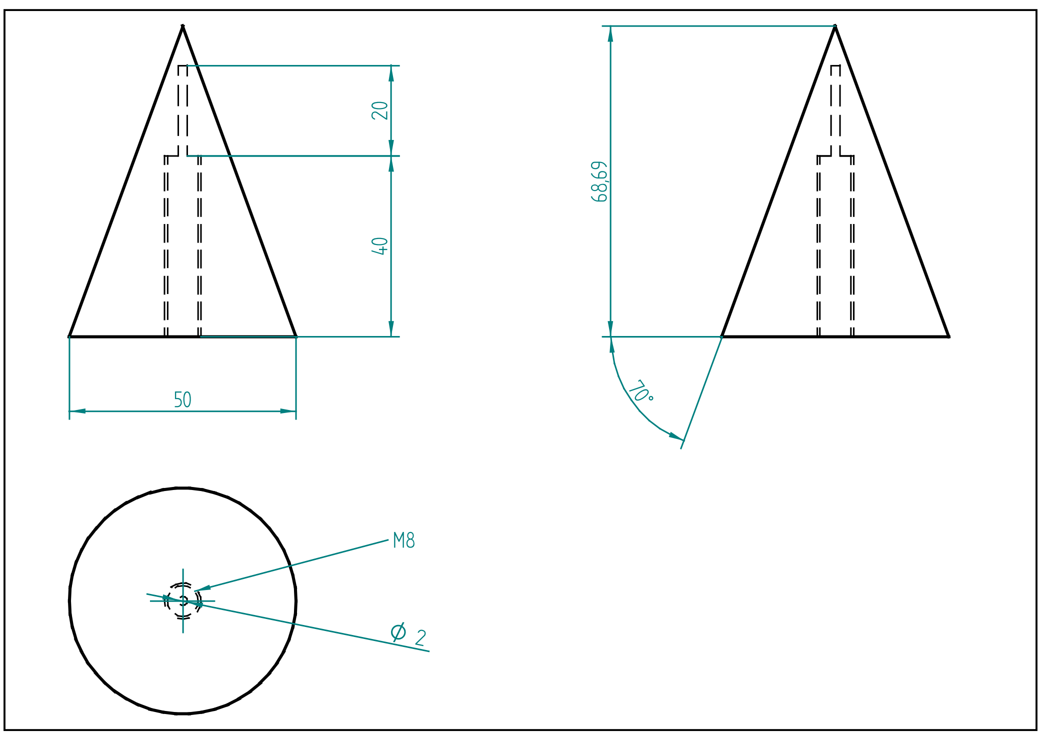

Figure 4.10 Cone 3

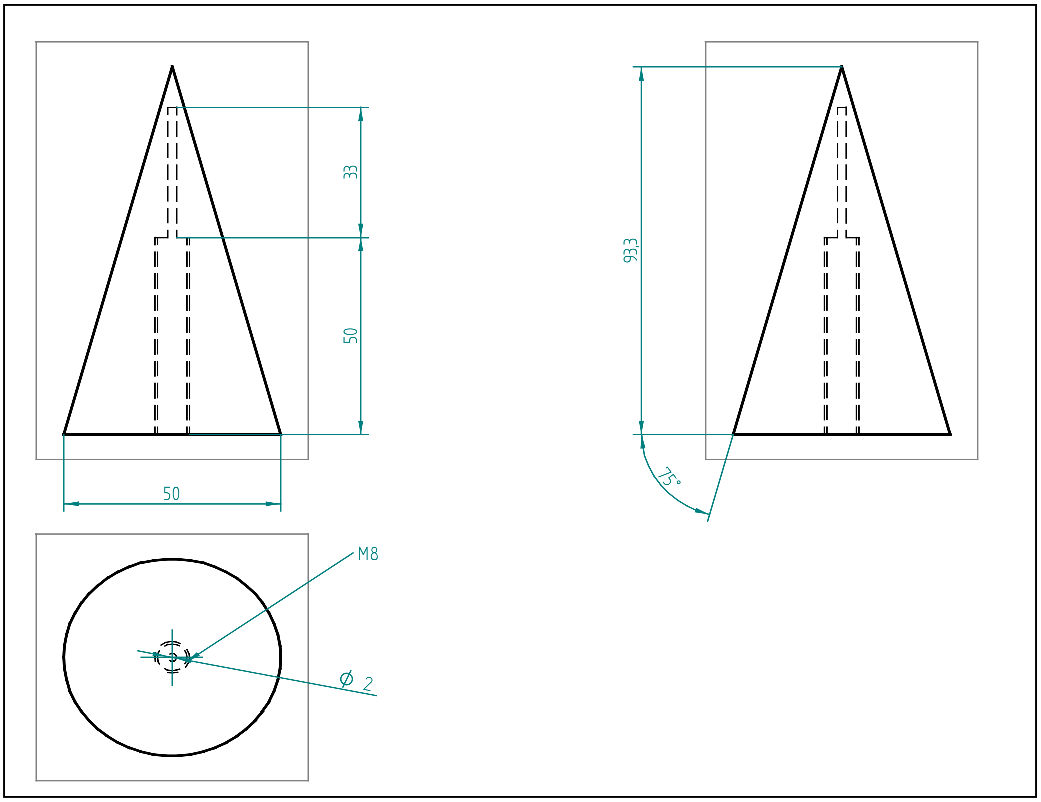

Figure 4.11 Cone 4

4.5 Calibration Procedure

The calibration and testing procedures as well as much of the data analysis have been adapted from Bredin (2002). As stated previously, a process known as deconvolution may be employed to analyse experimental data obtained from a SWDB. Deconvolution requires the system characteristics in the form of the impulse response to be known in order to convert measured strain into applied load. One may obtain the impulse response by generating a step change in the input to the system. This procedure is outlined in Section 3.4. The method utilised to create a step change in the input involved attaching a wire to the tip of the models to which weights were tied. This pre-stresses the models such that when the wire is cut, the release of the weights creates a step change in the applied load.

4.5.1 Acquisition of Calibration Data

The calibration procedure followed to acquire the impulse response and calibration constant for each cone is outlined below:

1. The drag balance was suspended vertically such that the model could be attached at the bottom. A schematic of the configuration is shown in Figure 4.12.
2. A length of 0.45 mm diameter high tensile wire was passed through the 0.5 mm hole at the apex of the calibration model.
3. A knot was tied in the wire at the base of the model and any excess wire removed.
4. The wire was pulled from the front end of the model until the knot was seated at the start of the 0.5 mm hole.
5. Silicon sealant was injected into the model and allowed to set.
6. A damper screw was inserted into the test model and screwed up against the silicon sealant.
7. The depth to which the damper screw was inserted was recorded. This was important to ensure the configuration of the corresponding test model be kept as close as possible to the calibration model since any differences would affect the stress wave propagation.
8. The model was screwed onto the drag balance until the end of the balance was resting against the damper screw.
9. The strain amplifier and digital storage oscilloscope were switched on and allowed to warm up. The semi-conductor strain gauges required 2 hours to warm up.
10. Weights were suspended at the end of the wire.
11. The oscilloscope was programmed to trigger automatically.
12. The output of the balance was zeroed.
13. The wire was cut approximately 500 mm from the model. Great care was taken to avoid any cutting forces acting along the axis of the balance.
14. The data, along with the total weight suspended from the wire, was recorded for processing.

Steps 5 and 6 were found to be necessary in order to provide adequate damping of vibrations while not negatively influencing the response time of the model. Another factor that needed to be considered was the shape of the step response obtained during calibration. The configuration used yielded the closest response to an ideal step response.

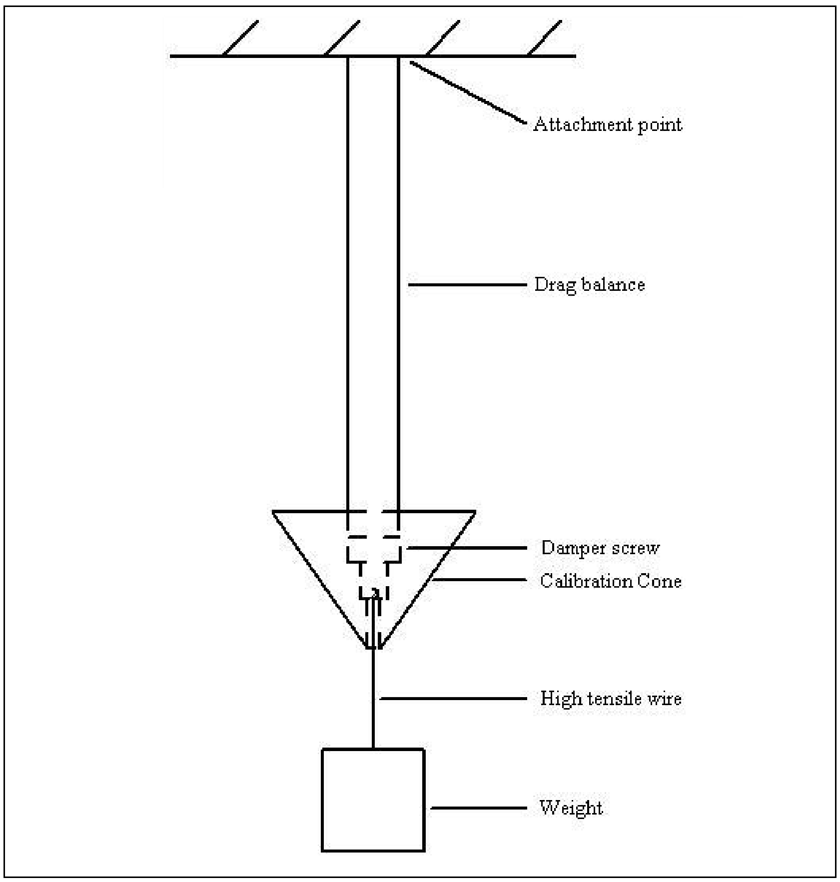

Figure 4.12 Schematic of the calibration configuration

4.5.2 Processing of Calibration Data

Data processing was done using Matlab version 6.5. The Matlab commands are shown in brackets and the functions can be found in Appendix A. The following data processing was required to convert the step response to an impulse response:

1. The data was zeroed. This was necessary since the semi-conductor strain gauges tended to drift significantly between zeroing and the start of data capture.
   ([zerod] = zero100data(data))
2. Data recorded before the wire was cut was removed. The start of the rise was judged manually.
3. The remaining data was filtered by fitting polynomials to each data point together with a number of preceding and subsequent data points. The data required filtering because the deconvolution process amplifies any noise. This was particularly important since electrical noise becomes very apparent at very high sampling rates (10×10^6 samples per second). Noise is further amplified when analogue to digital conversion is required, as was the case since the balance output was an analogue signal with the data being recorded digitally.
4. The polynomials were differentiated to yield the impulse response.
   ([smoothdata,ir] = fullpolyfit2(zerod,time,1,500))
5. The impulse response was filtered again by fitting polynomials.
   ([ir] = fullpolyfit2(ir,time,1,100))
6. Every tenth data point was sampled to get a reduced data set and therefore decrease what would otherwise be a very extensive computational time.
   ([ir] = sample10r(ir))
7. The step response (smoothdata) was deconvoluted using the impulse response (ir) to produce the step input.
   ([force] = deconvolution(ir,smoothdata))
8. The magnitude of the step response (force) needed to be multiplied by a calibration constant, x. This constant was determined by dividing the applied load by the average of the step output.
9. The impulse response and the calibration constant were saved as a Matlab data file to be used in the processing of test data.

4.6 Testing Procedure

4.6.1 Firing of the Shock Tube

The procedure followed for firing the shock tube is outlined below:

1. The main valve to the compressor, located next to the driver section, was opened.
2. It was ensured that all sections were bolted together properly.
3. The steel ring that surrounds the holes cut into the secondary piston was positioned as desired and screwed into place.
4. Port 3 was pressurised and then vented using the hand-operated ball valve labelled 'P3 Forward' on the control panel. The control panel is shown in Figure 4.13.
5. Port 1 and Port 2 were pressurised by opening the valve labelled 'P2 Pressure'.
6. Cavity 1 and the driver section were pressurised slowly by opening the valves labelled 'Driver' and 'P1 Pressure' respectively. The pressure in cavity 1 was always kept about 100 kPa above the driver pressure.
7. When the desired driver pressure was reached, the valves controlling the driver and cavity 1 pressures were closed.
8. Port 1 was vented using the 'P2 Pressure' valve thus initiating a test. The operator of the shock tube would wear earphones and blow a warning whistle just prior to venting port 1.

A schematic of the variable opening time valve, reproduced from Bredin (2002), showing the ports and cavities mentioned above is shown in Figure 4.14. The steel ring surrounding the secondary piston has been omitted from the schematic.

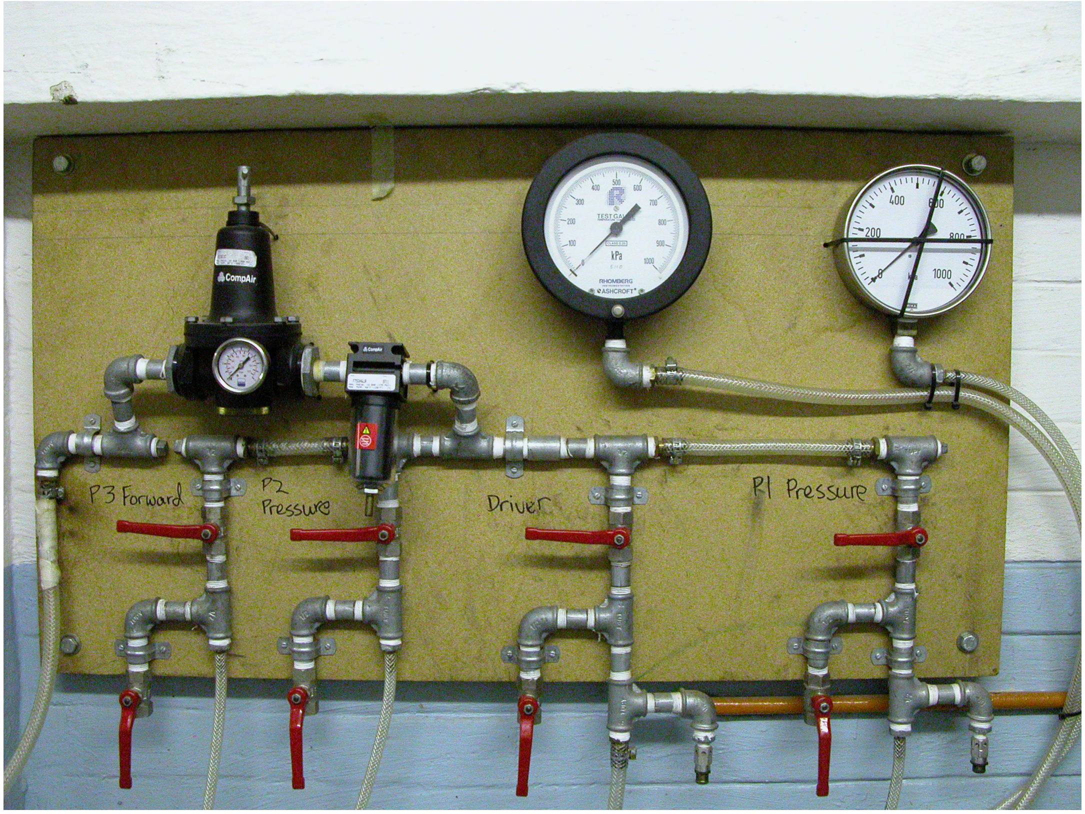

Figure 4.13 The control panel

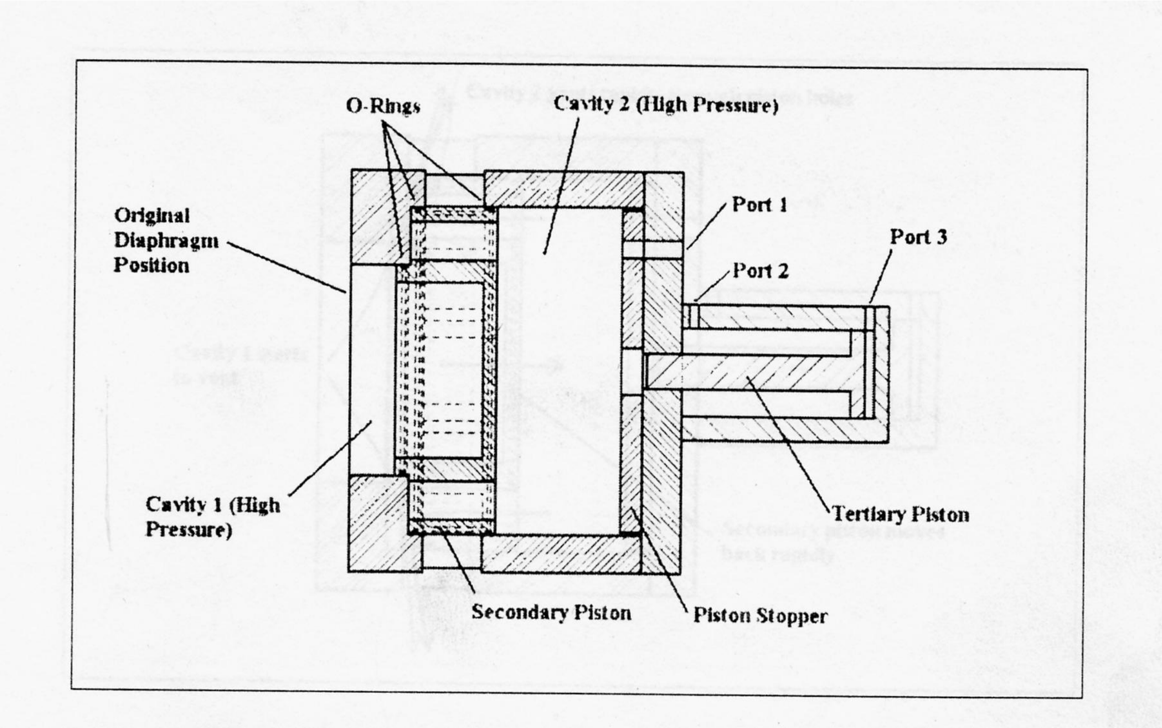

Figure 4.14 The variable opening time valve

4.6.2 Acquisition of Drag Data

The following procedure was employed to collect drag data from the stress wave drag balance:

1. Silicon sealant was injected into the test model.
2. A damper screw was inserted into the test model and screwed to the same depth as the corresponding calibration model.
3. The model was screwed onto the balance until the end of the balance was resting against the damper screw.
4. The strain amplifier and digital storage oscilloscope was switched on and allowed to warm up. The semi-conductor strain gauges required 2 hours to warm up.
5. The oscilloscope was programmed to trigger automatically off the upstream pressure transducer.
6. The output of the drag balance was zeroed.
7. The drag and pressure data was saved for processing. At this point the initial ambient temperature and pressure were also recorded.
8. The shock tube was fired as outlined in Section 4.6.1.

4.6.3 Processing of Drag Data

The following data processing was required to deconvolute the force obtained from the drag balance. The Matlab commands are shown in brackets and the functions can be found in Appendix A.

1. The data was zeroed.
   ([zerod] = zero100data(data))
2. Most of the initial data recorded before the arrival of the shock wave was removed. A small amount of data was retained such that any change in drag could be seen to start from zero.

3. The remaining data was filtered by fitting polynomials as described previously. ([smoothdata] = fullpolyfit2(zerod,time,1,100))
4. Every tenth data point was sampled to get a reduced data set. ([smoothdata] = sample10r(smoothdata))
5. The balance output (smoothdata) was deconvoluted using the impulse response (ir, saved during the calibration procedure) to yield the input force. ([force] = deconvolution(ir,smoothdata))
6. The force was multiplied by the calibration constant, x, saved during the calibration procedure.
7. The force was saved along with the flow properties, the analysis of which will be discussed in the following section.

It is important to note that the processing of the drag data was greatly simplified by including all of the above-mentioned commands in one function called dragb.m. The use of this function will be outlined in the following section.

4.6.4 Analysing the Flow Properties

Analysis of the flow properties involved interpreting the flow measurements, using the method of characteristics outlined in section 3.1.2, as follows:

1. Characteristics at the upstream pressure transducer (see Figure 4.1) were calculated from the upstream pressure measurement.
2. These characteristics were then used to calculate a wave diagram for the downstream flow.
3. The characteristics were interpreted to yield the required flow properties at the test section (axially aligned with the downstream pressure transducer).

The initial temperature, T_0, and pressure, P_0, were used to calculate the initial sound speed, a_0, and density, ρ_0, according to equations 4.1 and 4.2:

$$a_0 = 20\sqrt{T_0} \tag{4.1}$$

$$\rho_0 = \frac{P_0}{287T_0} \tag{4.2}$$

The isentropic relationship, equation 4.3, was used with the static pressure recorded by the upstream pressure transducer, *P*, to calculate the speed of sound, *a*, throughout the test:

$$a = a_0\left(\frac{P}{P_0}\right)^{\frac{\gamma-1}{2\gamma}} \tag{4.3}$$

Equation 4.4, from Thompson (1972), was then used to calculate the flow velocity, *v*:

$$v = \frac{2\left(a - a_0\right)}{\gamma - 1} \tag{4.4}$$

The values of *a* and *v* were then used to create an x-t diagram as far as the test section. Intersecting characteristics were combined such that the velocity of the new characteristic was the mean of the intersecting characteristics.

The start and end of any shock waves were identified manually. The Matlab code was then able to identify the arrival time of the shock at the test section. This data then allowed the exact shock speed, v_s, to be calculated since the distance between the two pressure transducers was constant. The Mach number, *M*, of the test was determined at this point using the following relationship:

$$M = \frac{v_s}{\sqrt{\gamma R T_0}} \tag{4.5}$$

After the downstream characteristics were calculated they were converted back into pressure values. The predicted and measured pressure could then be compared.

The shock waves generated were sufficiently weak to justify using the isentropic compression assumption to calculate the temperature, T, and density, ρ, throughout the test:

$$T = T_0 \left(\frac{P}{P_0} \right)^{\frac{\gamma - 1}{\gamma}} \tag{4.6}$$

$$\rho = \rho_0 \left(\frac{P}{P_0} \right)^{\frac{1}{\gamma}} \tag{4.7}$$

The Sutherland Viscosity Law, from White (1994), was then used to calculate the viscosity, μ:

$$\mu = \mu_0 \left(\frac{T}{T_{int}} \right)^{\frac{3}{2}} \left(\frac{T_{int} + S}{T + S} \right) \tag{4.8}$$

where: μ_0 = 1.71×10^{-5} (kg/ms)

S = 110.4 K (for air)

T_{int} = 273 K

The Reynolds number, Re, of the flow could now be calculated using equation 4.9:

$$Re = \frac{\rho v d}{\mu} \tag{4.9}$$

where d is the maximum diameter of the cone.

The Matlab code used to perform the aforementioned data processing are shown in Appendix A. The functions and commands are explained below. The raw data was recorded using a Yokogawa DL708E digital storage oscilloscope. The oscilloscope was programmed to save the drag on channel 1, the upstream pressure on channel 2 and the downstream pressure on channel 3. The raw data was saved as 'filename.asd', with the filename always 8 characters long.

The first step was to identify any shock waves using **shockpos.m** as follows:

shockpos('filename.asd',1,2)

This function called another function **funprocesspress2.m**. **funprocesspress2.m** reads the data from the raw data file and converts the voltage readings into pressures. The conversions included in the file are for PCB model M102A12 serial number 12833 and 12834 for the upstream and downstream pressure transducers respectively.

The pressures were then passed back to **shockpos.m** which plotted the upstream pressure trace. The user then clicked on the start and end of the shock wave and pressed enter. An output file **spfilename** containing the shock position was saved. The main processing file **dragb.m** was now called as follows:

dragb(filename,P_0,T_0 ,cone)

As stated previously P_0 and T_0 are the initial ambient pressure and temperature recorded before each test. The user was required to enter the cone number used for the particular test so that the correct calibration file would be called. **dragb.m** called all the flow processing functions as well as the deconvolution functions.

4.7 CFD Modelling of the Flow Fields

The CFD modelling of the flow fields were performed using the commercially available code Fluent 6.1.22©. The pre-processor used for geometry modelling and mesh generation was Gambit, supplied as part of the Fluent package.

The flow fields were modelled as 2-Dimensional Axisymmetric problems. The Coupled Explicit solver was chosen. The choice of solver determines the way that the continuity, momentum, and (where appropriate) energy and species equations are solved. The coupled solver solves these equations simultaneously (i.e., coupled together). The explicit solver means that for a given variable, the unknown value in each cell is computed using a relation that includes only existing values.

The Unsteady Time option was used since the flows being modelled were all time-dependent. The Explicit formulation was employed as this selection is recommended for capturing the transient behaviour of moving waves, such as shocks. Solution dependent gradient adaption was utilised to refine the grid and therefore improve the precision of the results.

The Standard k - ε model was selected as the viscous model. This model is a fully turbulent semi-empirical model. Initial simulations were performed using inviscid calculations and very little difference was noted. It was thus decided that the choice of viscous model was not critical and thus no attempt was made to resolve the boundary layers on the models.

5 Experimental and Computational Results

5.1 Calibration Results

The results for the calibration of each cone, in the form of the step response and impulse response, are shown in the Figures 5.1 through 5.8. The calibration constant for each cone, obtained by dividing the applied load by the average of the step output is shown in Table 5.1. The applied load was 139.29 N while the high tensile wire was cut approximately 500 mm below the models.

Table 5.1 Calibration Constants

Cone	Calibration Constant, x
1	1.4175×10^{8}
2	1.5327×10^{8}
3	1.5508×10^{8}
4	1.6171×10^{8}

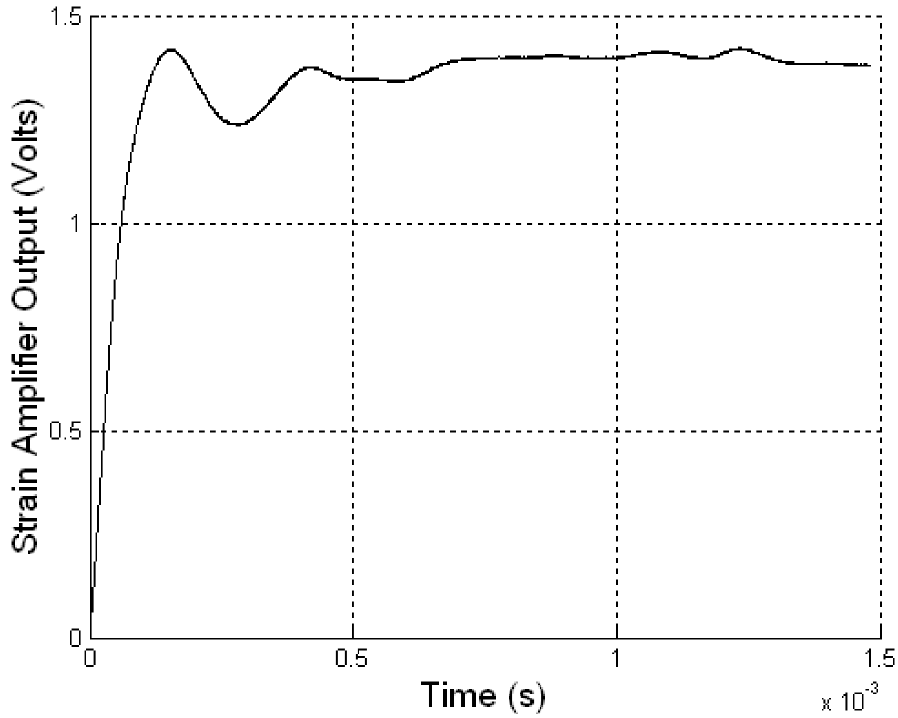

Figure 5.1 Step Response for Cone 1

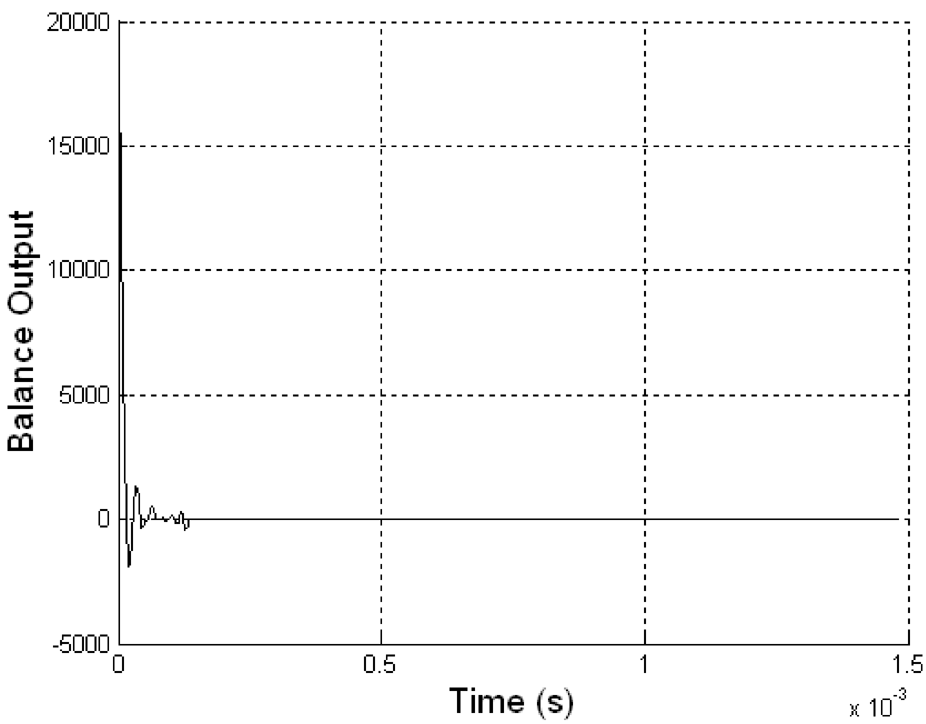

Figure 5.2 Impulse Response for Cone 1

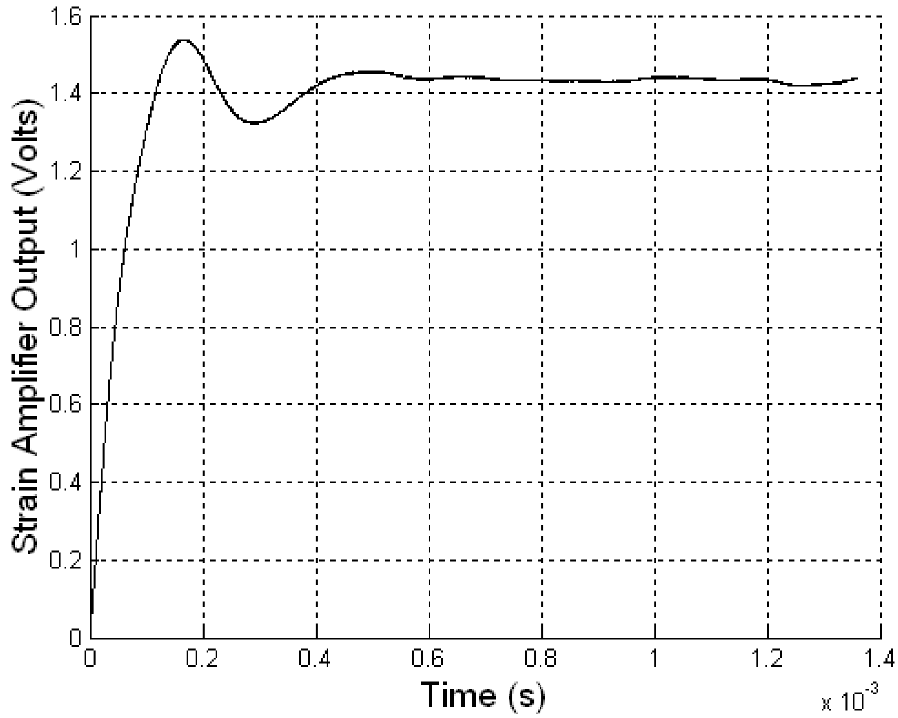

Figure 5.3 Step Response for Cone 2

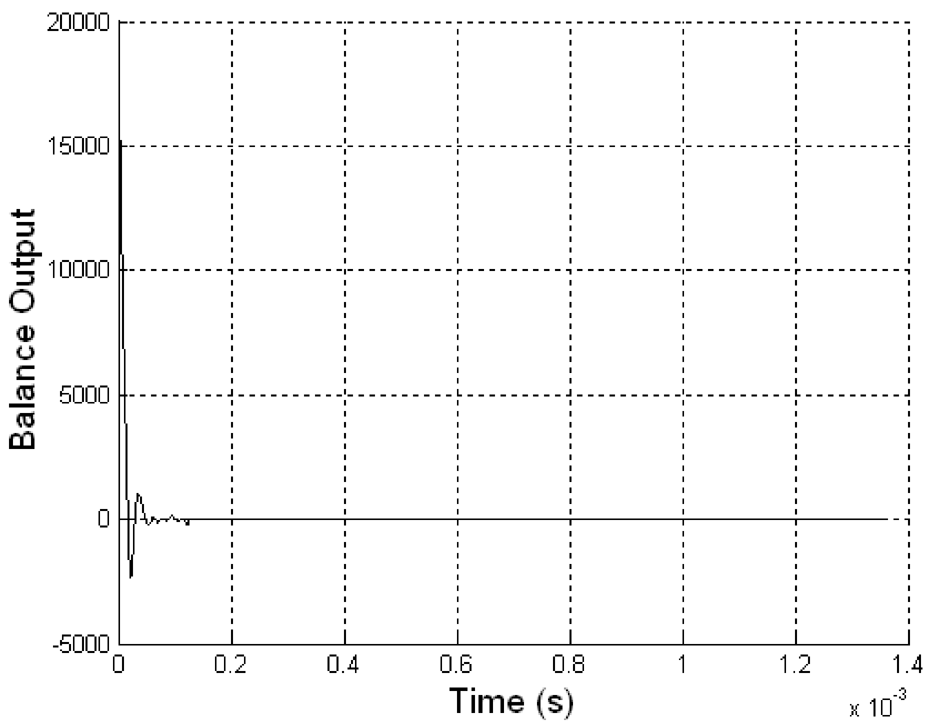

Figure 5.4 Impulse Response for Cone 2

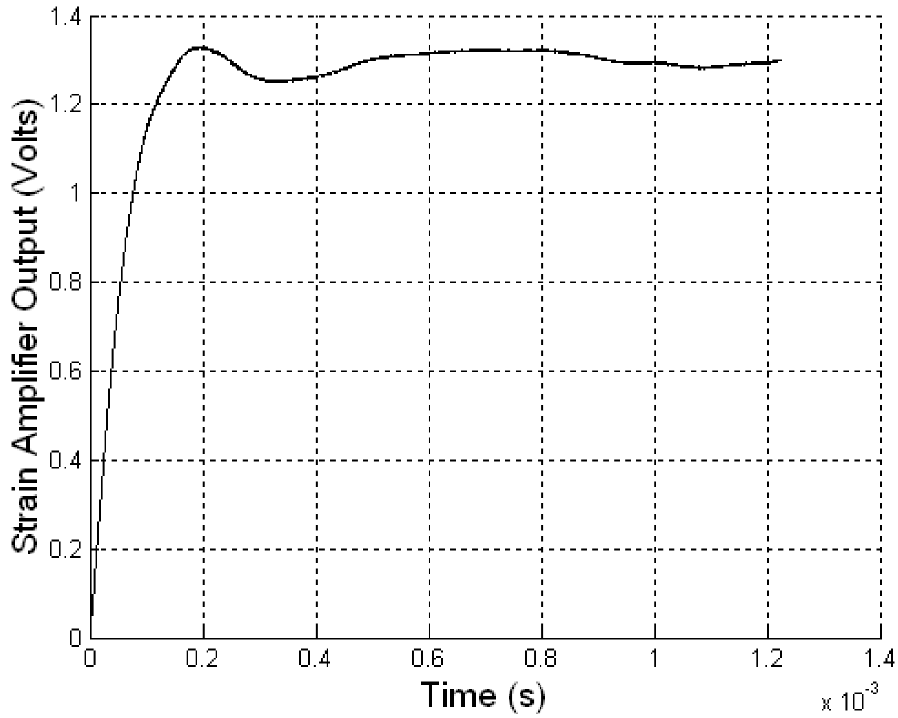

Figure 5.5 Step Response for Cone 3

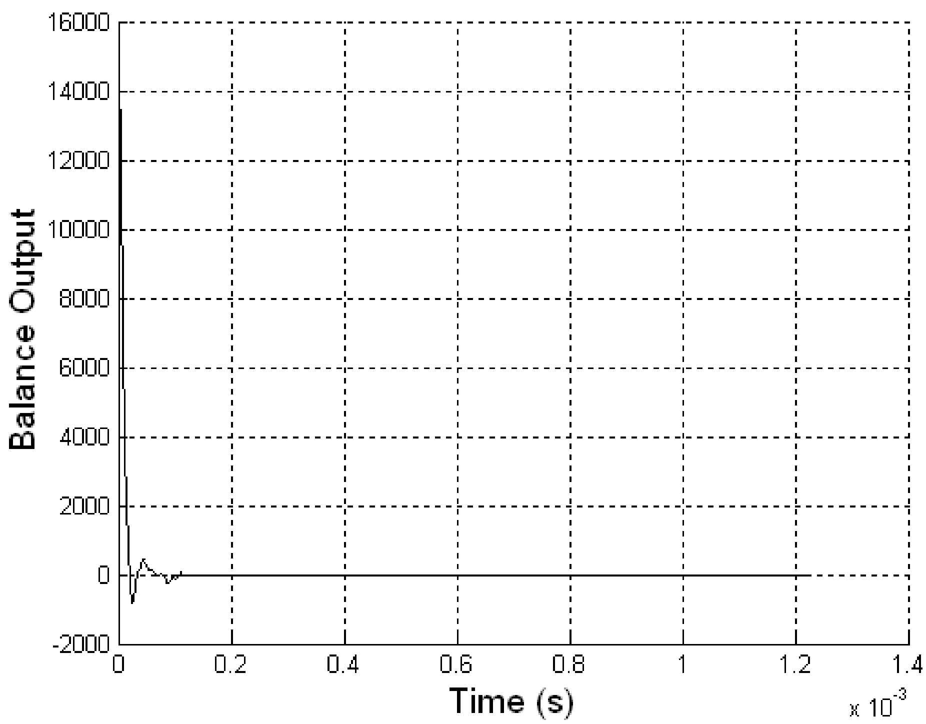

Figure 5.6 Impulse Response for Cone 3

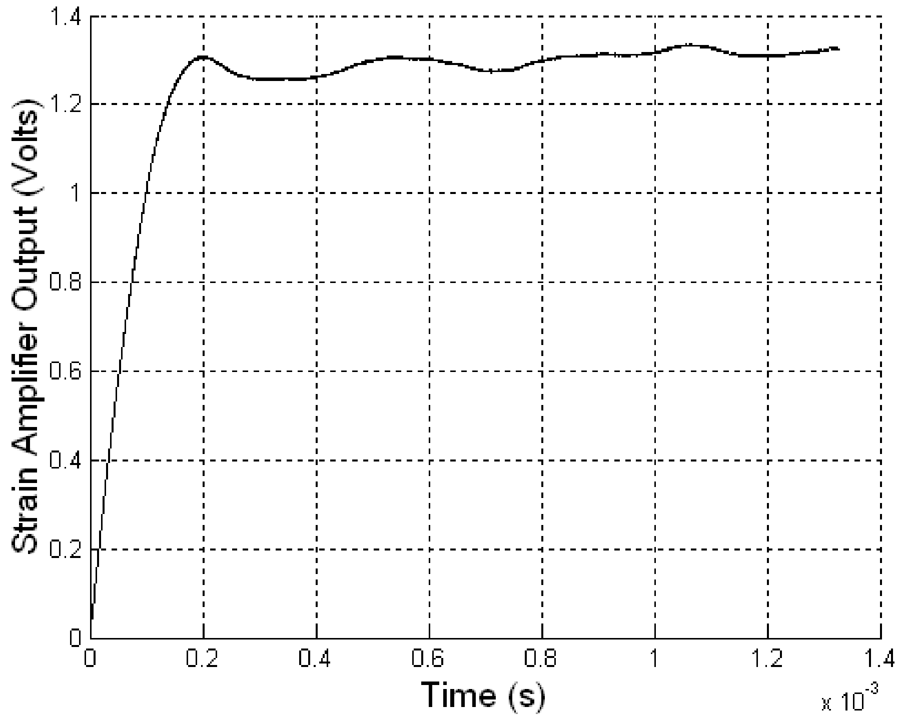

Figure 5.7 Step Response for Cone 4

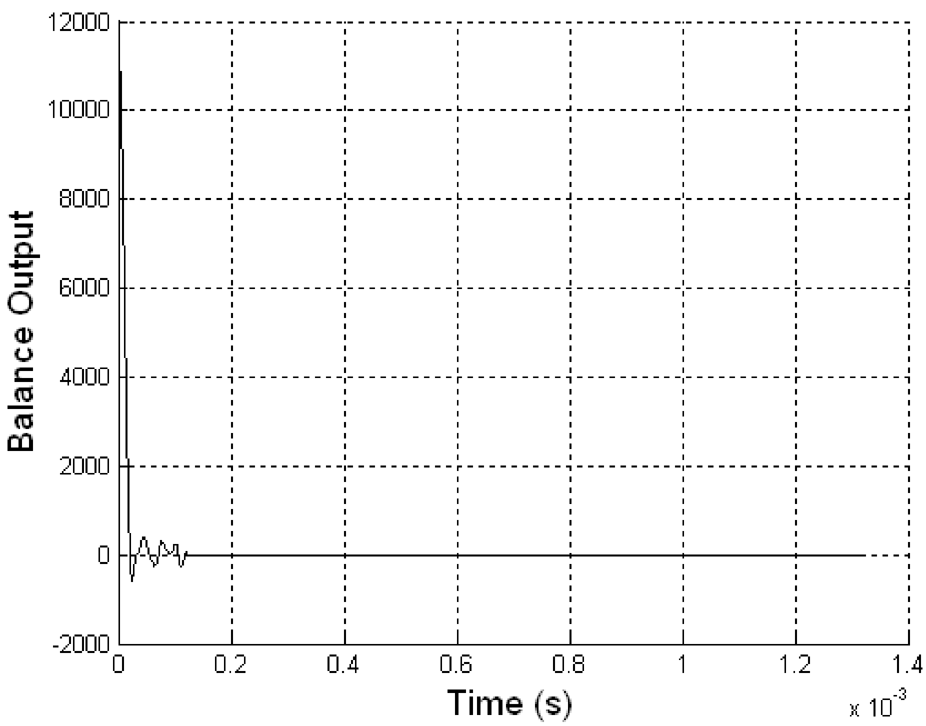

Figure 5.8 Impulse Response for Cone 4

5.2 Experimental Results

The following results (Figures 5.11 through 5.14) represent the combined drag data, obtained experimentally, for each cone. The Mach numbers indicated in these figures are shock wave Mach numbers. Individual drag data and corresponding Reynolds Number plots (as well as the initial temperature and pressure) for each test can be found in Appendix B. An example of the drag and Reynolds Number plots are shown in Figures 5.9 and 5.10 respectively:

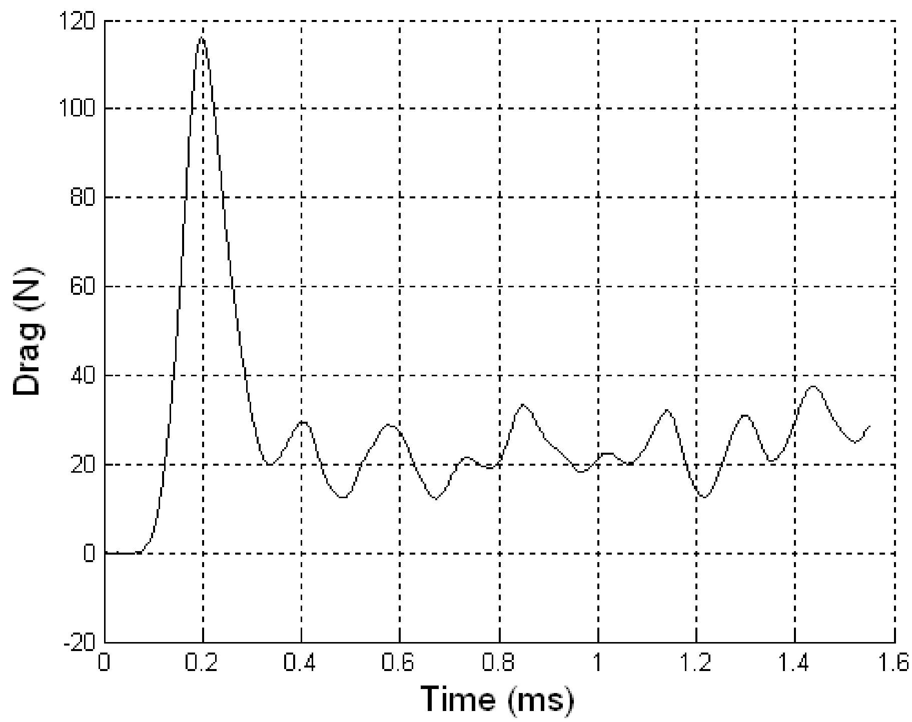

Figure 5.9 Drag on Cone 1 ($M_s = 1.24$; $T_0 = 297K$; $P_0 = 82930Pa$)

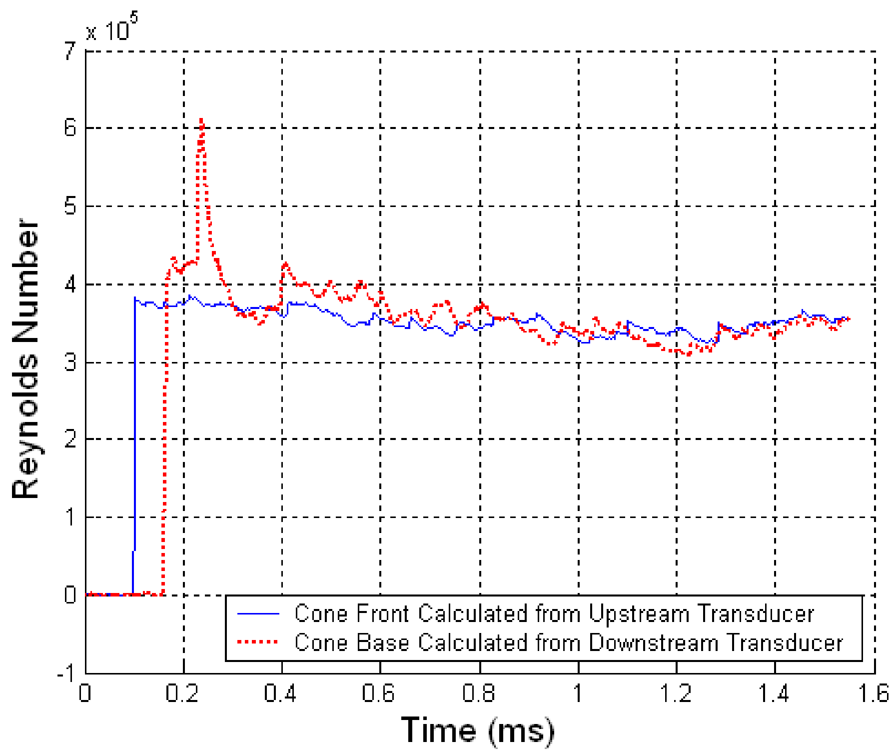

Figure 5.10 Reynolds Number Plot ($M_s = 1.24$; $T_0 = 297K$; $P_0 = 82930Pa$)

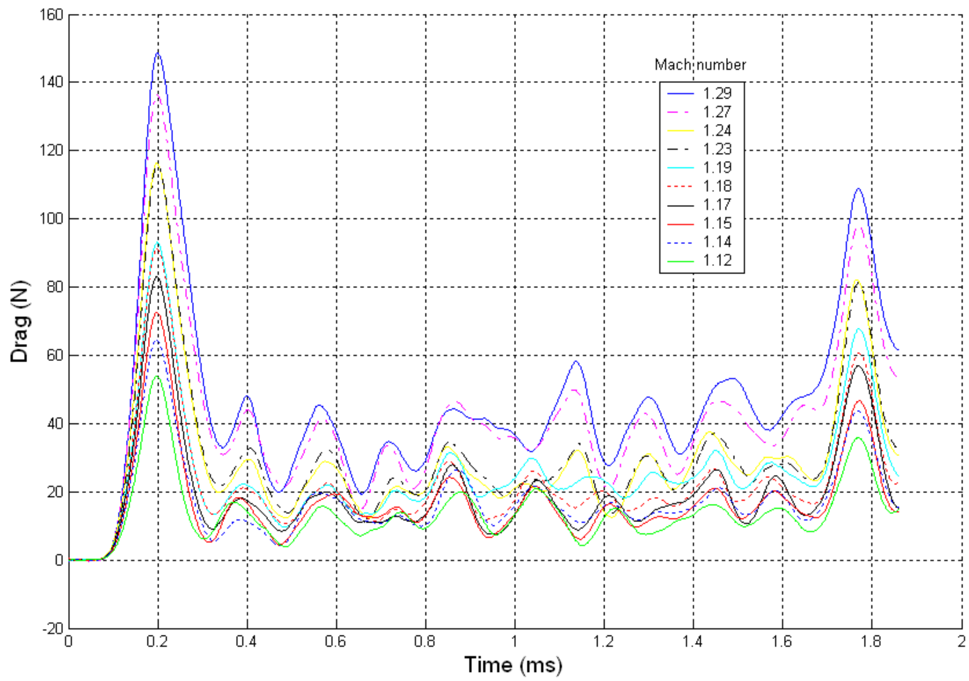

Figure 5.11 Experimental Results – Drag on Cone 1

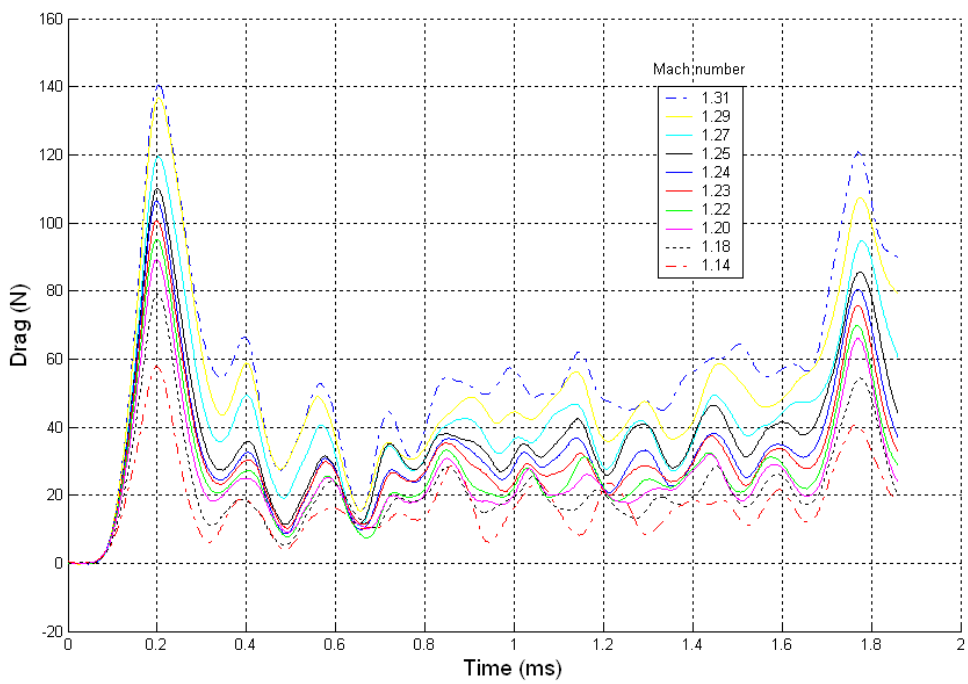

Figure 5.12 Experimental Results – Drag on Cone 2

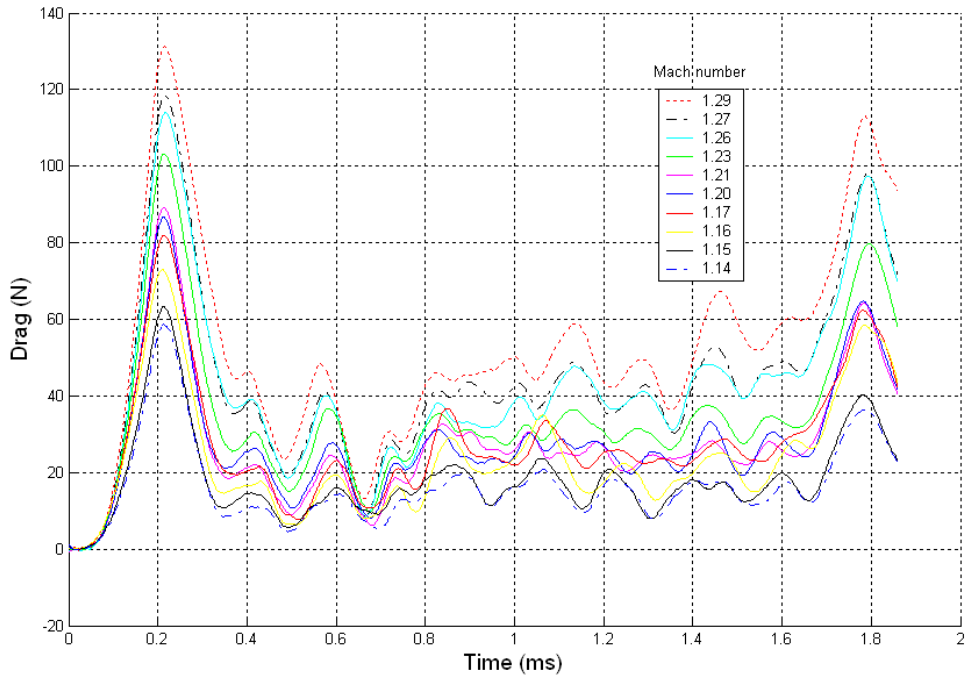

Figure 5.13 Experimental Results – Drag on Cone 3

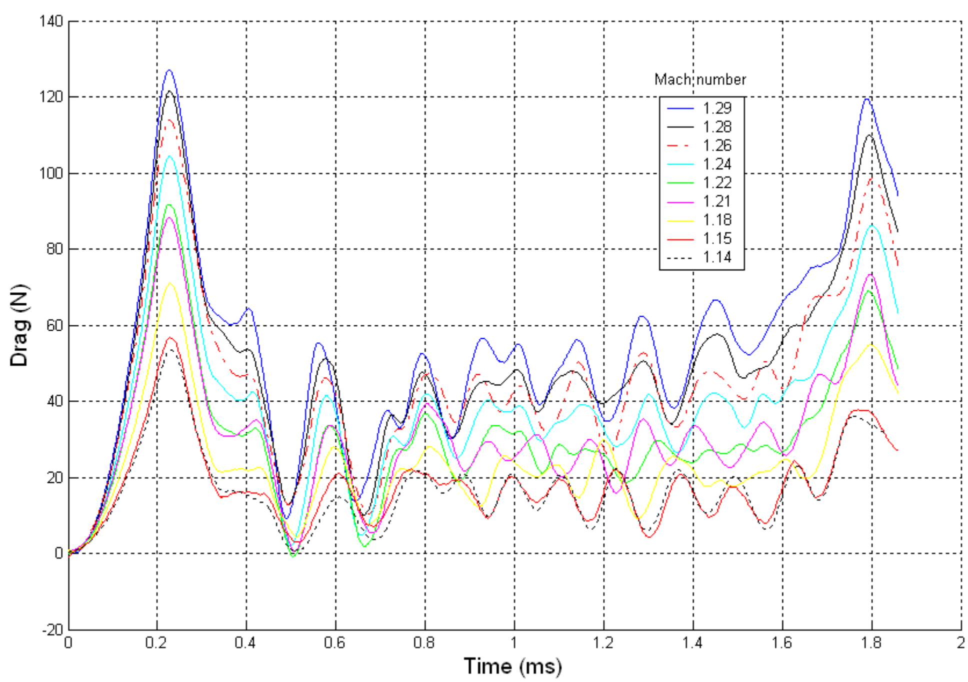

Figure 5.14 Experimental Results – Drag on Cone 4

The following figures show the variation in the experimentally measured drag between the different cones where the shock Mach number has been kept constant.

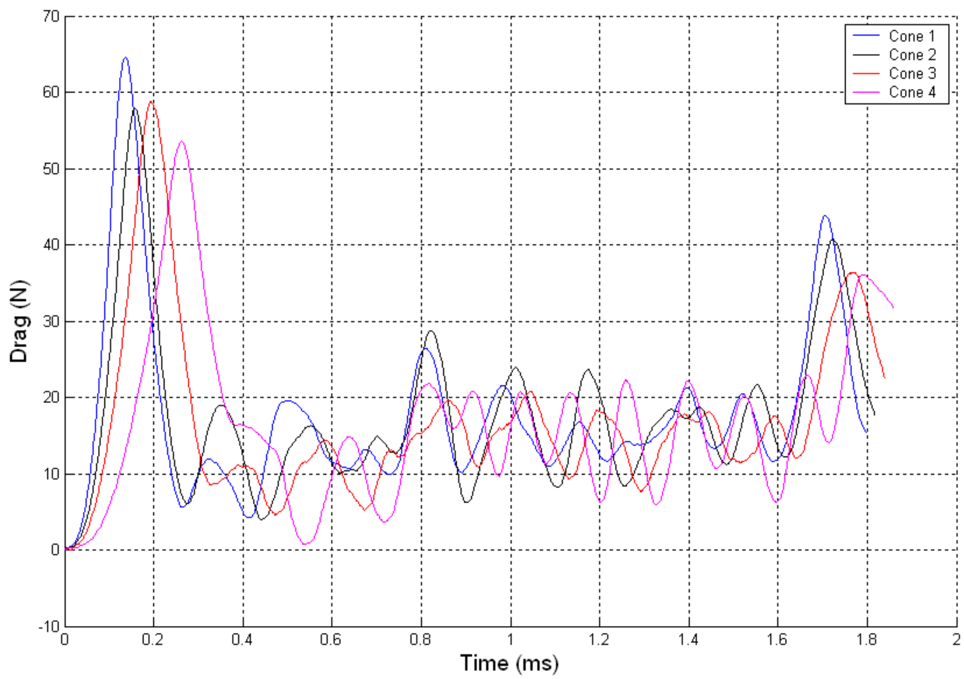

Figure 5.15 Experimental Results – Mach 1.14

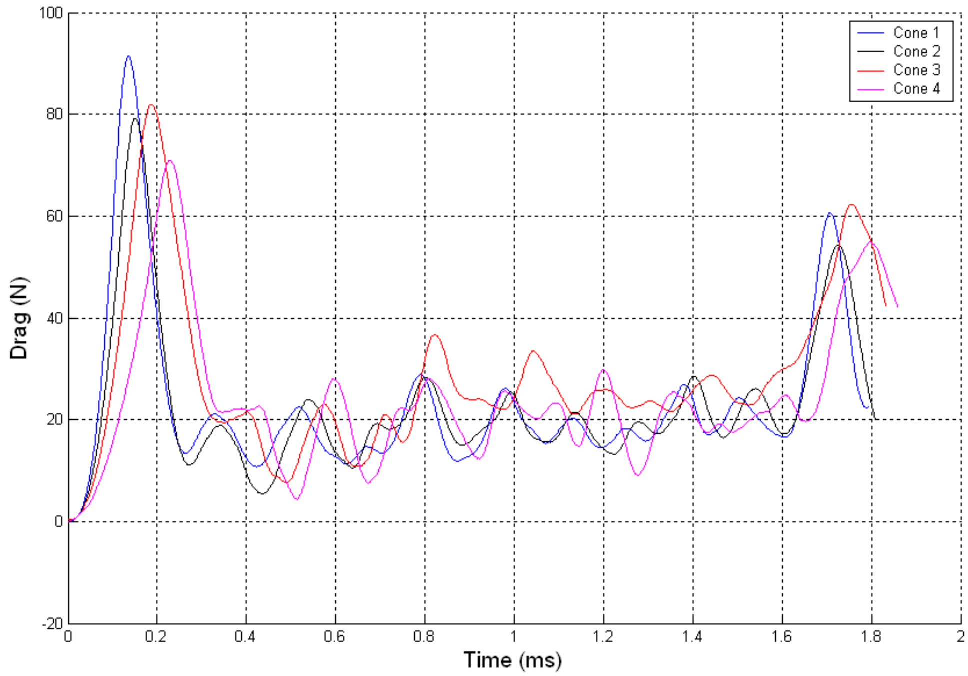

Figure 5.16 Experimental Results – Mach 1.18

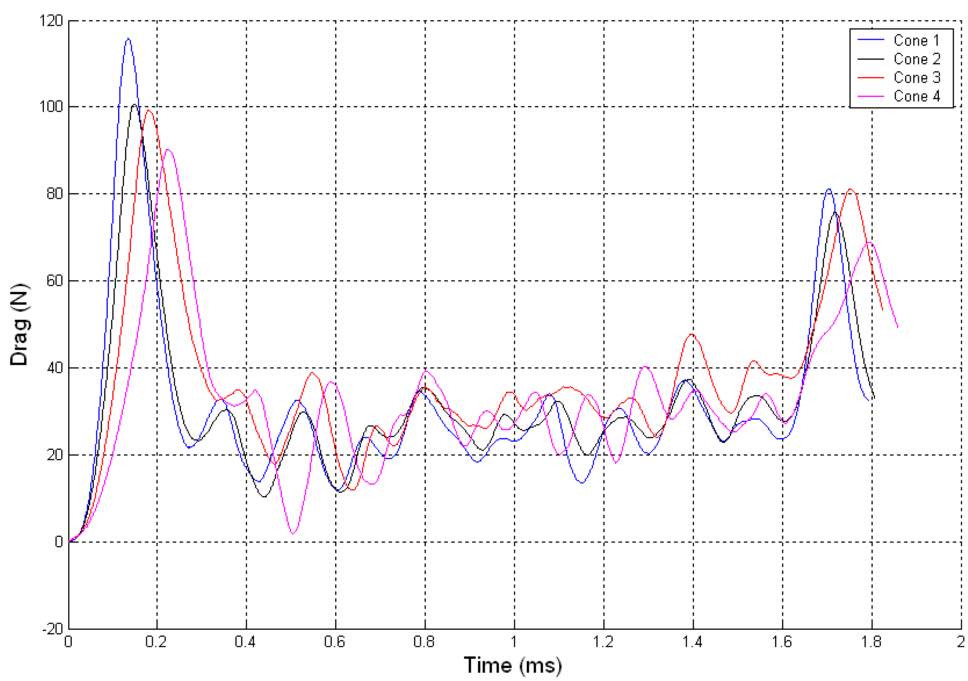

Figure 5.17 Experimental Results – Mach 1.23

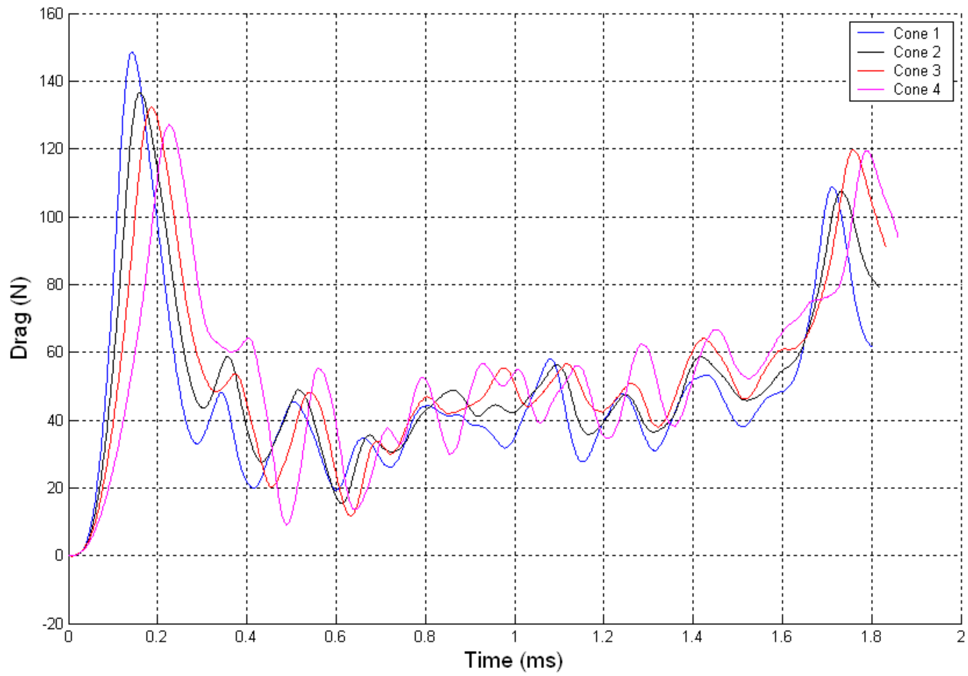

Figure 5.18 Experimental Results – Mach 1.29

5.3 Computational Results

The following sets of results were obtained using the Fluent CFD code. Figures 5.19 through 5.26 represent results in which the initial ambient temperature and pressure were kept constant. The initial temperature was set at 300 K and the pressure at 83500 Pa. The simulations were then set up to produce shocks with Mach numbers ranging from 1.3 to 1.5. Figure 5.19 represents drag obtained for a sphere of diameter 50 mm, while the rest of the figures refer to the cones corresponding to the experimental models. The cone data has been combined to show the relationships between drag and Mach number and drag and cone number.

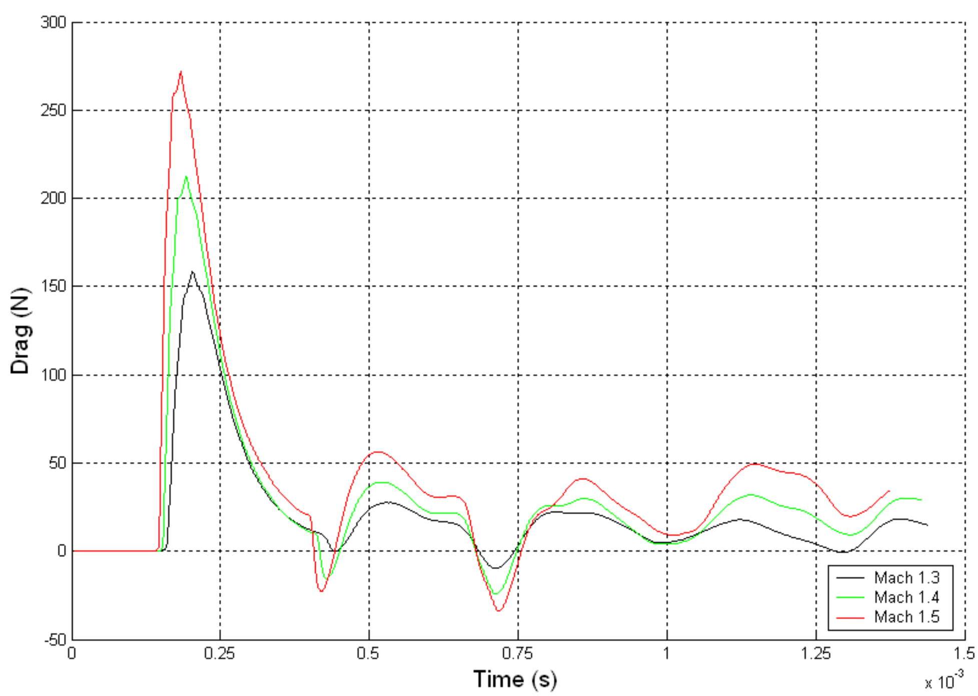

Figure 5.19 CFD Results – Drag on 50 mm diameter Sphere

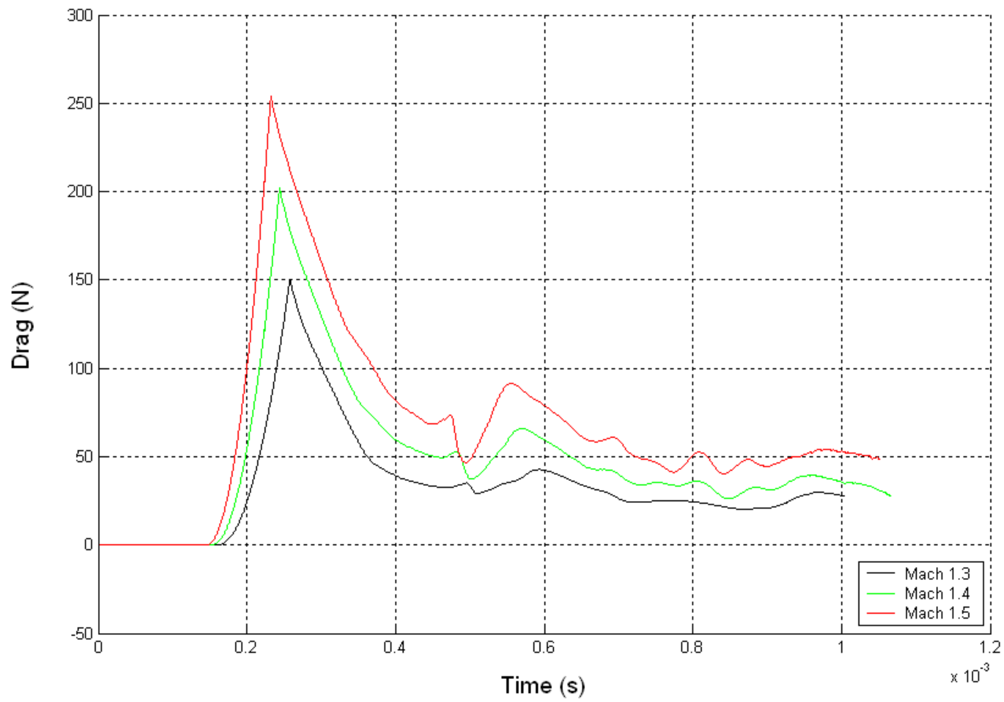

Figure 5.20 CFD Results – Drag on Cone 1

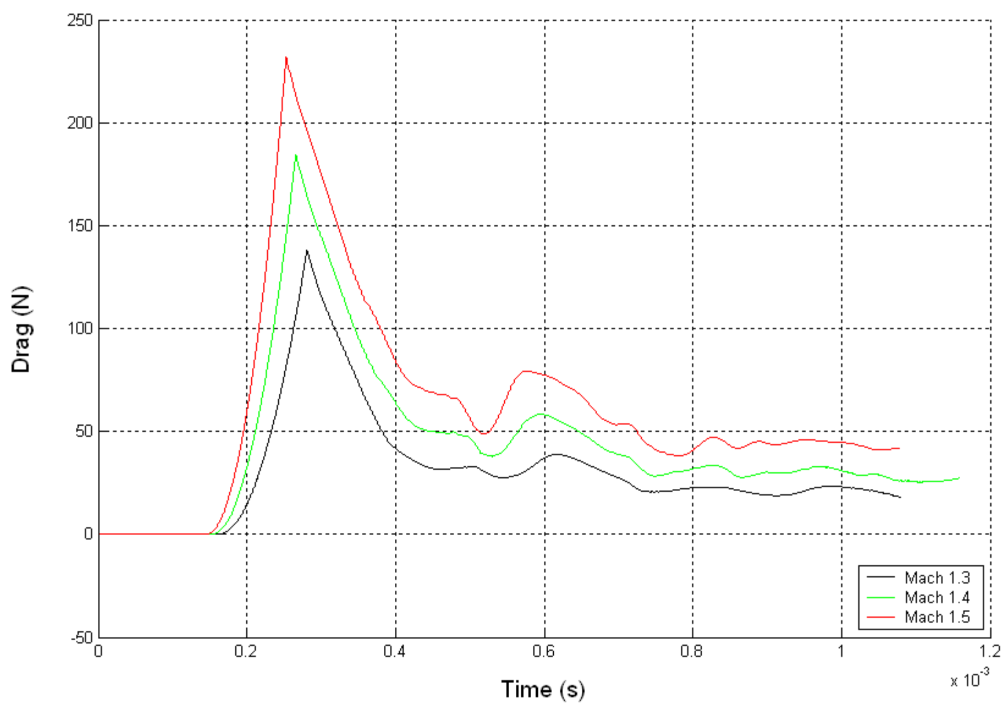

Figure 5.21 CFD Results – Drag on Cone 2

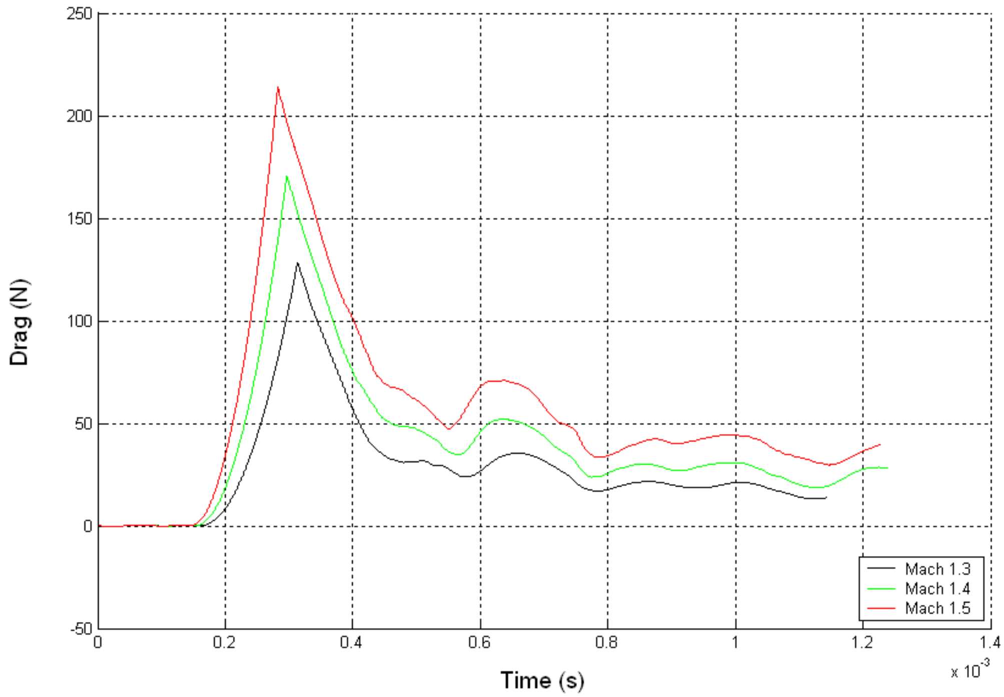

Figure 5.22 CFD Results – Drag on Cone 3

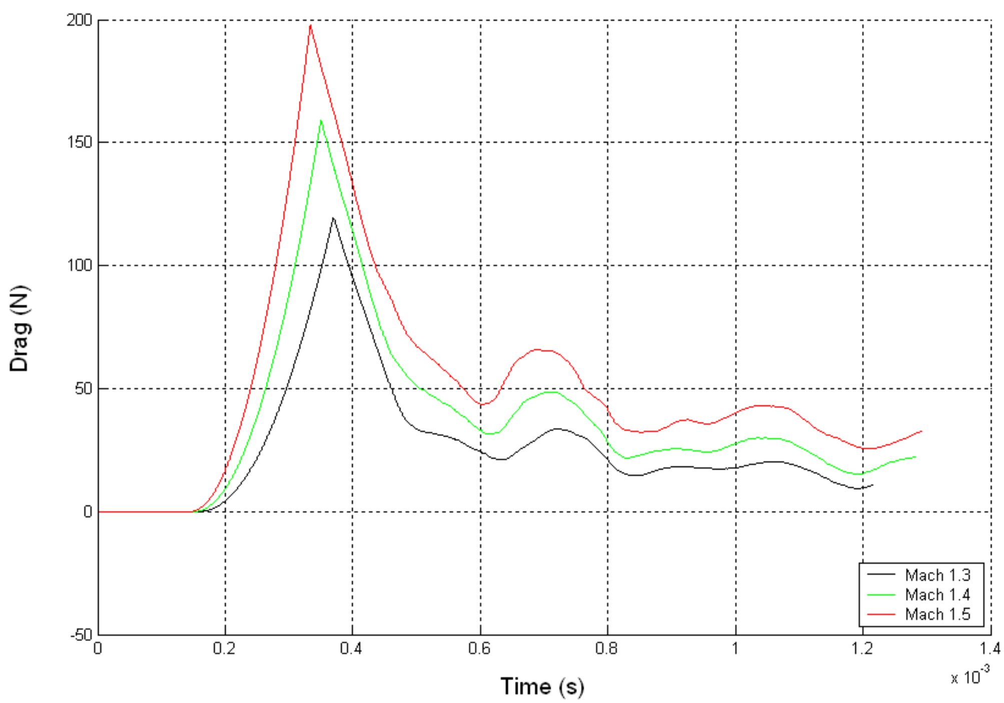

Figure 5.23 CFD Results – Drag on Cone 4

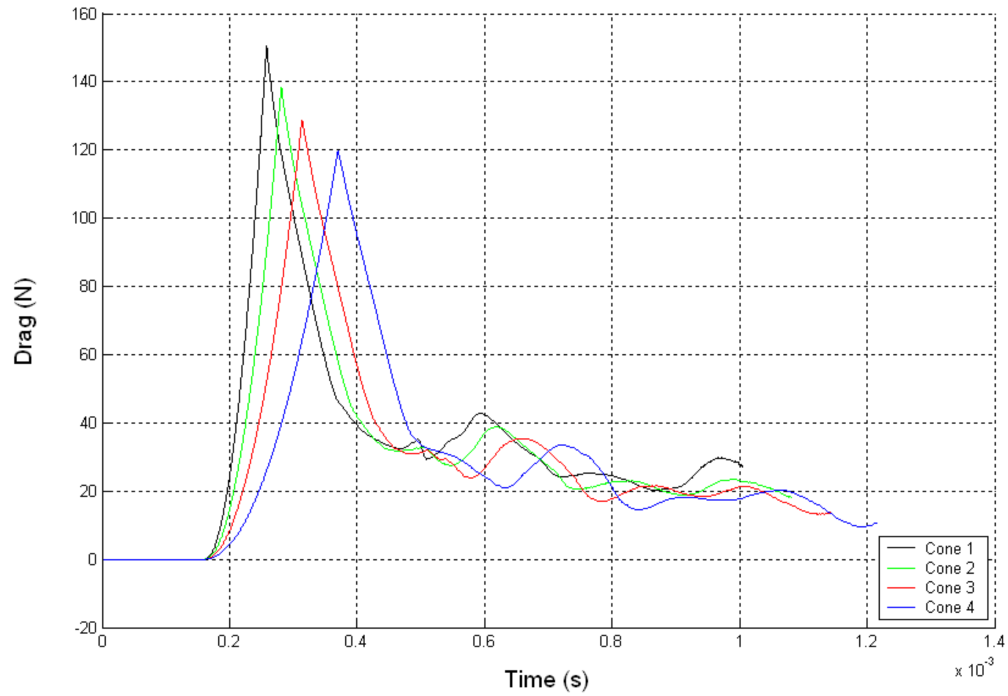

Figure 5.24 Combined CFD Results – Mach 1.3

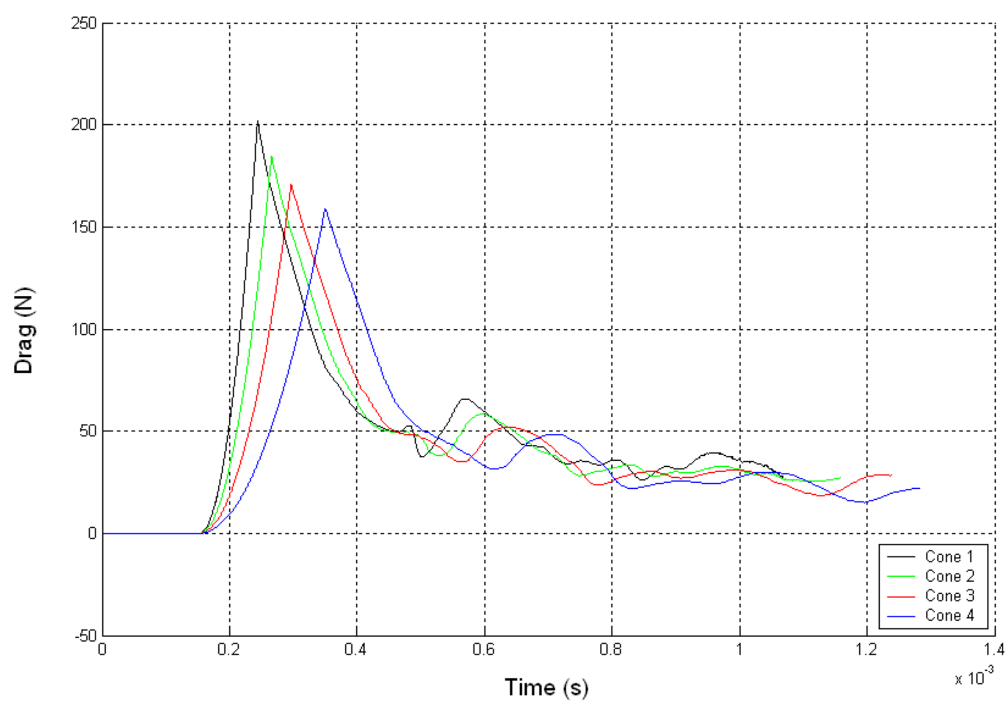

Figure 5.25 Combined CFD Results – Mach 1.4

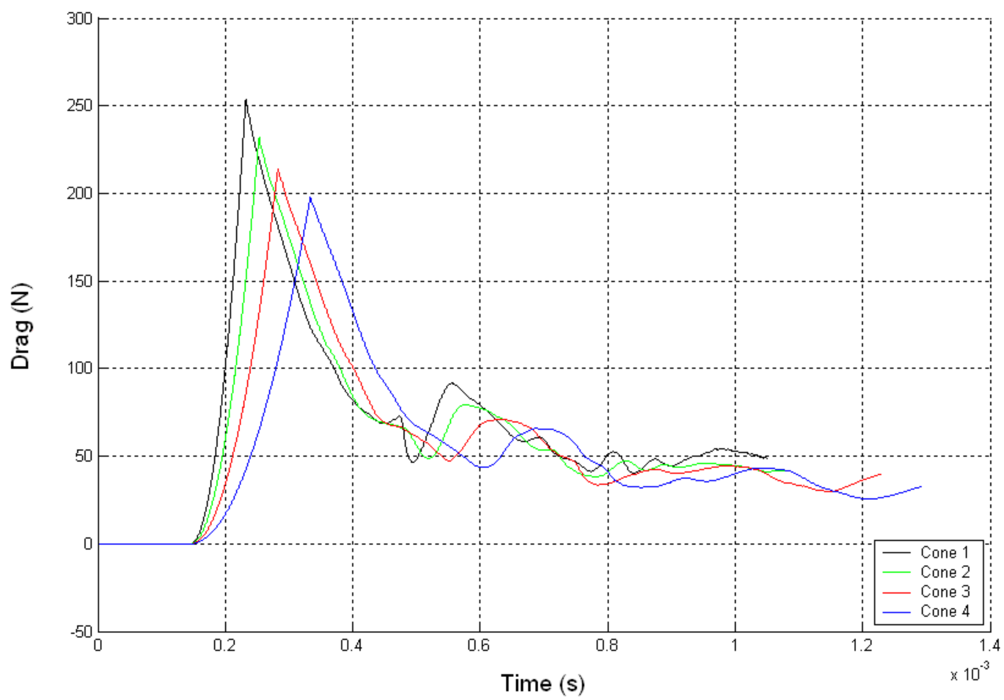

Figure 5.26 Combined CFD Results – Mach 1.5

5.4 Combined Experimental and Computational Results

The following results show drag obtained experimentally combined with drag obtained from CFD simulations. The initial ambient pressure, P_0, and temperature, T_0, recorded during experimentation were applied to the corresponding simulations. The results include the steady state drag. The steady state drag was calculated using the following equation:

$$Drag = C_D \frac{\rho_2}{2} V_2^2 \pi \frac{d^2}{4} \qquad (5.1)$$

where:

	ρ_2	=	free stream density
	V_2	=	free stream velocity
	d	=	maximum diameter (50 mm for each cone)
	C_D	=	steady state drag coefficient

It is important to note that the flow properties downstream of the incident shock are required to calculate the steady state drag. The free stream density and velocity were calculated as follows. The velocity of the gas relative to the shock, V_2, was first calculated using Equation 5.2:

$$\frac{V_2}{V_1} = \frac{\rho_1}{\rho_2} = \frac{1 + 0.2M_1^2}{1.2M_1^2} \tag{5.2}$$

The initial density, ρ_1, ahead of the shock was calculated as follows:

$$\rho_1 = \frac{P_0}{287T_0} \tag{5.3}$$

The shock velocity, V_1, was obtained during testing by simply dividing the time taken for the shock wave to pass between the upstream and downstream pressure transducers by the distance between the transducers. The velocity of the gas relative, V_y, to the cone could now be obtained by subtracting V_2 from V_1.

The steady state drag was obtained for compressible and incompressible flow. The compressible steady state drag refers to the drag that would occur under steady compressible flow with a post shock Mach number corresponding to the unsteady case. The compressible steady state drag coefficient, $C_{D\text{-}C}$, was obtained from steady state CFD simulations, using the same grids as in the unsteady cases above, and is a function of the post shock Mach number, M_y, and the half-vertex angle, ε. Post shock Mach numbers, calculated using Equation 5.4, ranged from 0.183 to 0.415.

$$M_y = \frac{V_y}{\sqrt{\gamma R T_2}} \tag{5.4}$$

The range of compressible steady state drag coefficients for each cone is shown in Table 5.2.

Table 5.2 Compressible Steady State Drag Coefficients

Cone	Drag Coefficient, $C_{D\text{-}C}$
1	1.39 – 1.03
2	1.18 – 0.90
3	0.99 – 0.78
4	0.81 – 0.64

The incompressible steady state drag coefficient, $C_{D\text{-}I}$, representing the drag force in uncompressed fluid flow at corresponding Reynolds numbers, for each cone was obtained from Figure 3.6 (Hoerner (1965)) and is shown in Table 5.3.

Table 5.3 Incompressible Steady State Drag Coefficients

Cone	Drag Coefficient, $C_{D\text{-}I}$
1	0.50
2	0.47
3	0.43
4	0.39

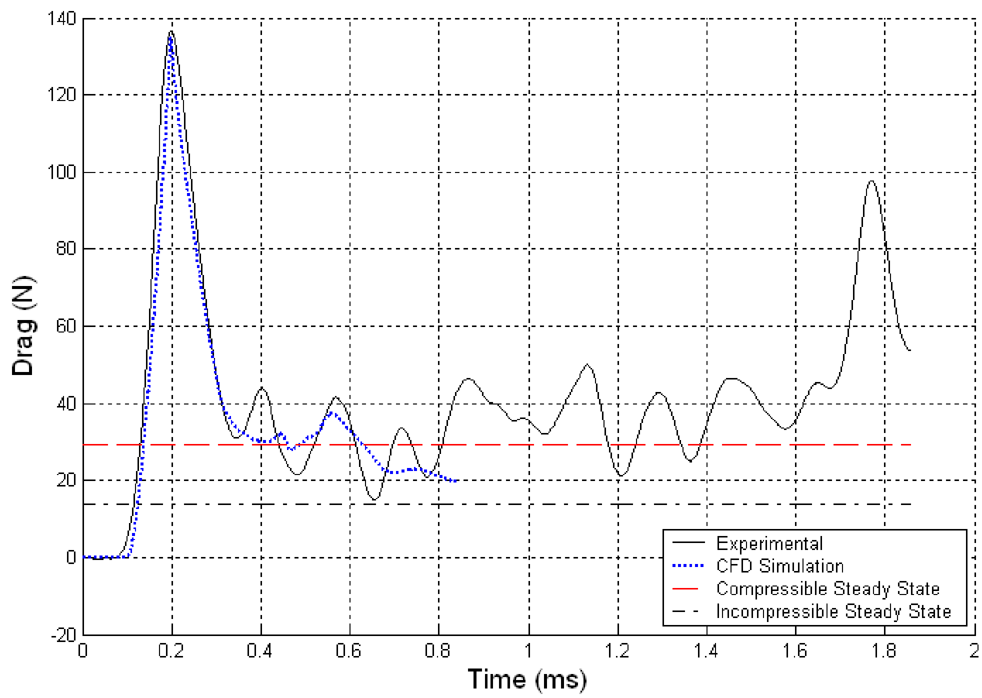

Figure 5.27 Combined Drag Results – Cone 1 Mach 1.27

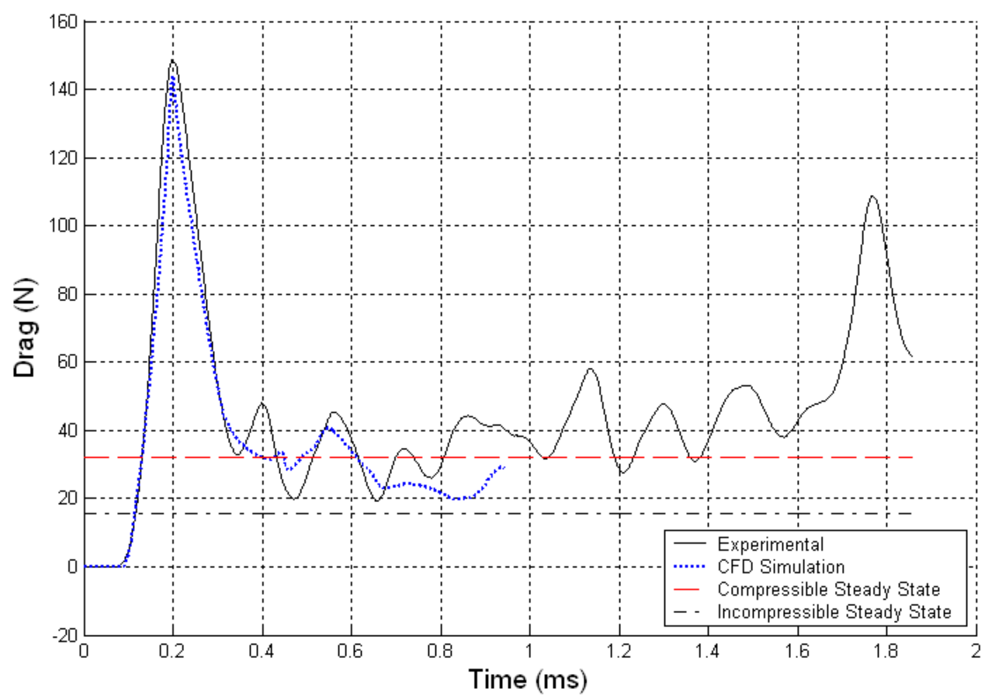

Figure 5.28 Combined Drag Results – Cone 1 Mach 1.29

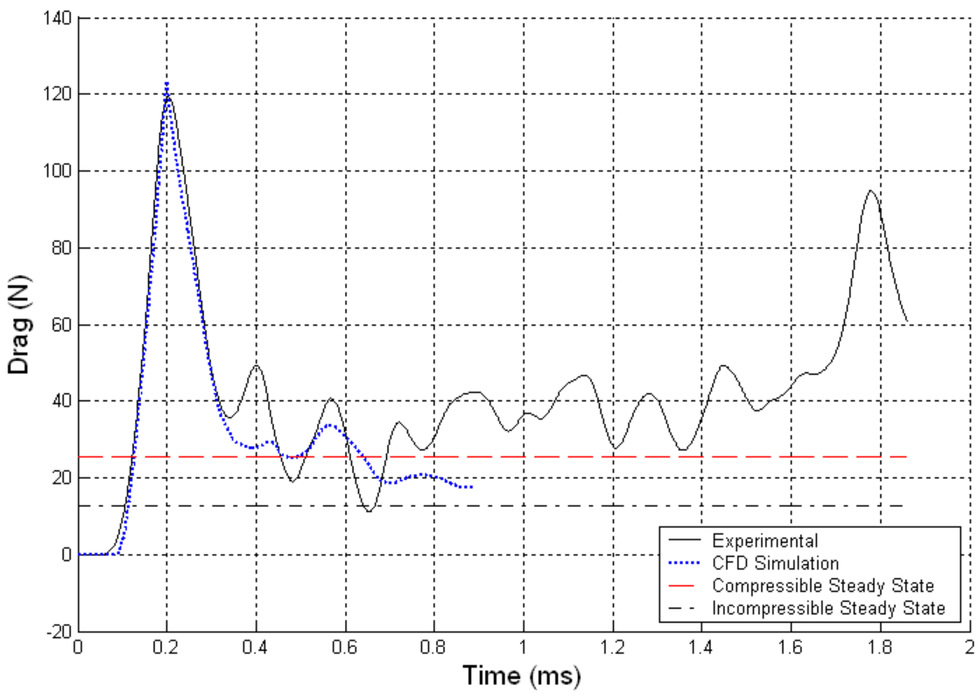

Figure 5.29 Combined Drag Results – Cone 2 Mach 1.27

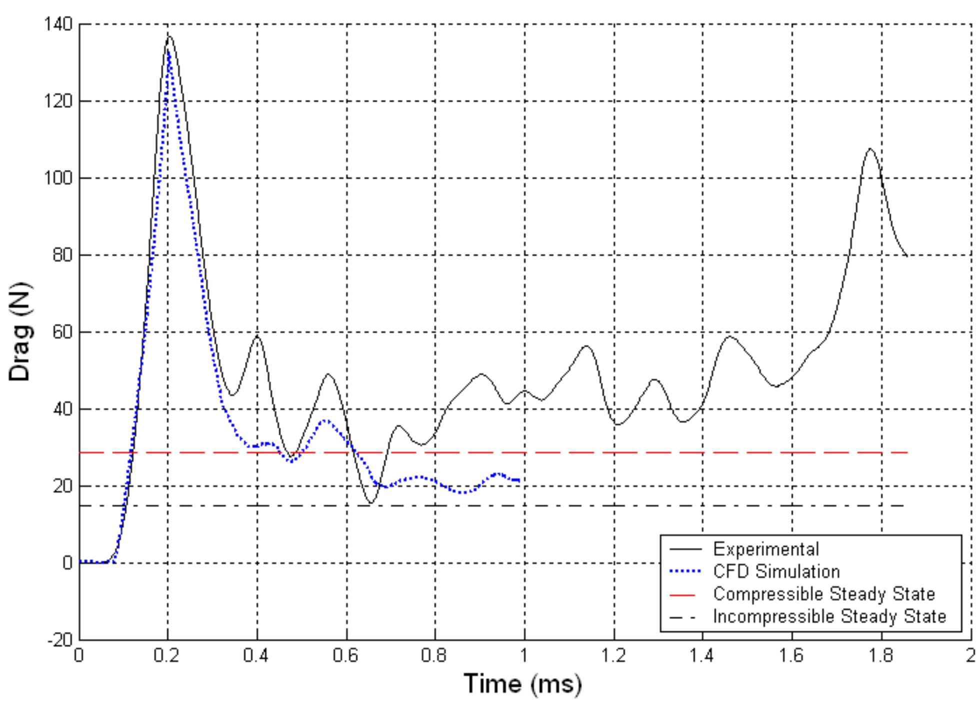

Figure 5.30 Combined Drag Results – Cone 2 Mach 1.29

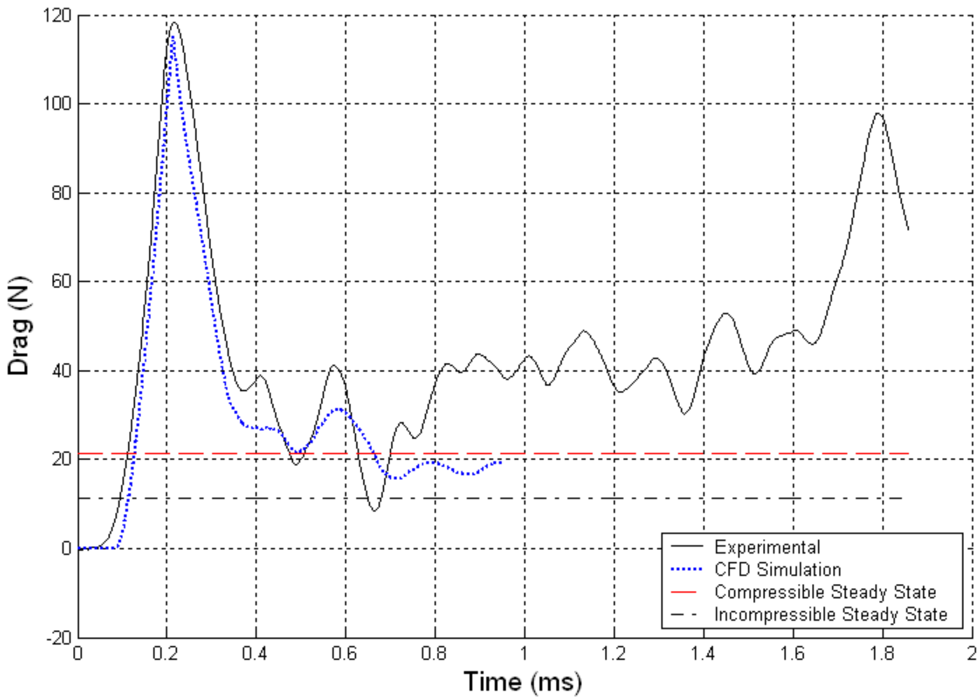

Figure 5.31 Combined Drag Results – Cone 3 Mach 1.27

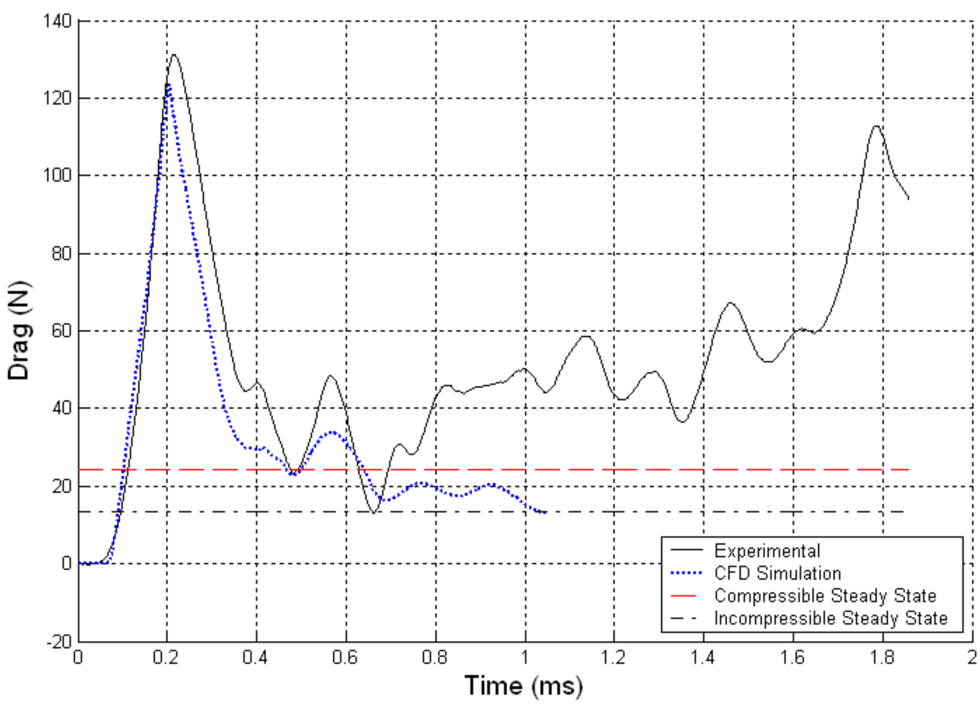

Figure 5.32 Combined Drag Results – Cone 3 Mach 1.29

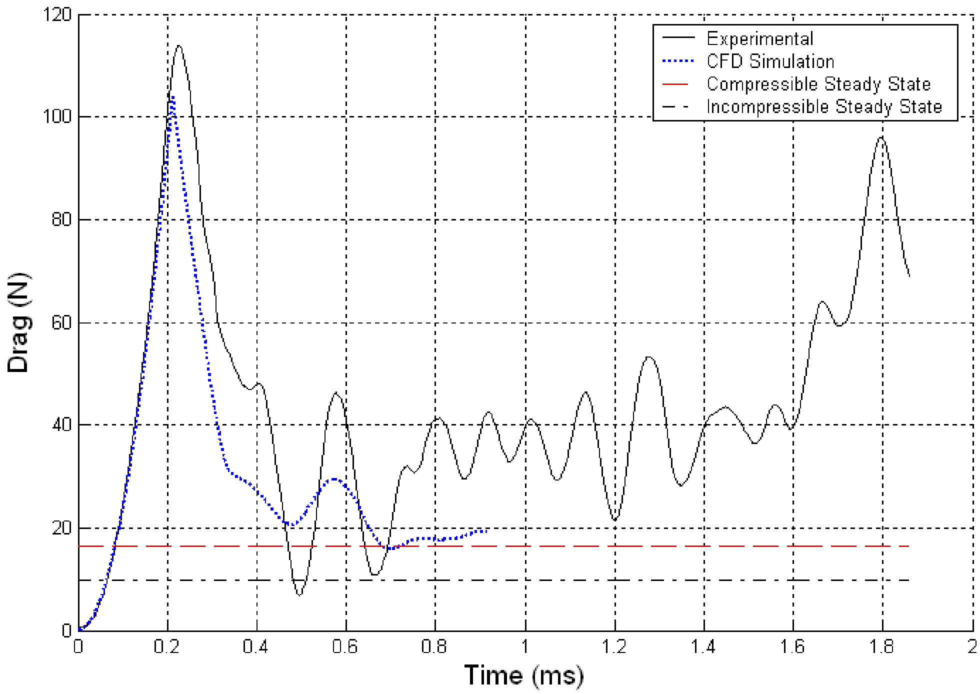

Figure 5.33 Combined Drag Results – Cone 4 Mach 1.26

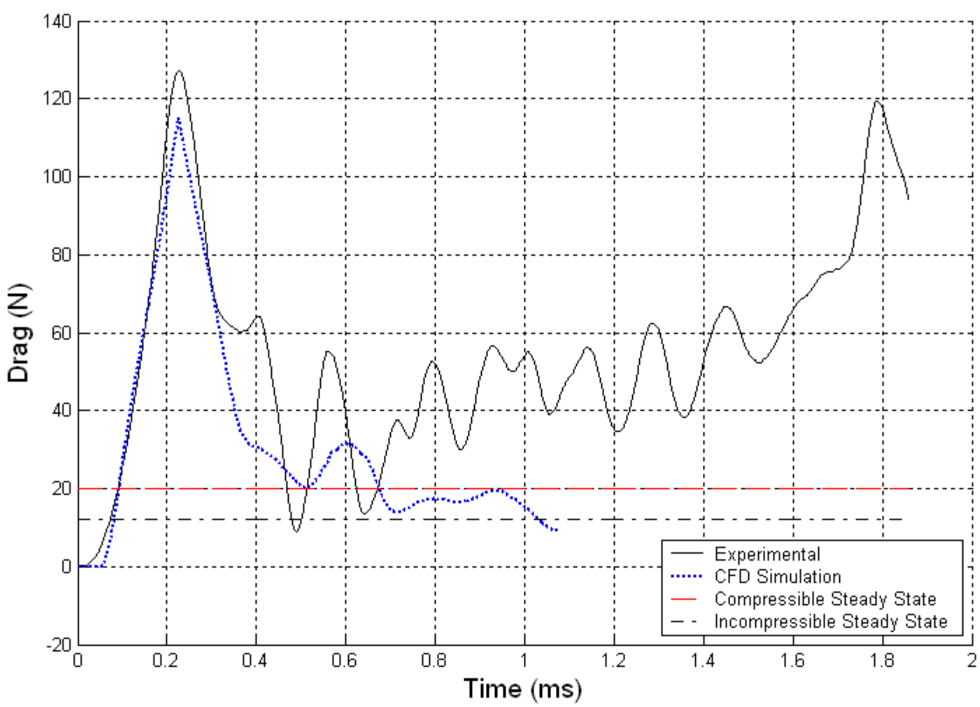

Figure 5.34 Combined Drag Results – Cone 4 Mach 1.29

6 Discussion

6.1 The Effect of Shock/Model Interaction on Drag

Visualisation of the experimental test section was not possible due to the design of the shock tube. It was thus decided to investigate the nature of the shock reflection and diffraction using numerical simulations. Experimentally recorded drag and drag obtained from the numerical simulations, represented by Figures 5.27 through 5.34, compare very favourably. The drag obtained numerically follows a consistent pattern for each model, with an increase in Mach number scaling the drag throughout a test. This can be seen in Figures 5.19 to 5.23 and proves that visualisation of the flow fields over the range of Mach numbers studied is unnecessary. The analysis of the shock interactions with all the models was therefore confined to a common Mach number of 1.5. The images in this section are density contours obtained from the numerical simulations and they refer to points shown on the corresponding drag curves.

6.1.1 Shock Interaction with Conical Models

The drag on Cone 1 (having a half-vertex angle of 30°), shown in Figure 6.1, starts to rise at 0.14 ms, the point at which the incident shock wave arrives at the apex of the cone. Immediately after the shock wave impacts the cone, a bow-shaped reflected shock forms and propagates upstream as illustrated in Figure 6.2. Closer inspection of this figure shows that the type of reflection is in fact Mach reflection. The region between the reflected wave and the cone experiences a very high pressure while the downstream portion of the cone is still at atmospheric pressure. The increase in drag is due to this large pressure differential.

The drag reaches a maximum when the incident shock reaches the base of the cone (Figure 6.3). At this point, the shock wave starts to diffract around the base of the cone forming a vortex as illustrated by Figure 6.4. As the initial shock wave propagates further, it impacts and reflects off the cone support (corresponding to the SWDB of the experimental apparatus). At the same time, the first reflected shock wave from the cone has reached the wall of the shock tube and been reflected once more. These reflections can be seen in Figures 6.5 and 6.6.

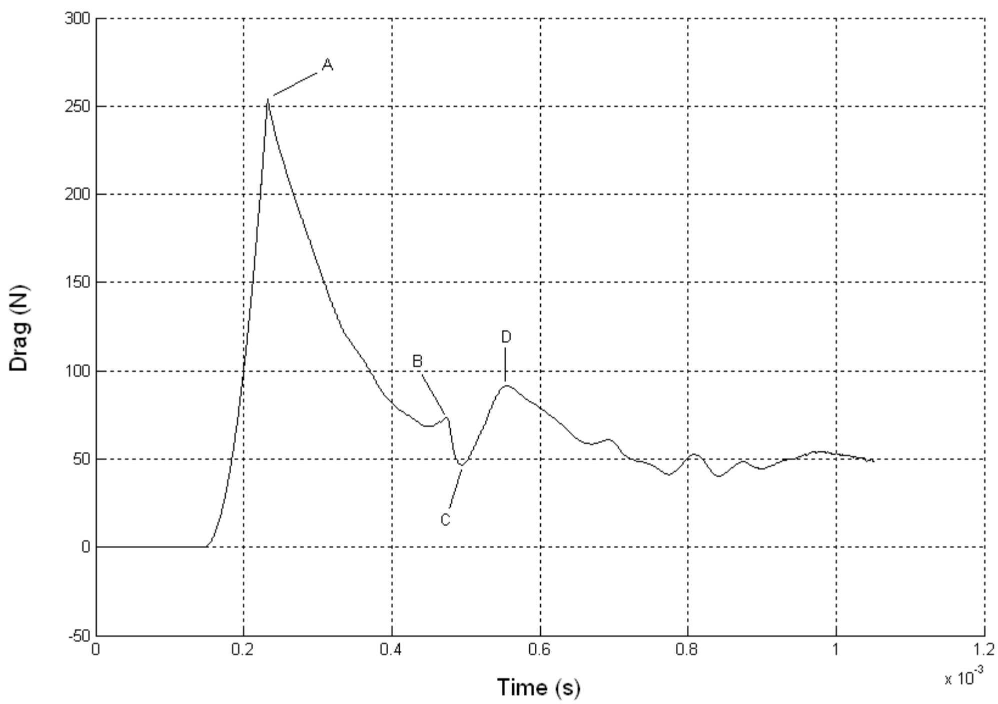

Figure 6.1 Drag on Cone 1 – Mach 1.5

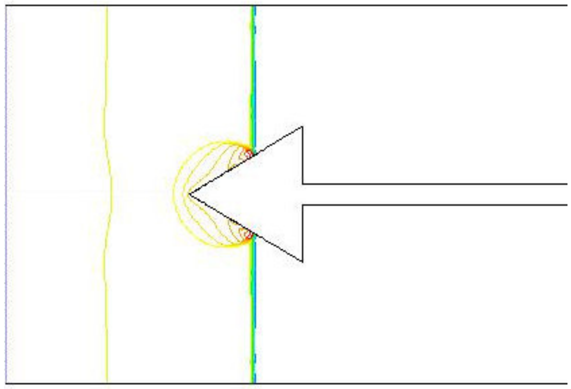

Figure 6.2 Cone 1 - 0.2 ms

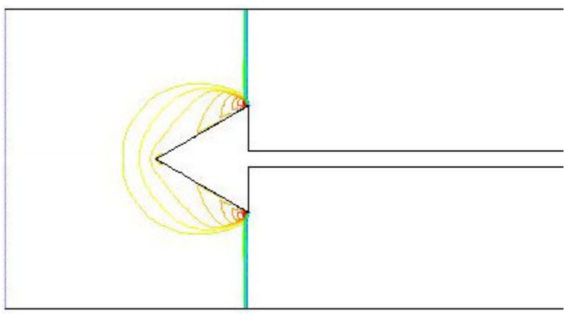

Figure 6.3 Cone 1 - Point A (0.23 ms)

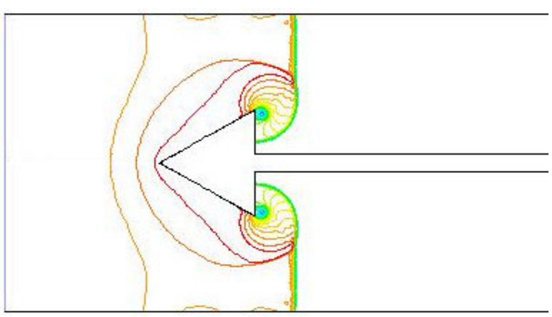

Figure 6.4 Cone 1 - 0.27 ms

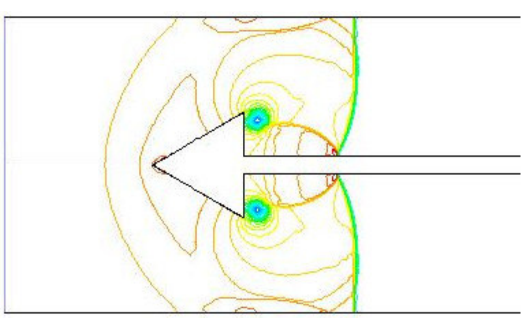

Figure 6.5 Cone 1 - 0.34 ms

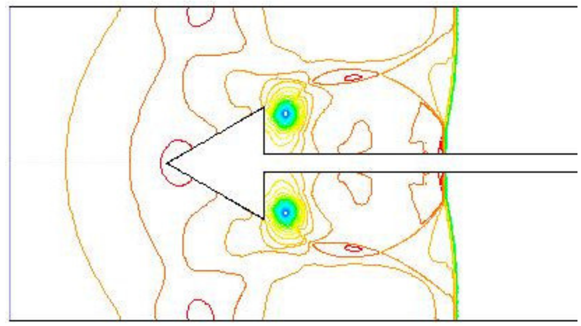

Figure 6.6 Cone 1 - 0.41 ms

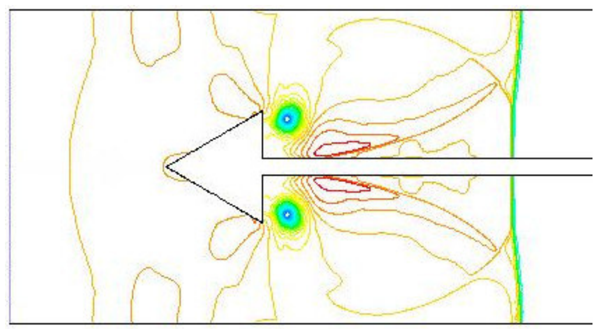

Figure 6.7 Cone 1 - Point B (0.47 ms)

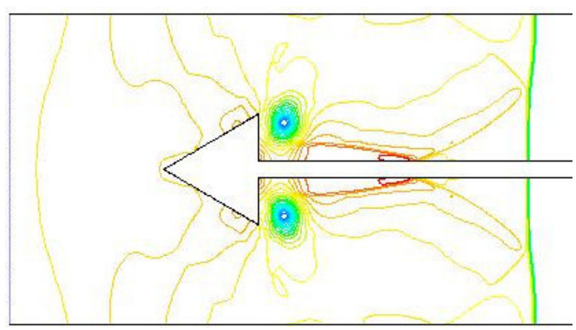

Figure 6.8 Cone 1 - Point C (0.5 ms)

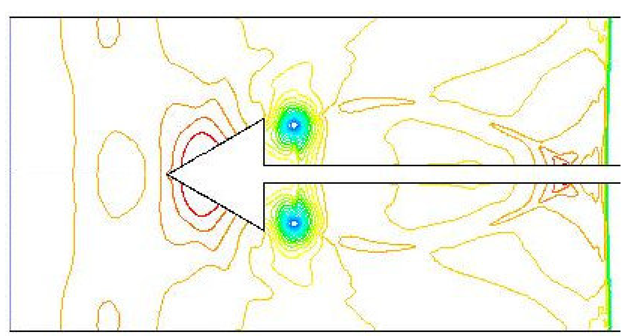

Figure 6.9 Cone 1 - Point D (0.56 m)

The drag starts to decrease less rapidly at approximately 0.34 ms before rising slightly again at 0.44 ms. At 0.47 ms (Point B) the drag drops once more. This behaviour is consistent with the vortex being shed from the cone. At 0.34 ms (Figure 6.5) the vortex is still attached to the cone whereas at Point B (Figure 6.7) the vortex has been shed. When a vortex forms behind an object the pressure difference across the object increases causing an increase in drag. If the vortex was shed the pressure difference would be restored and thus the drag would decrease.

The flow field becomes increasingly difficult to analyse as the number of shock reflections off the shock tube walls and the model support increases. The decrease in drag between Point B and Point C corresponds to the reflected waves impacting the base of the cone thus creating a force on the cone in the upstream direction. Between Point C and Point D the reflected waves are travelling over the sides of the cone (illustrated in Figure 6.9) and the direction of the pressure differential is downstream once more, thus causing the drag to increase. Further fluctuations diminish steadily over time, consistent with the attenuation of the reflected waves.

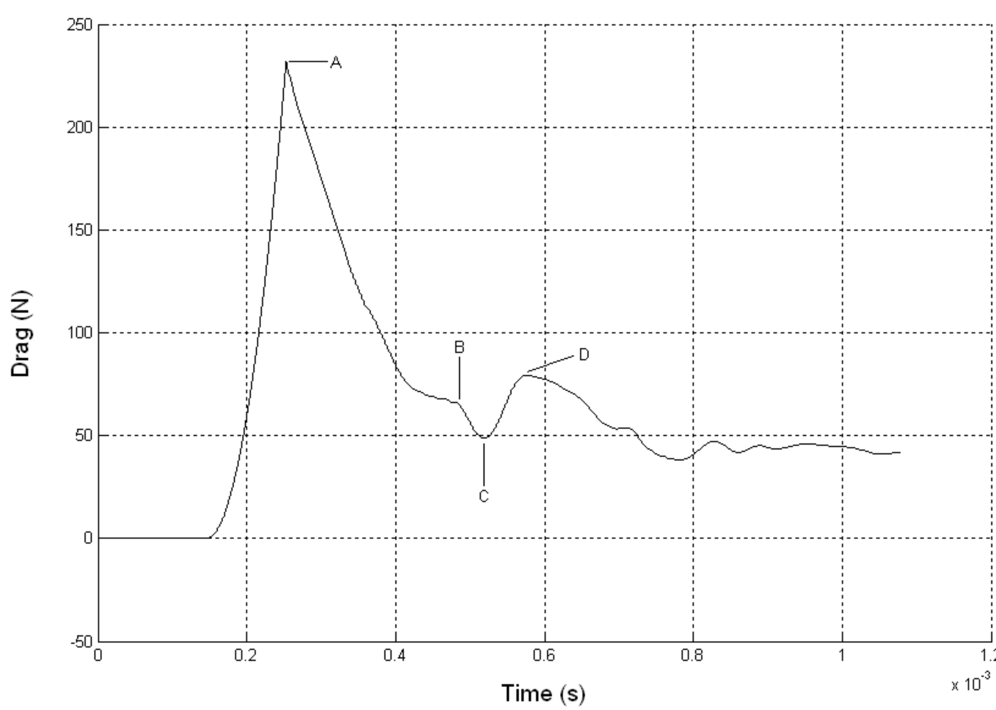

Figure 6.10 Drag on Cone 2 – Mach 1.5

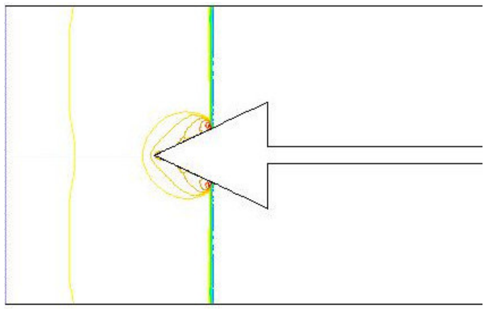

Figure 6.11 Cone 2 - 0.2 ms

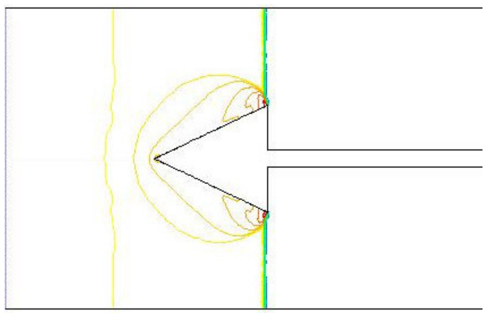

Figure 6.12 Cone 2 - Point A (0.25 ms)

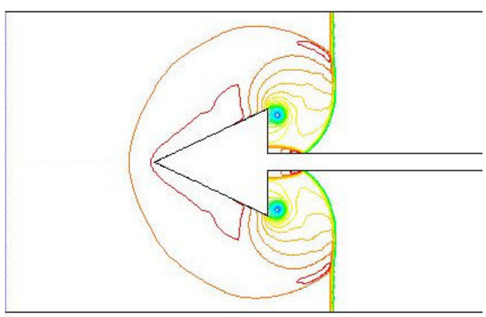

Figure 6.13 Cone 2 - 0.32 ms

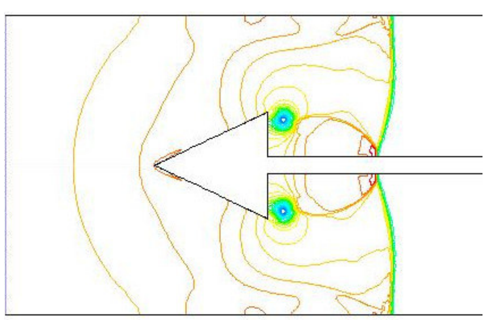

Figure 6.14 Cone 2 - 0.38 ms

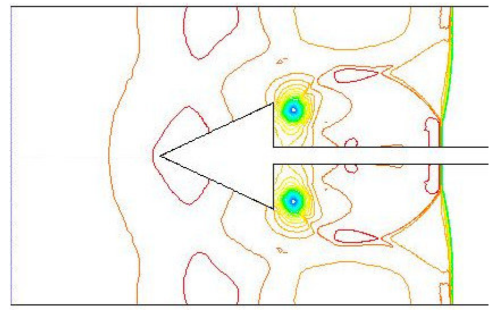

Figure 6.15 Cone 2 - 0.43 ms

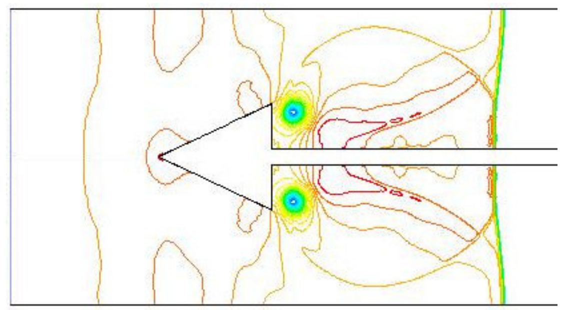

Figure 6.16 Cone 2 - Point B (0.48 ms)

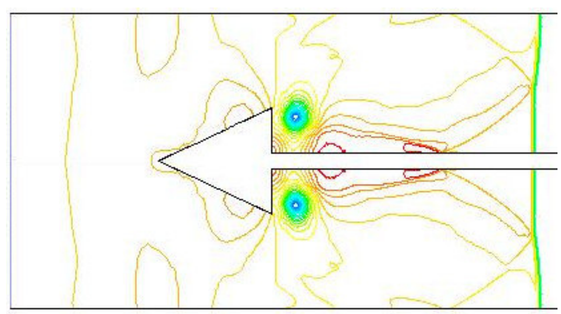

Figure 6.17 Cone 2 - Point C (0.52 ms)

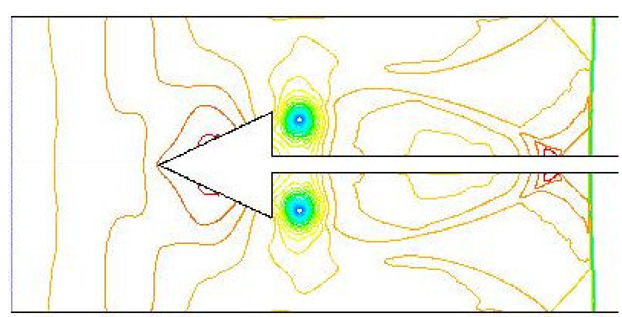

Figure 6.18 Cone 2 - Point D (0.58 m)

The mode of reflection of the incident wave off all of the cones appears to be Mach reflection, with the length of the Mach stem increasing as the half-vertex angle decreases. The mode of reflection is not thought to play a critical role in the drag loading however, since research done by Sun et al. (2004) into the transition from regular to Mach reflection over spheres showed the mode of reflection not to influence the drag.

The drag on Cones 2, 3 and 4 (having half-vertex angles of 25°, 20° and 15° respectively) at Mach 1.5 and the corresponding density contours are shown in Figures 6.10 to 6.36. The shock wave interactions with each of these cones are much the same as described for Cone 1. There is a small difference though. The first small spike visible in the drag after the shock wave has passed over Cone 1, as mentioned above, smoothes out steadily as the half-vertex angle is decreased. One aspect of the reflection that is thought to influence the drag in this way is the shape of the reflected wave.

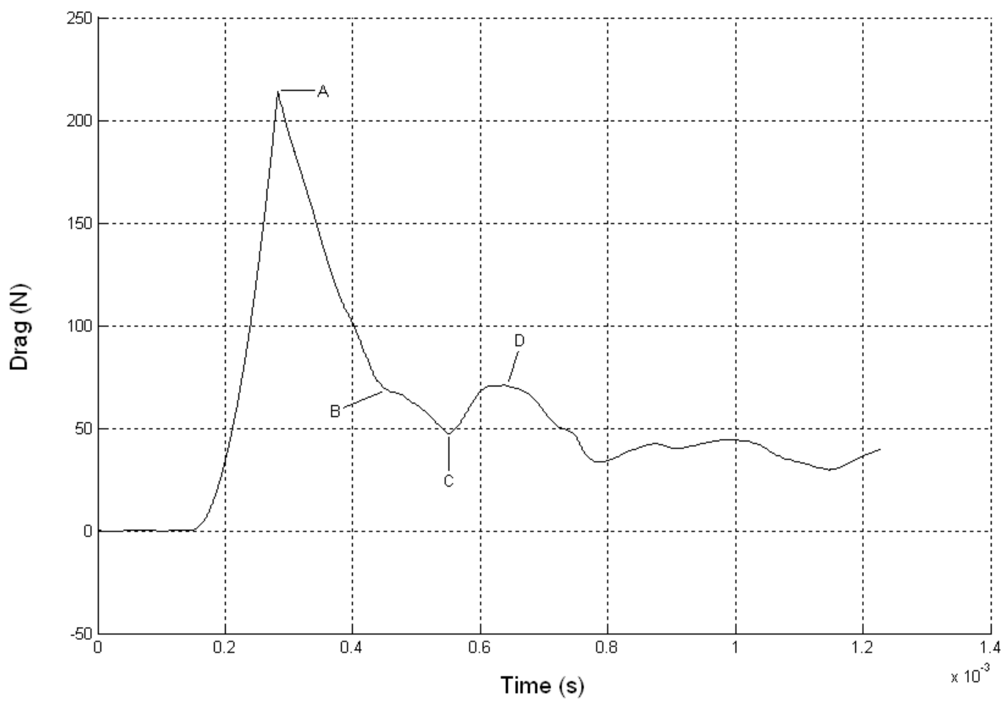

Figure 6.19 Drag on Cone 3 – Mach 1.5

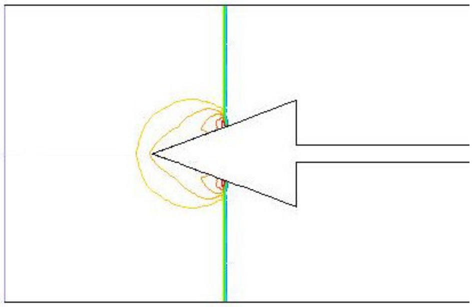
Figure 6.20 Cone 3 - 0.22 ms

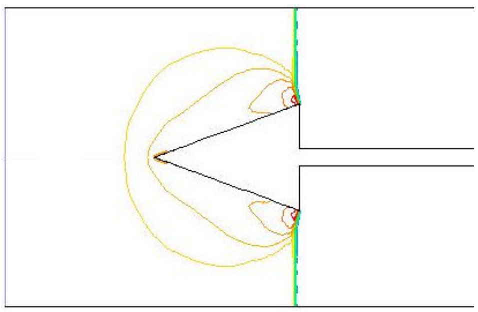
Figure 6.21 Cone 3 - Point A (0.28 ms)

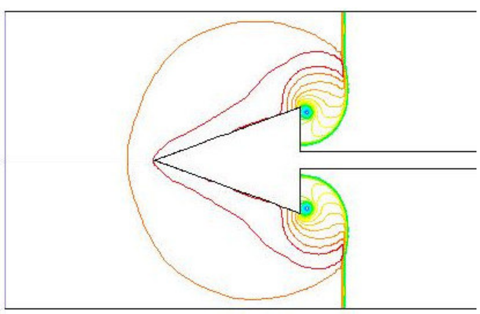
Figure 6.22 Cone 3 - 0.33 ms

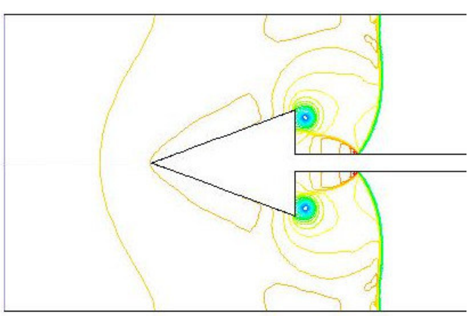
Figure 6.23 Cone 3 - 0.37 ms

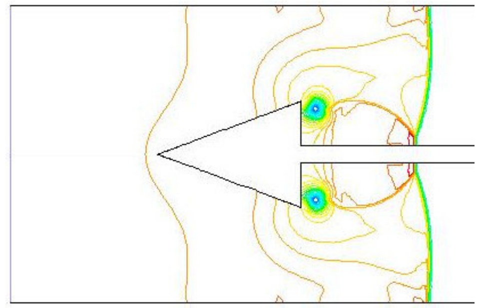
Figure 6.24 Cone 3 - 0.41 ms

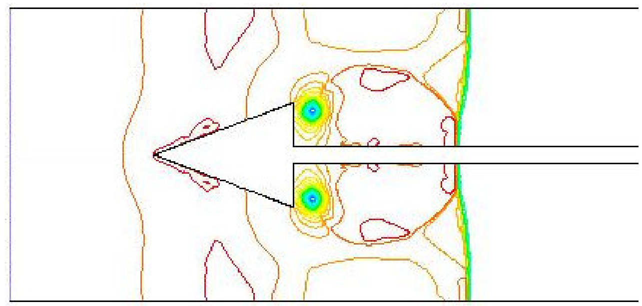
Figure 6.25 Cone 3 - Point B (0.46 ms)

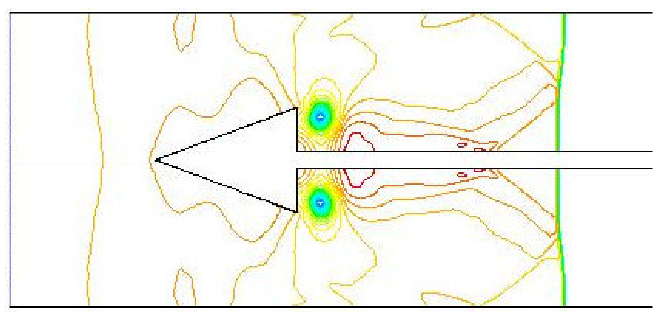
Figure 6.26 Cone 3 - Point C (0.55 ms)

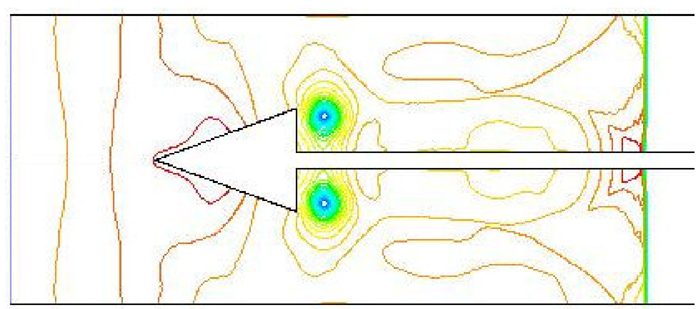
Figure 6.27 Cone 3 - Point D (0.64 ms)

The curvature of the reflected wave diminishes as the half-vertex angle decreases. Figure 6.2 (Cone 1) shows an essentially spherical reflected wave whereas the reflected wave in Figure 6.29 (Cone 4) is far more elongated. A more elongated reflected wave results in a greater portion of the wave travelling upstream, away from the cone.

The strength of the subsequent reflected shock wave off the shock tube walls that impacts the cone will therefore decrease. This secondary reflected wave is clearly visible in Figure 6.6 (Cone 1) whereas in Figure 6.33 (Cone 4) it does not appear at all. The absence of this reflected wave is consistent with the absence of a significant change in the drag for Cone 4 at Point B. This trend can also be seen in the experimental drag curves (Figures 5.11 to 5.14) at approximately 0.4 ms. The reflection of the shock wave off the support becomes the primary cause of subsequent fluctuations and thus negates any further effect of the weakened secondary shock wave.

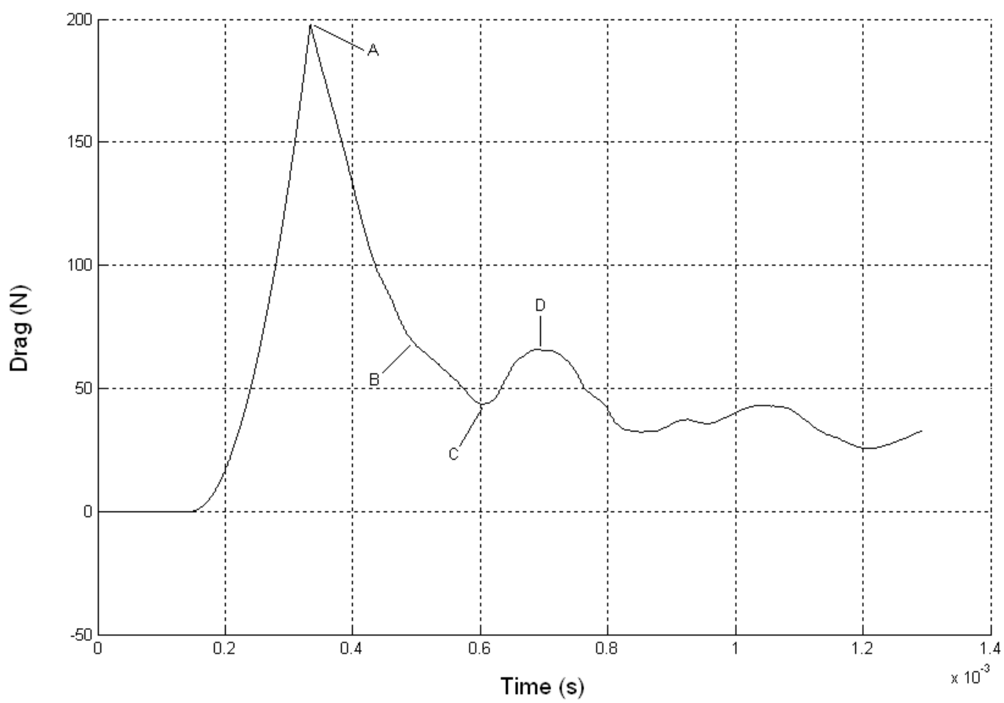

Figure 6.28 Drag on Cone 4 – Mach 1.5

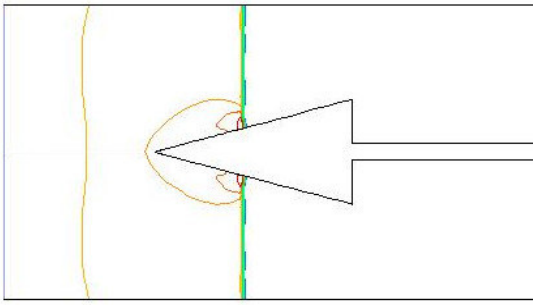

Figure 6.29 Cone 4 - 0.23 ms

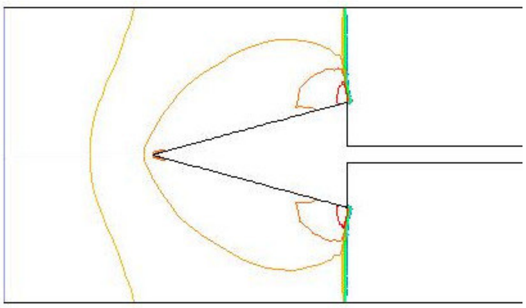

Figure 6.30 Cone 4 - Point A (0.33 ms)

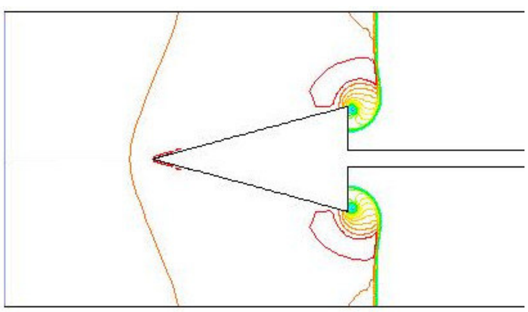

Figure 6.31 Cone 4 - 0.37 ms

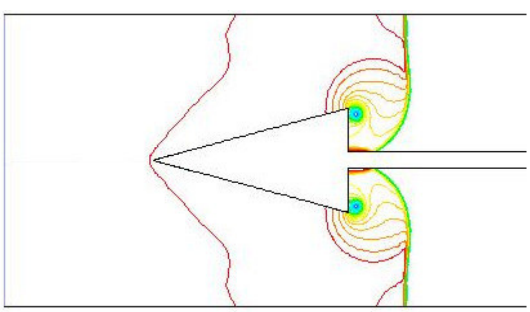

Figure 6.32 Cone 4 - 0.4 ms

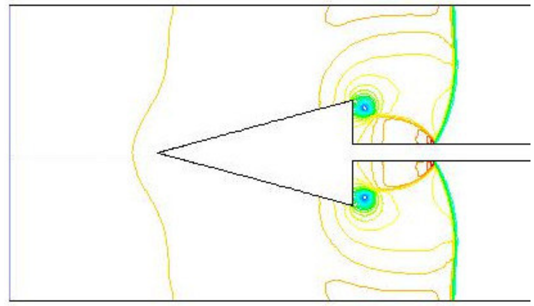

Figure 6.33 Cone 4 - 0.44 ms

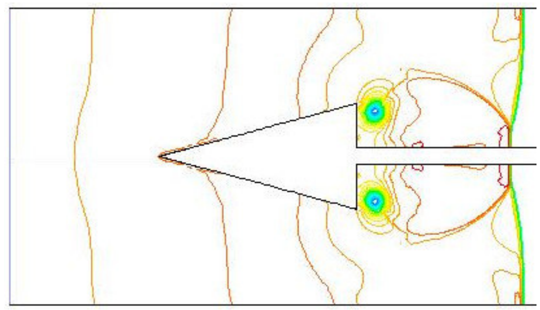

Figure 6.34 Cone 4 - Point B (0.5 ms)

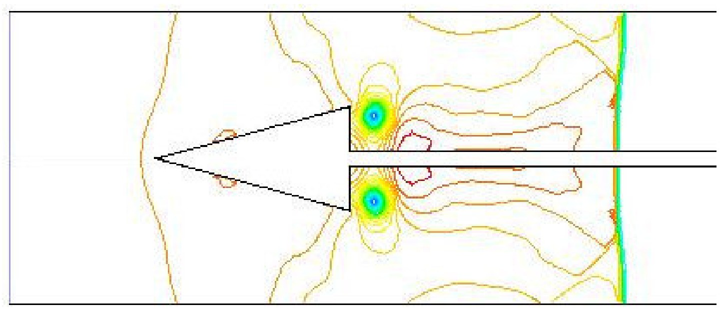

Figure 6.35 Cone 4 - Point C (0.61 ms)

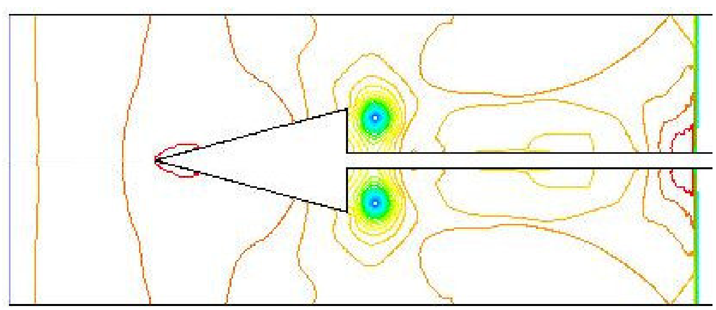

Figure 6.36 Cone 4 - Point D (0.69 ms)

There should be no significant difference in the magnitude of the subsequent fluctuations for the different cones since the magnitude and angle of the wave reflected off the support is constant. This is observed in both the numerical and experimental results. The amplitude of the fluctuations, particularly the first spike, is greater in the experimental results though.

6.1.2 Shock Interaction with the Sphere

Bredin (2002) investigated the unsteady drag on a sphere due to shock loading using the same experimental apparatus as the current work. Details of this work are given in Section 3. One of the objectives of the current work was to verify the drag measurements obtained in the previous study. In particular, it was required to confirm that the negative drag measured was not due to balance error. This has been tackled in two ways, namely measuring the drag over cones using the same balance and performing numerical simulations of the flow over the sphere. Figure 6.37 shows the numerically obtained drag on the sphere at Mach 1.5, while Figures 6.38 through 6.45 are the corresponding density contours.

As with the conical models, the drag starts to rise as the shock arrives at the front of the cone. The transition from regular to Mach reflection, as found by Sun et al. (2004) and illustrated in Figure 3.13, can be observed on closer inspection of the density contours. Sun et al. (2004) concluded that the mode of reflection does not affect the drag; rather it is merely a transient phenomenon of shock/sphere interaction. The maximum drag on the cones occurs as the wave reaches the base of the cones. The maximum drag on the sphere, however, occurs a short time before the wave reaches the equator of the sphere. This is shown in Figure 6.38 (Point A on the drag curve). As described previously, the region between the sphere and the reflected wave is at a much higher pressure than the downstream section resulting in an increase in drag.

The drag then decreases steadily as the reflected wave propagates away from the cone causing the pressure between the reflected wave and the sphere to decay. Figure 6.37 shows a further sharp drop in the drag at 0.4 ms (Point B), with the drag becoming negative shortly thereafter. This negative drag correlates well with results from Bredin (2002) as can be seen in Figure 3.12. Figures 6.42 and 6.43 are useful in explaining the negative drag. In these figures, one can clearly see the reflected waves from the walls and the support. These waves cover a larger portion of the downstream hemisphere of the sphere than the upstream hemisphere. Since there are high-pressure regions behind the reflected waves, the net force on the sphere may in fact be acting upstream which would account for the negative drag. Further propagation of the reflected waves results in the upstream hemisphere being covered by the wave and thus the drag rises once more.

The numerically obtained drag results agree well with the results obtained by Bredin (2002). These results confirm that both the negative drag and large post-shock fluctuations (see Figure 3.12) were not due to balance error but rather were a product of the shock reflections off the sphere support and the walls of the shock tube.

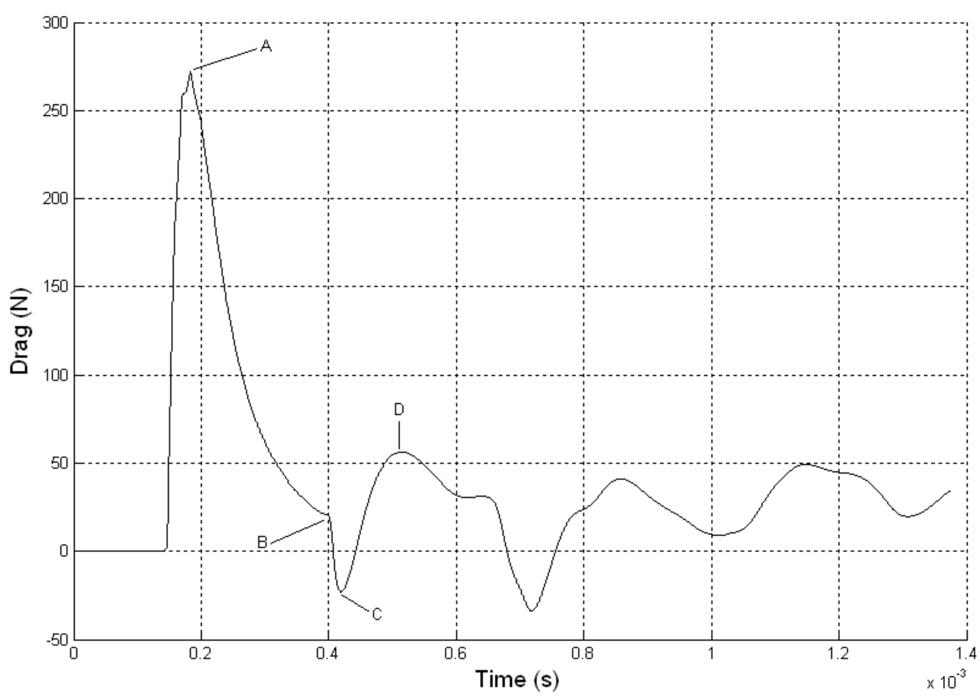

Figure 6.37 Drag on Sphere – Mach 1.5

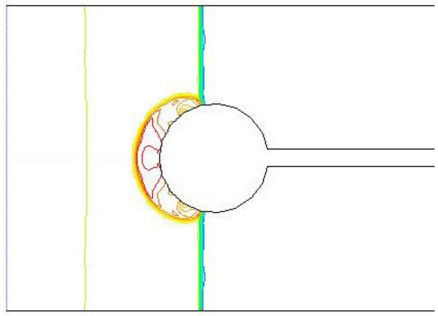

Figure 6.38 Sphere - Point A (0.18 ms)

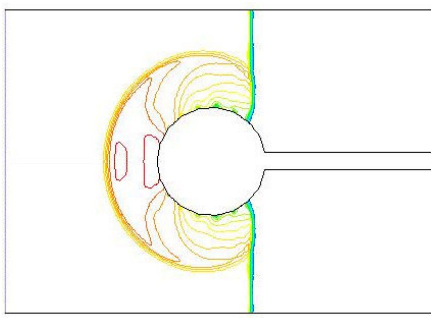

Figure 6.39 Sphere - 0.24 ms

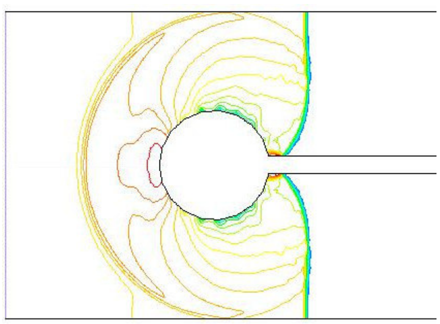

Figure 6.40 Sphere - 0.28 ms

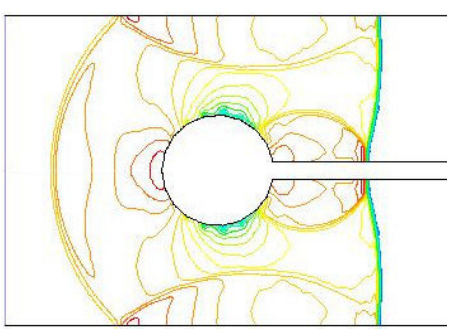

Figure 6.41 Sphere - 0.35 ms

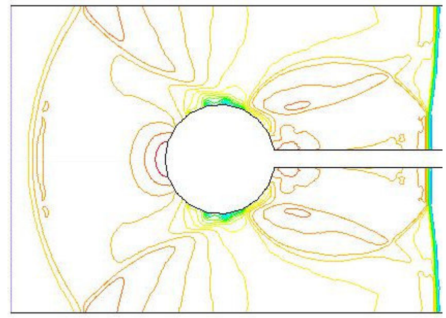

Figure 6.42 Sphere - Point B (0.4 ms)

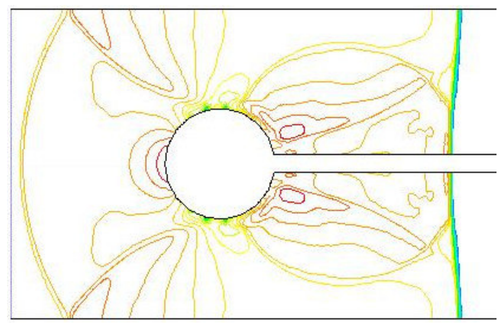

Figure 6.43 Sphere - Point C (0.42 ms)

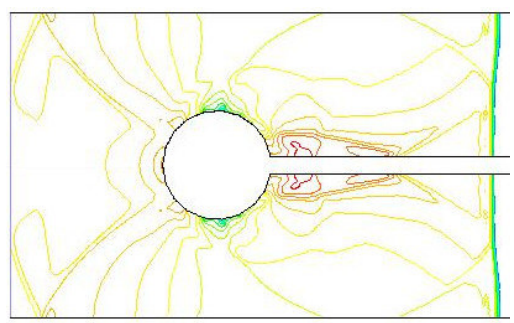

Figure 6.44 Sphere - 0.47 ms

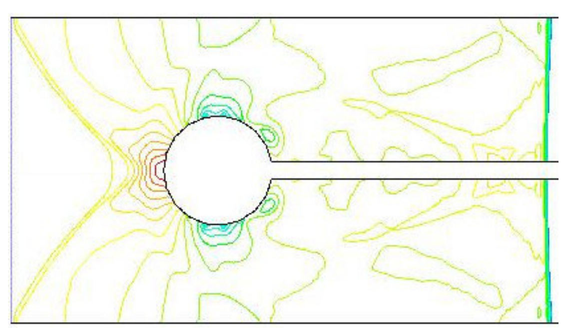

Figure 6.45 Sphere - Point D (0.52 ms)

6.2 Maximum Unsteady Drag Values

The maximum unsteady drag values measured experimentally ranged from 53.5 N for Cone 4 (with a half-vertex angle of 15°) at a Mach number of 1.14 to 148.6 N for Cone 1 (with a half-vertex angle of 30°) at a Mach number of 1.29. The correlations of these maximum values with numerical (CFD) results and steady state drag values are discussed below.

6.2.1 Experimental and CFD Results

The experimental and numerical drag curves, combined in Figures 5.27 to 5.34, compare very favourably. The important features of the drag curves and their causes were discussed in the previous section. Table 6.1 uses the maximum drag to quantify the correlation between the experimental and numerical results. The maximum CFD drag was divided by the maximum experimental drag and multiplied by 100 to get a percentage. The results show the closest correlation to be within 0.4% for Cone 1 at a Mach number of 1.27 and the least accurate comparison to be within 9.6% for Cone 4 at a Mach number of 1.29.

Table 6.1 Maximum Drag Correlations between CFD and Experimental Results

Test	Maximum Experimental Drag (N)	Maximum CFD Drag (N)	CFD/Experimental (%)
Cone 1 Mach 1.27	136.4	134.8	99.6
Cone 1 Mach 1.29	148.6	144.3	97.1
Cone 2 Mach 1.27	119.5	123.4	103.3
Cone 2 Mach 1.29	136.7	132.3	96.8
Cone 3 Mach 1.27	118.4	115.2	97.3
Cone 3 Mach 1.29	131.3	123.6	94.1
Cone 4 Mach 1.26	113.9	103.9	93.3
Cone 4 Mach 1.29	127.2	115	90.4

6.2.2 Experimental and Steady State Results

Figures 5.27 to 5.34 show the combined experimental and numerical drag for various tests as well as two steady state drag values for each test. The derivation of the two steady state drag values is explained in Section 5.4. These results show the post shock unsteady drag to be of the same order of magnitude as the steady state drag.

Comparing the maximum experimentally measured drag with the steady state drag values yields some positive results. Previous research, such as Takayama et al. (2004), has not compared the maximum unsteady drag with steady state values for a range of Mach numbers. Previous work also compares drag coefficients rather than the drag force, which has been deemed unreliable as stated previously. The findings have up to this point always shown the peak unsteady drag to be far greater than the steady state values. For example, Takayama et al. (2004) quote a ratio of 20:1 between the peak unsteady drag coefficient and the corresponding steady value for shock loading of a sphere at a Mach number of 1.22 in air.

The results shown in Section 5.4 also reveal the peak unsteady drag values to be greater than the corresponding incompressible steady state values. Figures 6.46 through 6.49 present the maximum and steady state drag values for each cone as a function of shock Mach number. As stated previously, the post shock flow properties were calculated to obtain the steady state values.

The maximum unsteady drag values appear to increase sharply with an increase in Mach number. Both the incompressible and compressible steady state drag values also increase as a function of Mach number, though at a slower rate than the unsteady drag. The steady state values also increase noticeably as the half-vertex angle of the cone increases. The ratio of maximum unsteady drag to compressible steady state drag varied from 4.4:1 at M_S = 1.31 for Cone 2 to 9.8:1 at M_S = 1.14 for Cone 4, while the ratio of maximum unsteady drag to incompressible steady state drag varied from 8.3:1 at M_S = 1.31 for Cone 2 to 22.2:1 at M_S = 1.12 for Cone 1.

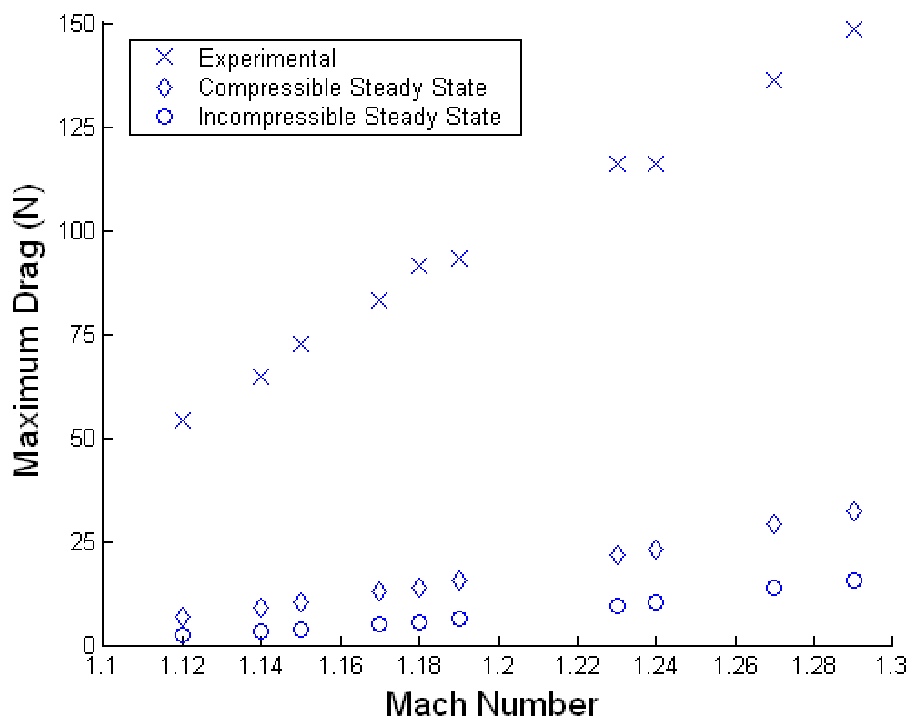

Figure 6.46 Maximum and steady state drag values on Cone 1

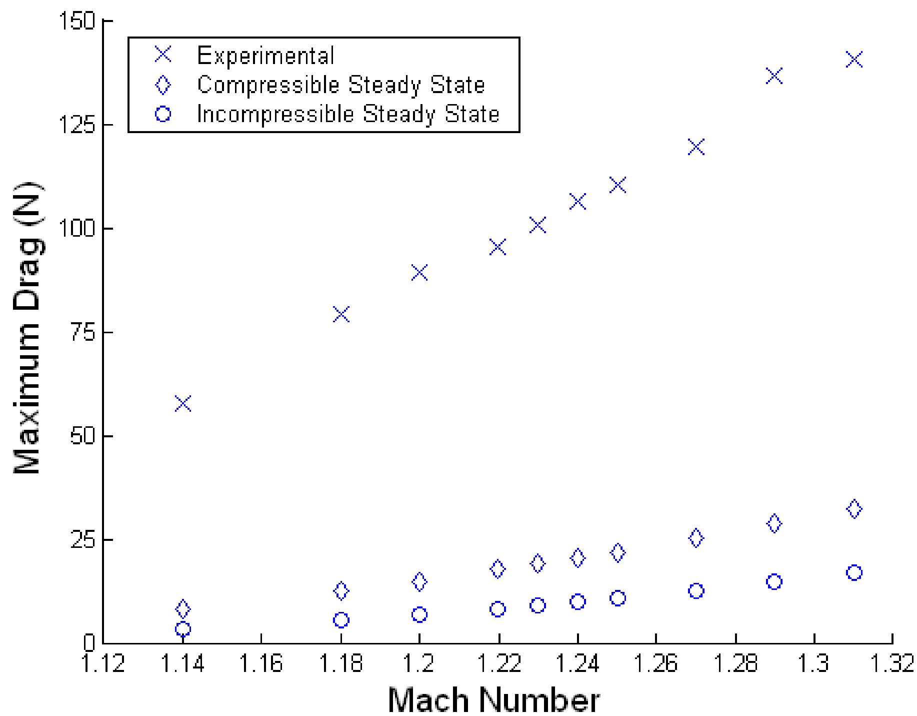

Figure 6.47 Maximum and steady state drag values on Cone 2

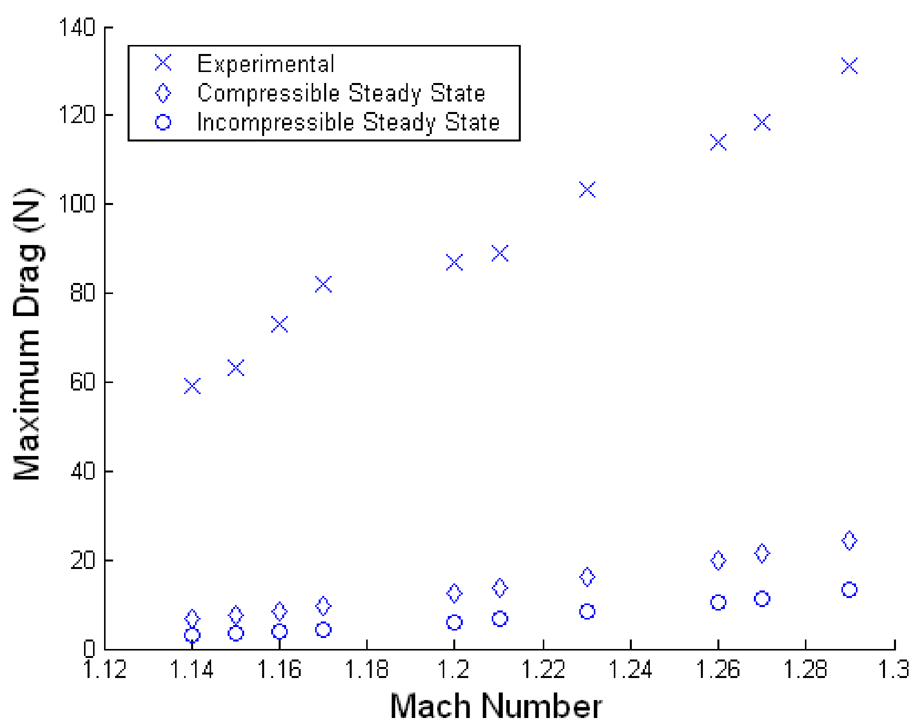

Figure 6.48 Maximum and steady state drag values on Cone 3

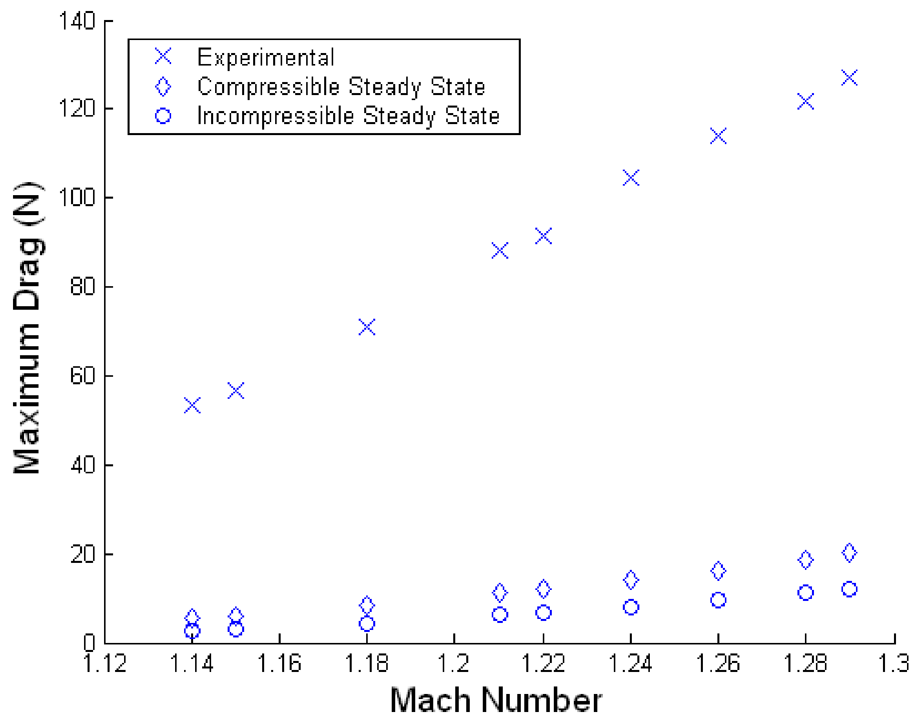

Figure 6.49 Maximum and steady state drag values on Cone 4

6.3 Unsteady Drag as a Function of Mach Number and Cone Angle

Experimental and numerical results show the unsteady drag measured over all the models to be directly proportional to the Mach number. Figures 6.46 to 6.49 show this relationship between the maximum unsteady drag measured experimentally and the Mach number. The post-shock fluctuations also increase with an increase in Mach number as can be seen in Figures 5.11 to 5.14 for the experimental results and in Figures 5.19 to 5.23 for the numerical results. This can be attributed to the fact that an increase in the strength of the incident shock wave will result in an increase in the strength of the reflected shock waves that are the cause of the fluctuations.

Both experimental (Figures 5.15 to 5.18) and numerical results (Figures 5.24 to 5.26) show the unsteady drag to increase as the cone angle increases. This relationship is well established for drag in steady flow as illustrated by Figure 3.6. This figure shows the steady state drag data to be increasing at a decreasing rate whereas for the range of angles tested the unsteady drag appears to increase at an increasing rate. This trend is illustrated, for various numerical and experimental results, in Figure 6.50. Since the range of half-vertex angles tested was fairly small, due to the physical constraints of the shock tube and SWDB, further investigation of this relationship is recommended. Numerical simulations would be most suitable for such a study as the full range of angles may be tested.

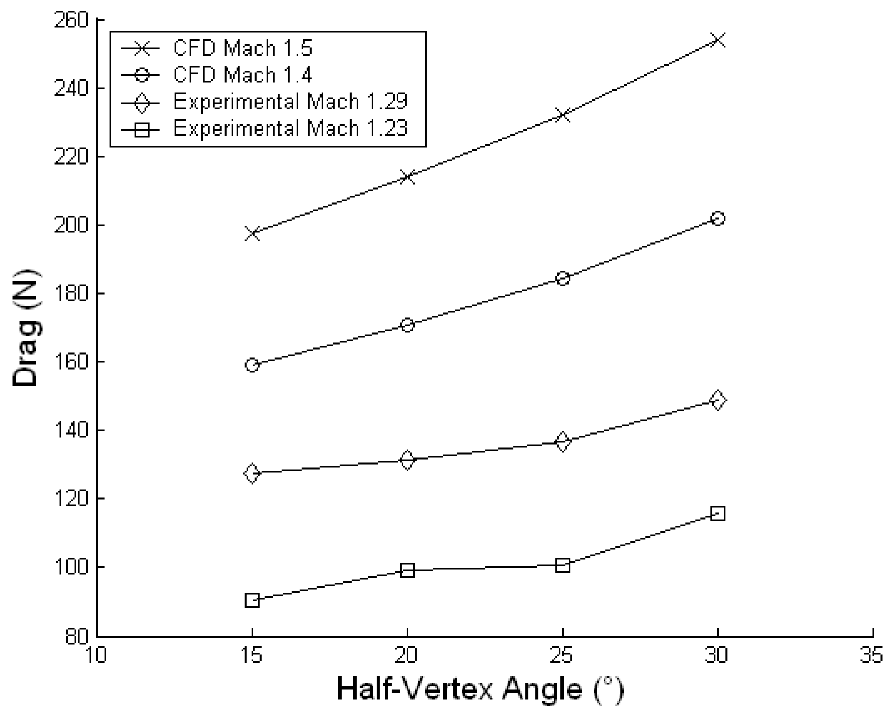

Figure 6.50 Unsteady drag as a function of half-vertex angle

7 Conclusions

The following conclusions could be drawn from the work performed for this project:

- The drag in unsteady compressible flow due to shock wave loading on four 50 mm diameter aluminium cones, having half-vertex angles ranging from 15° to 30°, was measured using a Stress Wave Drag Balance (SWDB) developed by Bredin (2002).
- The unsteady drag was measured experimentally at shock wave Mach numbers ranging from 1.12 to 1.31. The maximum unsteady drag values measured experimentally ranged from 53.5 N for the 15° cone at a Mach number of 1.14 to 148.6 N for the 30° cone at a Mach number of 1.29.
- Numerical simulations, using the commercially available CFD package, Fluent 6.1.22©, were conducted for each of the geometries of test models, at Mach numbers ranging from 1.26 to 1.5. Simulations were also performed for a 50 mm diameter sphere, corresponding to testing done by Bredin (2002) using the same experimental apparatus. The drag obtained numerically agreed well with experimental results. The negative drag and large post-shock drag fluctuations measured by Bredin (2002) were present in the numerical results and thus confirm that these features were not due to balance error. One can thus conclude that the SWDB is suitable for measuring drag in unsteady compressible flow.
- The unsteady drag, obtained numerically and experimentally on the conical models as well as the numerically obtained drag on the sphere, was shown to be directly proportional to the shock wave Mach number. The numerical results for the sphere confirm results reported by Bredin (2002).

- The unsteady drag increased as the half-vertex angle increased as was expected. However, the unsteady drag increased at an increasing rate, unlike that predicted by steady state drag data.
- The unsteady drag was compared to two steady state values, namely an incompressible steady state drag and a compressible steady state drag. The incompressible value was obtained from drag coefficient data in incompressible flow for the appropriate range of Reynolds numbers. The compressible value, obtained numerically, refers to the drag that would occur under steady compressible flow with a gas Mach number corresponding to the post shock Mach number of the unsteady case. The steady state drag values were of the same order of magnitude as the post shock unsteady drag.
- The ratio of the maximum unsteady drag to the compressible steady state drag varied from 4.4:1 to 9.8:1, while the ratio of the maximum unsteady drag to the incompressible steady state drag varied from 8.3:1 to 22.2:1.
- Numerical simulations were employed to visualise the shock/model interactions and proved that post-shock fluctuations are due to shock wave reflections off the shock tube walls and the model support. The drag forces on the conical models peak when the shock wave reaches the base of the cone whereas the drag on the sphere peaks just before the shock reaches the equator of the sphere.

8 Recommendations for Future Work

8.1 Further Experimental Testing

- The current work has proven that the stress wave drag balance is suitable for measuring drag in unsteady compressible flow. Models of different shapes can now be tested with confidence. Scaled models of bodies subjected to unsteady flow such as aircraft would be of particular interest.
- It may be valuable in the future to conduct concurrent steady state testing on any test models in a wind tunnel to enable more reliable comparisons between the steady and unsteady cases.
- All tests conducted were for shock wave inputs with steady post-shock flow. However, the shock tube is also capable of producing shock wave inputs with decelerating post-shock flow and multiple acceleration flow (compression wave tests). Further testing on the conical models should be conducted under these flow conditions.
- The signal to noise ratio of the balance may be doubled by using a full Wheatstone bridge instead of a half bridge.
- Further investigation into methods of improving the quality and repeatability of the calibration procedure is recommended. One does not notice any inconsistencies in drag measurements on one model at various Mach numbers since the calibration details are always the same. Comparing various models at the same Mach number, however, shows some deviation from expected results. It is suspected that small differences in the calibration procedure are the cause.

- The method of characteristics code should be improved to enable the modelling of multiple shock waves within a test.
- Adapting the balance to create an infinite testing time balance has been proposed. This may be possible by placing strain gauges at a second location on the balance and predicting the effects of reflected waves within the model and balance. Further details of this proposal can be found in Bredin (2002).

8.2 Further Numerical Work

- Numerical work should be undertaken to investigate fully the effects on the drag of shock wave reflections off the shock tube walls and the stress wave drag balance. This would be possible by omitting the balance from the model geometry and ensuring that the boundaries of the flow field are sufficiently far from the model.
- Due to physical constraints it is not possible to determine experimentally the effect of cone angle on the drag over the full range of cone angles. Numerical simulations would be ideal for such a study.

References

Basset, A.B (1888), *On the motion of a sphere in a viscous liquid*, Philosophical Transactions of the Royal Society of London, Series A 179: 43-63.

Boussinesq, J (1885), *Sur la résistance qu'oppose un liquide…au mouvement varié d'une sphère solide…et produits soient négligeables*, C.R. Acad. Sci. Paris 100: 935-937.

Bredin, M.S (2002), *The Measurement of Drag in Unsteady Compressible Flow*, Thesis for the degree of Doctor of Philosophy, University of the Witwatersrand, Johannesburg.

Britan A, Elperin T, Igra O, Jiang J.P (1995), *Acceleration of a sphere behind planar shock waves*, Experiments in Fluids, Vol. 20, No. 2: 84-90.

Clift R, Grace J.R, Weber M.E (1978), *Bubbles, Drops and Particles*, Academic Press, New York.

Han Z, Yin X (1993), *Shock Dynamics*, Kluwer Academic Publishers, Dordrecht and Science Press, Beijing.

Hoerner, S.F (1965), *Fluid-Dynamic Drag*, Published by the Author, New York.

Igra O, Takayama K (1993), *Shock tube study of the drag coefficient of a sphere in a non-stationary flow*, Proceedings of the Royal Society of London Series A 442: 231-247.

John, E.A (1969), *Gas Dynamics*, Allyn and Bacon Inc., Boston.

Mee, D.J (2003), *Dynamic calibration of force balances for impulse hypersonic facilities*, Shock Waves, Vol. 12, No. 6: 443-455.

Morrison, R.B (1962), *Design Data for Aeronautics and Astronautics*, John Wiley and Sons, Inc., New York and London.

Rodriguez G, Grandeboueuf P, Khelifi M, Haas J.F (1995), *Drag coefficient measurement of spheres in a vertical shock tube and numerical simulation*, Proc. 20th Int. Symp. On Shock waves, Marseille, Vol. 3: 43-48.

Sanderson S.R, Simmons J.M (1991), *Drag Balance for Hypervelocity Impulse Facilities*, AIAA Journal, Vol. 29, No. 12: 2185-2191.

Smith A.L, Mee D.J (1996), *Drag measurements in a hypervelocity expansion tube*, Shock Waves, Vol. 6, No. 3: 161-166.

Stokes, G.G (1851), *On the effect of the internal friction of fluids on the motion of pendulums*, Trans. Camb. Phil. Soc. 9: 8-106.

Sun M, Saito T, Takayama K, Tanno H (2004), *Unsteady drag on a sphere by shock wave loading*, Shock Waves, Dec 2004.

Takayama K, Saito T, Sun M, Tamai K, Tanno H, Falcovitz J (2004), *Unsteady drag force measurements of shock loaded bodies suspended in a vertical shock tube*, Proc. Of 21st International Congress of Theoretical and Applied Mechanics, Warsaw, Poland, August 15-21, 2004.

Tamai K, Ogawa T, Ojima H, Falcovitz J, Takayama K (2004), *Unsteady drag force measurements over bodies with various configurations in a vertical shock tube*, Proc. Of

24th International Symposium on Shock Waves, Institute of Mechanics, Chinese Academy of Sciences, Beijing, China, July 11-16, 2004

Tanno H, Itoh K, Saito T, Abe A, Takayama K (2003), *Interaction of a shock with a sphere suspended in a vertical shock tube*, Shock Waves, Vol. 13, No. 3: 191-200.

Thompson, P.A (1972), *Compressible-Fluid Dynamics*, McGraw-Hill, New York.

Tyler A.L, Salt D.L (1977), *Periodic discontinuities in the acceleration of spheres in free flight*, Printed by the ASME.

White, F.M (1994), *Fluid Mechanics*, McGraw-Hill, New York.